NAVAL POSTGRADUATE SCHOOL

MONTEREY, CALIFORNIA

THESIS

TERMINAL HOMING FOR AUTONOMOUS UNDERWATER VEHICLE DOCKING

by

Eric B. Bermudez

June 2016

Thesis Advisor: Douglas Horner
Second Reader: Noel Du Toit

Approved for public release; distribution is unlimited

THIS PAGE INTENTIONALLY LEFT BLANK

REPORT DOCUMENTATION PAGE			*Form Approved OMB No. 0704-0188*

1. AGENCY USE ONLY *(Leave blank)*	**2. REPORT DATE** June 2016	**3. REPORT TYPE AND DATES COVERED** Master's thesis

4. TITLE AND SUBTITLE TERMINAL HOMING FOR AUTONOMOUS UNDERWATER VEHICLE DOCKING	**5. FUNDING NUMBERS**
6. AUTHOR(S) Eric B. Bermudez	
7. PERFORMING ORGANIZATION NAME(S) AND ADDRESS(ES) Naval Postgraduate School Monterey, CA 93943-5000	**8. PERFORMING ORGANIZATION REPORT NUMBER**
9. SPONSORING /MONITORING AGENCY NAME(S) AND ADDRESS(ES) N/A	**10. SPONSORING / MONITORING AGENCY REPORT NUMBER**

11. SUPPLEMENTARY NOTES The views expressed in this thesis are those of the author and do not reflect the official policy or position of the Department of Defense or the U.S. Government. IRB Protocol number ____N/A____.

12a. DISTRIBUTION / AVAILABILITY STATEMENT Approved for public release; distribution is unlimited	**12b. DISTRIBUTION CODE**

13. ABSTRACT

The use of docking stations for autonomous underwater vehicles (AUV) provides the ability to keep a vehicle on station, conducting missions for extended periods of time, with limited human interaction. However, the use of a docking station brings about challenges associated with terminal homing, position estimation, and vehicle control. A traditional single propeller-driven AUV must dock at a high relative approach velocity to maintain controllability, which can lead to serious damage to the AUV and the docking station. Alternatively, equipping a AUV with forward and aft pairs of horizontal and vertical cross-tunnel thrusters enables a hovering capability and allows for a slower, more deliberate approach that can help reduce potential damage during the terminal homing phase. Additionally, the commonly used ultra-short baseline (USBL) acoustic transponder attached to the docking station, which provides bearing and range measurements, can be asynchronous and sparse. The integration of these measurements into an optimal position estimation filter can potentially produce inaccuracies that are detrimental during docking operations. This thesis discusses the development of a hydrodynamic model and a filtering algorithm for position estimation for a cross tunnel thruster-enabled REMUS 100 AUV. The hydrodynamic model provides the capability of simulating vehicle docking with variable environmental effects. The filtering algorithm looks to provide an integrated solution of inertial navigation measurements and UBSL measurements to provide a more accurate vehicle location during docking operations.

14. SUBJECT TERMS terminal homing, REMUS 100, USBL, UKF, hydrodynamic model, position estimation filtering	**15. NUMBER OF PAGES** 121
	16. PRICE CODE

17. SECURITY CLASSIFICATION OF REPORT	**18. SECURITY CLASSIFICATION OF THIS PAGE**	**19. SECURITY CLASSIFICATION OF ABSTRACT**	**20. LIMITATION OF ABSTRACT**
Unclassified	Unclassified	Unclassified	UU

NSN 7540-01-280-5500 Standard Form 298 (Rev. 2-89) Prescribed by ANSI Std. 239-18

THIS PAGE INTENTIONALLY LEFT BLANK

Approved for public release; distribution is unlimited

TERMINAL HOMING FOR AUTONOMOUS UNDERWATER VEHICLE DOCKING

Eric B. Bermudez
Ensign, United States Navy
B.S., United States Naval Academy, 2015

Submitted in partial fulfillment of the
requirements for the degree of

MASTER OF SCIENCE IN MECHANICAL ENGINEERING

from the

NAVAL POSTGRADUATE SCHOOL
June 2016

Approved by: Dr. Douglas Horner
Thesis Advisor

Dr. Noel Du Toit
Second Reader

Dr. Garth Hobson
Chair, Department of Mechanical and Aerospace Engineering

THIS PAGE INTENTIONALLY LEFT BLANK

ABSTRACT

The use of docking stations for autonomous underwater vehicles (AUV) provides the ability to keep a vehicle on station, conducting missions for extended periods of time, with limited human interaction. However, the use of a docking station brings about challenges associated with terminal homing, position estimation, and vehicle control. A traditional single propeller-driven AUV must dock at a high relative approach velocity to maintain controllability, which can lead to serious damage to the AUV and the docking station. Alternatively, equipping a AUV with forward and aft pairs of horizontal and vertical cross-tunnel thrusters enables a hovering capability and allows for a slower, more deliberate approach that can help reduce potential damage during the terminal homing phase. Additionally, the commonly used ultra-short baseline (USBL) acoustic transponder attached to the docking station, which provides bearing and range measurements, can be asynchronous and sparse. The integration of these measurements into an optimal position estimation filter can potentially produce inaccuracies that are detrimental during docking operations. This thesis discusses the development of a hydrodynamic model and a filtering algorithm for position estimation for a cross tunnel thruster-enabled REMUS 100 AUV. The hydrodynamic model provides the capability of simulating vehicle docking with variable environmental effects. The filtering algorithm looks to provide an integrated solution of inertial navigation measurements and UBSL measurements to provide a more accurate vehicle location during docking operations.

THIS PAGE INTENTIONALLY LEFT BLANK

TABLE OF CONTENTS

LIST OF FIGURES

THIS PAGE INTENTIONALLY LEFT BLANK

LIST OF TABLES

THIS PAGE INTENTIONALLY LEFT BLANK

LIST OF ACRONYMS AND ABBREVIATIONS

ADCP	Acoustic Doppler Current Profiler
AUV	Autonomous Underwater Vehicle
CAVR	Center for Autonomous Vehicle Research
DOF	Degree of Freedom
DR	Dead Reckoning
DVL	Doppler Velocity Log
EKF	Extended Kalman Filter
GPS	Global Positioning System
INS	Inertial Navigation System
KF	Kalman Filter
LBL	Long Baseline
MBARI	Monterey Bay Aquarium Research Institute
NED	North East Down
NPS	Naval Postgraduate School
ODE	Ordinary Differential Equation
PF	Particle Filter
PUC	Positional Uncertainty
REMUS	Remote Environmental Measuring Units
RPM	Rotations per Minute
SNAME	Society of Naval Architects and Marine Engineers
UKF	Unscented Kalman Filter
USBL	Ultra-short Baseline
USL	Unmanned Systems Lab
UUV	Unmanned Underwater Vehicle
WHOI	Woods Hole Oceanographic Institute

THIS PAGE INTENTIONALLY LEFT BLANK

ACKNOWLEDGMENTS

First and foremost, I would like to thank my family and friends for supporting me throughout this past year. I could not have completed this thesis without them. Next, I would like to thank and acknowledge my advisor, Dr. Douglas Horner, for consistently giving up his time to help and guide me throughout the entire thesis process. I would also like to thank Sean Kragelund, Noel Du Toit, and Aurelio Monarrez for their assistance throughout my time here at NPS.

THIS PAGE INTENTIONALLY LEFT BLANK

I. INTRODUCTION

A. MOTIVATION FOR THIS WORK

Unmanned Underwater Vehicles (UUV) have been part of inventories for Navies around the world for several decades [1]. However, the known extent of the usefulness of these vehicles has largely grown within the last 10–15 years. A report to the Chief of Naval Operations in 2001 believed that UUVs may augment or completely replace divers and mammals in the coming future due to their mission duration time, reduced risk-management, and cost effectiveness [2]. A renewed focus was put on UUV development and implementation during the 2000s. This resulted in research and development of new capabilities that included exploring the feasibility of using UUVs for inspecting ship hulls, surveying water columns and bottom type, testing non-GPS reliant navigation techniques, and expanding mine counter measure efforts [3].

This ongoing discovery of potential uses however is consistently plagued by one aspect of the underwater domain, accurate navigation. Above the water, light and electromagnetic signals travel well through air and space, mediums that allow for a variety of localization systems for vehicles, the primary method being the Global Positioning System (GPS). However, the characteristic properties of air and space that make them good mediums for these signals, do not carry over to the undersea domain. Compared to air or space, water inhibits the passage of light and electromagnetic signals, and drastically reduces the effectiveness of electro-optical and electromagnetic sensors. This essentially eliminates the use of GPS navigation while submerged. The only signal that performs adequately in water is sound. As a consequence, many UUV systems rely on acoustic beaconing systems that, due to the oceanographic characteristics, can be less accurate and can negatively impact operational flexibility. For position estimation the external beacon system augments navigational filters that use Inertial Navigation Systems (INS) and Doppler Velocity Logs (DVL).

Dead reckoning is recognized as the first and oldest form of underwater navigation dating back to David Bushnell's Turtle in 1776 and is simply the estimation of

position given a known direction and speed, which for UUV would consist of a compass heading and a correlation between propeller revolutions and forward velocity [4]. Significantly more sophisticated than DR is INS, which integrates the data collected from accelerometers and gyroscopes to accurately estimate a vehicles position given an initial starting position. Similar to surface navigation, an underwater vehicle's positional uncertainty (PUC) grows in between vehicle fixes, whether it be GPS or acoustic fixes. Unlike surface navigation, an UUV receives only an initial GPS fix at the start of a mission and relies solely on DR or INS for the extent of the mission, or until it resurfaces for another fix. The PUC for INS system on board the REMUS 100 increases at rate of roughly 0.45% distance traveled in benign conditions, which means an UUV conducting a mission for an hour at 3 knots could be over 25 meters off course. For DR models it can be significantly worse as it is difficult to factor in the effects from the environment (i.e., currents and waves), and the direction and speed measurements typical maintain a higher degree of inaccuracies. The best current method of reducing the PUC of an UUV, without surfacing for a GPS fix, is using acoustic baseline systems, specifically a long baseline line (LBL) system. This method involves deploying acoustic transponders at known locations to communicate with the UUV using sound. The vehicle sends an initial sound signal to the transponders after which the transponders send a reply message. Using Equation (1), where c is the speed of sound and t is the time it took to travel between vehicle and transponder, the vehicle can determine the distance to each transponder.

$$d = c * \delta t \tag{1}$$

These distances are then used to determine an estimate of the vehicle's location via intersecting circles shown in Figure 1, where the two position solutions, represented by the red X's, are developed from using two transponders, represented by DT4C and DT1D. While this process can provide the vehicle with a fairly accurate fix, it comes with its own limitations.

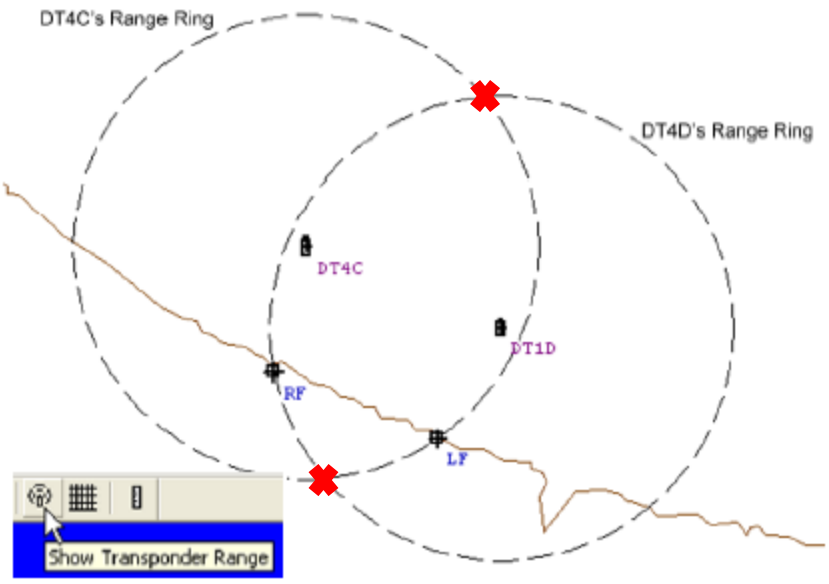

Figure 1. Position Solutions Using Two Transponders. Source: [5].

The first limitation of the acoustic baseline system is that it is an active sound system, which means it cannot be used in mission requiring discretion because it is actively putting detectable sound into the water. The second limitation of the system is that fix accuracy is greatly dependent on the geometry associated with the system setup. If the vehicle operates to close to the baseline, the line between two transponders, the vehicle can become "confused" as it is given two possible position solutions, and thus limits the operational area of the UUV given the system setup. Additionally, the acoustic system's accuracy is a function of range due to signal attenuation, which means as the distance between the vehicle and the transponder grows the accuracy decreases due to the possibility of multi-path between transmitter and receiver. As a result, acoustic baseline systems are rated to specific distances after which fix accuracy becomes no longer acceptable. The last limitation of acoustic systems is that the vehicle must have an understanding of the water and environment characteristics in order to determine the value of sound speed to accurately determine position. The predominant governing factors of sound speed are temperature, salinity, and depth, which all must be predetermined or measured by the vehicle.

Once the vehicle determines it has a fix, it must then determine whether it is accurate. This method of determining fix accuracy is another ongoing field of study in UUV navigation. It is difficult because establishing ground truth in the ocean experimentation is difficult. Still accurate vehicle position estimation is incredibly important not only for general vehicle navigation but also for the wide variety of missions UUVs can support. For missions tasks such as terrain mapping, mine detection for mine clearance operations, and vehicle docking, knowing exact positions is critical to ensure mission success.

B. PROBLEM DESCRIPTION

This thesis investigates AUV position estimation for undersea docking. The undersea platform is a Remote Environmental Measuring Units (REMUS) 100 autonomous underwater vehicle (AUV) maintained by the Center for Autonomous Vehicle Research Lab (CAVR) at the Naval Postgraduate School (NPS) in Monterey, California.

The deployment and recovery techniques of AUVs typically varies given the vehicle size and mission objective. In the case of long endurance missions it could make strategic and financial sense to keep the vehicle in the area of operation without human assistance and instead use a docking station to recharge the vehicle, download and transmit mission data, and then reprogram it for its next mission. The use of a docking station could increase mission efficiency by allowing the AUV to remain in the operational area for longer while also reducing necessary manpower and potentially necessary funding.

A difficulty experienced with the standard REMUS 100 while docking is controlling vehicle movement within close proximity to the docking station. While the initial trajectory can be within a few meters of the docking station the final trajectory must be accurate within less than one meter in order to successfully dock. For the standard REMUS 100 configuration, shown in Figure 2, these trajectory alterations are made with the pitch and rudder fins.

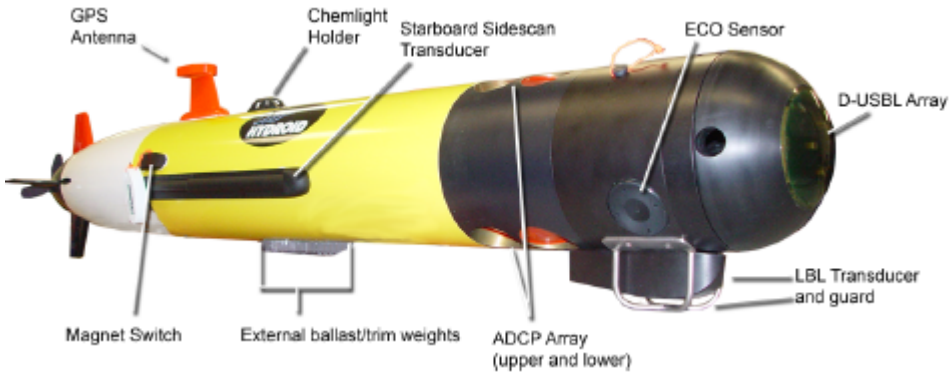

Figure 2. Standard REMUS Configuration. Source: [5].

However, given the "torpedo-like" configuration of the vehicle the fins must have a sufficient flow of water over them to provide the necessary lifts forces to steer the vehicle. For the REMUS vehicle this sufficient flow roughly equates to 2–3 knots of headway as it attempts to dock. While 2–3 knots is not seemingly a fast speed, it is fast enough to cause damage to the docking station and vehicle if the trajectory is incorrect, as seen through the partially broken guidance rails of the docking station and damaged Ultra-short Baseline (USBL) sensor in Figure 3.

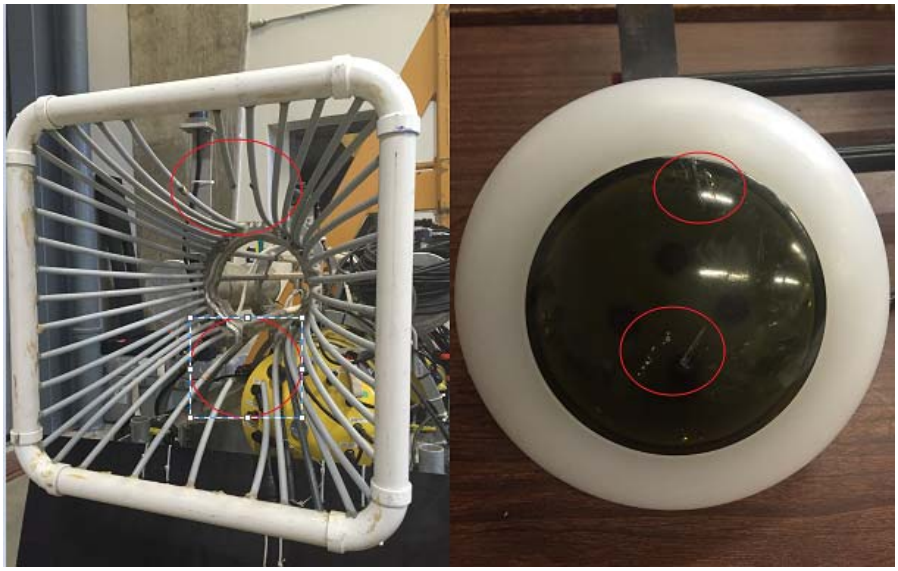

Damage caused by unsuccessful docking attempts at 2–3 knots. Damaged areas are indicated by red circles.

Figure 3. Damage Incurred from Unsuccessful Vehicle Docking

A solution to this problem was to reconfigure the REMUS vehicle to include horizontal and vertical cross-body thrusters in the forward and aft sections, seen in Figure 4.

Figure 4. Updated, Non-Standard REMUS Configuration

The cross-body thrusters allow for higher control capability at slower forward velocities, which looks to help reduce potential vehicle and docking station damage and increase docking efficiency. However, given the non-standard vehicle configuration of the REMUS 100, the developed hydrodynamic simulation models are no longer accurate and must be altered to reflect the new configuration. To gain a larger understanding of the capabilities of the new REMUS 100 configuration this thesis looks to develop a new hydrodynamic simulation model that incorporates the larger vehicle parameters as well as the tunnel thrusters.

As discussed previously, an AUVs PUC increases after the initial vehicle fix. Unless the PUC is reduced through additional vehicle fixes, the vehicle will begin the docking task with a potentially inaccurate positional estimate. Therefore, the initial trajectory the vehicle uses to approach the docking station will be inaccurate and needs to be corrected in order to successfully dock. The current method used by the REMUS 100 is an on board filtering algorithm that determines, what it believes to be, the most accurate position estimate by incorporating all available sensor information. However, past experience conducting docking operations has shown that this on board position estimation filter is not necessarily accurate. These inaccuracies also contribute to the vehicle damage shown in Figure 3. Due to the proprietary nature of the REMUS software and therefore the filtering algorithm it is not fully known how the vehicle determines a positional estimate. In order to gain greater clarity and ultimately gain greater accuracy,

the position estimate using the REMUS 100 sensor systems was also investigated in this thesis. The specific REMUS 100 sensor systems incorporated into this filtering process were the INS, USBL, and the Acoustic Doppler Current Profiler/Doppler Velocity Log (ADCP/DVL).

Given the growing error in the INS solution and the potential errors associated with the USBL solution, the problem arises on how best to filter the two systems into providing an accurate estimate of position as the vehicle approaches the docking station. The combination of an INS and USBL system generate an additional difficulty, which is they operate at different frequencies causing asynchronous data generation. Additionally, data collected from previous REMUS missions show frequent intermittent data generation performance with the USBL system, which adds complexity to the asynchronous behavior. While a variety of filtering algorithms exist that can combine several sets of data to develop a combined solution, much less have been developed that can handle several sensors with asynchronous and intermittent data generation. While it was initially believed that the INS velocities would be more accurate than the velocities measured by the integrated ADCP/DVL sensor system, the ADCP/DVL velocities were tested in the filtering process nonetheless.

C. LITERATURE REVIEW

The following sections seeks to outline the current status of the specific areas to be investigated in this thesis. A primary intention of this thesis is to not completely reinvent docking stations, hydrodynamic models, or position filters but rather work to improve the current methods. Keeping this primary intention in mind, the organization of this literature review consists of three discussion areas: the current status of UUV hydrodynamic models, the current docking stations in use or being tested, and the current methods of data or sensor filtering, specifically related to position estimation.

1. Hydrodynamic Models

A large area of study within undersea environment is the study and development of motion models for underwater vehicles. A leader in the field of underwater vehicle motion is Fossen, whose 6 degree of freedom (DOF) motion model is widely accepted

and used a starting point for maritime vehicle models [6]. Fossen's general model requires further development and calculation of a variety of coefficients, for specific platforms. These coefficients have been developed for the REMUS 100 AUV by Prestero [7] and further tested and presented by Sgarioto [8]. A limitation with these models is that they are developed around the standard REMUS 100 configuration, and the configuration of the CAVR REMUS used in this thesis is approximately double the length and mass. In order to successfully apply these developed models, the vehicle coefficients must be altered to fit the larger vehicle parameters A thesis recently presented by Doherty [9]. redeveloped Fossen's coefficients using Prestero's method for the CAVR REMUS in nearly the exact same configuration. The only difference between Doherty's configuration and the configuration presented in this thesis is the nose end cap for Doherty was a forward looking sonar instead of an USBL. Therefore, Sgarioto's model and MATLAB code in conjunction with Doherty's coefficients serves as the most accurate baseline to use in the development of a motion model to the current REMUS configuration.

Another limitation of the Fossen model is the limited discussion on the thruster force developed by the vehicle's propulsion system. Several models have been presented to fill this void but the three-state thruster model developed by Blanke et al. [10] and then further applied specifically to the REMUS 100 by Sgarioto [8] was determined to provide the most thorough solution and was used as a baseline thruster model for the aft thruster for this thesis.

2. Docking Station

The concept of docking a AUV in a docking station to recharge, download data, and reprogram has been widely studied over in recent years. The original producers of the REMUS 100 vehicle used in this thesis developed and tested their own docking station [11], which was subsequently put into production and is used in this thesis as the docking station. The docking station design created by Wood Hole Oceanographic Institution (WHOI), shown later in Figure 11, is a fairly small and compact design and easily deployable and functional in a variety of locations. The basic design and shape of

the docking station is also fairly common as similar docking stations developed by the Monterey Bay Aquarium Research Institute (MBARI) [12] and by researchers at Zhejiang University in China [13], which are shown in Figures 5 and 6, respectively, are seen to resemble and use similar systems.

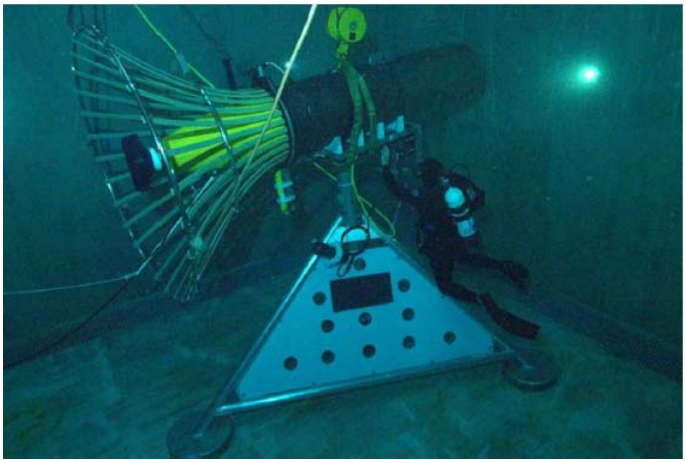

Figure 5. MBARI Docking Station. Source: [12].

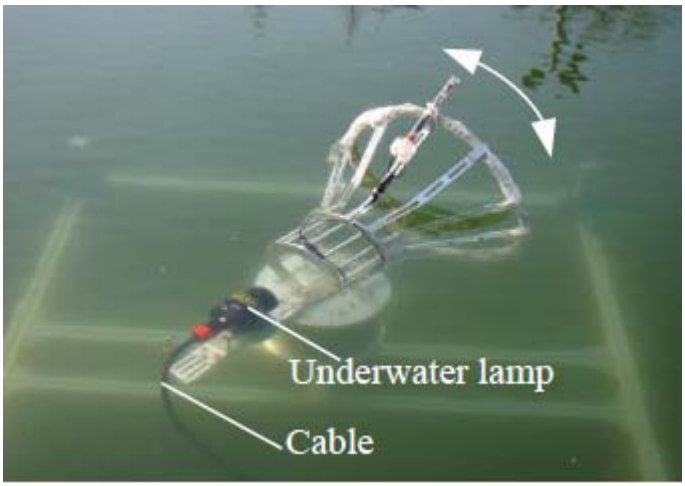

Figure 6. Zhejiang University Docking Station. Source: [13].

MBARI research results cover several similar aspects that are investigated in this thesis, namely the use of USBL for terminal homing and the development of a control algorithm for cross track error control during the terminal docking approach. The approach differs from the WHOI docking station in that the MBARI docking station

maintains thrusters that allow the docking station to pivot to compensate for error in the AUV terminal approach. Additionally, as seen in Figure 6, the researchers at Zhejiang University are operating their vehicle at the surface and therefore have high video quality as well as access to GPS.

3. Position Estimation Filtering

There is little research with respect to undersea position estimation during terminal homing. As a result, the literature research was expanded to look for filtering approaches to specific aspects of the terminal homing problem, specifically handling asynchronous data measurements and combining the outputs of several sensor systems. Additionally, research was conducted to determine what specific type of filters would serve the positional estimation problem for terminal homing best.

As previously discussed, a large difficulty with the position estimation for terminal homing of AUV sensor systems, specifically those available on the CAVR REMUS 100, is the asynchronous and intermittent behavior of the sensor data. The sensor systems on the CAVR REMUS 100 vehicle operate at different frequencies and do not always deliver usable data. A prime example is the USBL system whose performance is effected by a variety of factors including the range to the acoustic transponder and surrounding environmental conditions. As a result, USBL measurements can be sporadic and all of the vehicle's sensors' data cannot always be combined at every time step. This can result in a degraded position estimate.

Recent work pertaining to this problem has produced several potential solutions. Armesto et al. [14] developed a multi-rate fusion algorithm combining vision and inertial sensor systems for surface robot tracking with 6 DOF. The model accounts for differing sampling times by altering the measurement and output steps to reflect whether measurement data is available, and also utilizes an input hold mechanism to maintain the same input vector. The paper also compares the effectiveness of the implementing this algorithm with an EKF and UKF, and finds the UKF to be slightly more accurate but at seven times the processing cost. A similar process was conducted by Geng et al. [15] as they developed a hybrid derivative-free EKF filter for USBL and INS tightly coupled.

The derivative-free EKF combines the linear time propagation technique utilized by the standard EKF and the non-linear measurement propagation, similar to the technique utilized by the UKF. The results showed that the derivative-free EKF operated as well as the UKF for integration navigation [15]. However, the assumptions made with tightly coupled USBL and INS are not necessarily reflective for the REMUS vehicle and thus the results are not entirely applicable to this thesis.

Additional methods considered for dealing with asynchronous data as well as weighting or combining measurement estimates were presented in the works of both Syahroni [16] and Ali et al. [17]. Both papers use decentralized UKFs in a federated configuration to handle multi-sensor data fusion. The process consisted of individual UKFs that are associated with specific sensor systems that all feed into a master UKF that weighs the supporting sensor systems based on user defined coefficients. This decentralized model prevents the possibility of data overload by dispersing the data across several UKFs. The federated configuration also allows the filter to easily account for asynchronous or intermittent sensor behavior by simply adjusting the weighting coefficient for each UKF. This capability allows the master filter to operate largely uninterrupted, regardless of the sensors' operating frequencies or data quality.

The final works considered in this thesis dealt with determining what specific types of filters would best suit the position estimation problems associated with terminal homing. The first of these works was conducted in the CAVR lab research by Dillard [18]. Dillard's work focused on the positional estimation a quadcopter using bearing and range estimates to surrounding beacons. The filtering methods explored by Dillard were the extended Kalman filter (EKF) and the unscented Kalman filter (UKF) and ultimately used the UKF over the EKF. While Dillard's work showed the EKF to required less processing power, the UKF, similar was found to be able to handle the non-linearity associated with the bearing measurement better than the EKF [18]. This capability of handling non-linear measurement is believed to be a critical aspect to this thesis as the USBL measurements are non-linear in their calculation process and are sporadic in practice that results in greater non-linearity. Further works by van der Merwe et al. [19], Sarkka [20], and Allotta et al. [21] also presented an improved capability of

the UKF over the EKF while handling non-linear data. The deterministic sampling approach utilized in these works by the UKF was shown to be more realistic and less complex than the linearization used by the EKF. However, the EKF is still considered as a potential solution due to its lower required processing power as well as its capability to easily represent growing error or uncertainty with the sensor measurements.

D. THESIS ORGANIZATION

This thesis is organized as follows: Chapter II provides a description of the specific equipment and sensors used in this thesis, Chapter III delves into the governing equations and development process of the hydrodynamic model, Chapter IV delves into the governing filter equations and filter development process, Chapter V presents the results of hydrodynamic model and filtering process, and Chapter VI provides conclusions as well as recommendations for future work.

II. SYSTEM DESCRIPTION

A. REMUS 100

The standard REMUS 100, shown in Figure 2, was developed by WHOI and produced by the Kongsberg Company and is a man-portable, shallow water vehicle designed for a variety of operations that include

- hydrographic surveys,
- mine counter measure operations,
- harbor security operations,
- environmental monitoring,
- debris field mapping,
- search and salvage operations, and
- scientific sampling and mapping. [5]

The AUVs are rated to operate in depths up to 100 meters, range between 2 and 2.5 meters in length, and weigh between 50 and 65 kilograms. Table 1 further explains the REMUS 100 specifications.

Table 1. REMUS 100 Vehicle Specifications. Source: [5].

Physical/Functional Area	Characteristic	
	Metric	**US**
Vehicle Diameter	19 cm	7.5 in
Vehicle Length	2.22 m	7.28 ft
Vehicle Length with Forward looking Sonar	2.72 m	8.94 ft
Vehicle Length with Large USBL Attachment	2.48 m	8.14 ft
Vehicle Length with Small USBL Attachment	2.26 m	7.41 ft
Weight in air	52 kg	114.6 lbs
Weight in air with Forward looking Sonar	64.5 kg	142.2 lbs
Weight in Air with Large USBL Attachment	58.4 kg	128.8 lbs
Weight in Air with Small USBL Attachment	52.5 kg	115.6 lbs
External Ballast Weight	1 kg	2.2 lbs
Operating Depth Range	3 m to 100 m	10 ft to 328 ft
Typical Search Area	1200 m X 1000 m	1312 yds X 1083 yds
Rated Transponder Range	2000 m	2187 yds
Rated Acoustic Communications Range	2000 m	2187 yds
Operational Temperature		
In Air:	-24 to +43 deg C	-11.2 to +109 deg F
In Water:	-2 to +43 deg C	+28 to +109 deg F
Speed Range	0.25 to 2.57 m/s	1.0 to 4.0 knots
Maximum Operating Water Current	1.0 m/s	2 knots
Max Recommended Operating Sea State	Sea State 3	
Battery	1 kWh internally-rechargeable Lithium-ion	
Typical Endurance	20 hrs at 2 knots;9 hours at 4 knots	
Propulsion	Direct drive DC brushless motor directly connected to open three bladed propeller	
Control	2 coupled yaw and pitch fins	
Navigation Modes	Long baseline, ultra short baseline, dead reckoning, GPS	

The specific REMUS 100 vehicles used throughout this thesis, shown in Figure 8, are modified versions of the REMUS 100 AUV, and supplied by CAVR. The two REMUS vehicles used in this thesis are referred to by their vehicle numbers 231 and 359. The two vehicles are nearly identical except that vehicle 359 is Wi-Fi enabled while vehicle 231 is not.

Figure 7. Vehicle -231 with D-USBL Nose Attachment

Each vehicle operates with the following sensors and systems, [5]:

- downward looking acoustic Doppler current profiler (ADCP) and Doppler velocity log (DVL)
- acoustic modem
- magnetic compass
- NMEA 183 GPS/ Iridium antenna
- forward and aft, horizontal and vertical cross-body tunnel thrusters,
- YSI-600 conductivity, temperature, and depth sensor
- Marine Sonic Technology Limited dual frequency sidescan sonar
- Kearfott INS
- modular end cap with optional Digital USBL (D-USBL), video camera recorder, and forward looking sonar attachments

The three sensor systems critical to this thesis are the D-USBL, Kearfott INS, ADCP/DVL. However, the primary sensor system investigated in this thesis is an acoustic baseline system known the USBL. The USBL system is attached to the nose of the AUV, shown in Figure 7, and communicates with a transponder attached to the docking station. The USBL receives the docking station signal and through a four-channel planar hydrophone array determines the bearing and range to the docking station, thus obtaining a vehicle fix. However, the accuracy of the USBL tends to degrade faster than a LBL system as the range from the transponder increases. The setup of the hydrophone array also requires the docking station signal to be within a 35 degree swath

in front of the vehicle in order to achieve a successful fix. As a result signals received outside of this swath can be fairly inaccurate. Figure 8 shows the specific setup necessary for successful USBL fixes between the docking station and the AUV. Further sensor specifications are shown in Table 2.

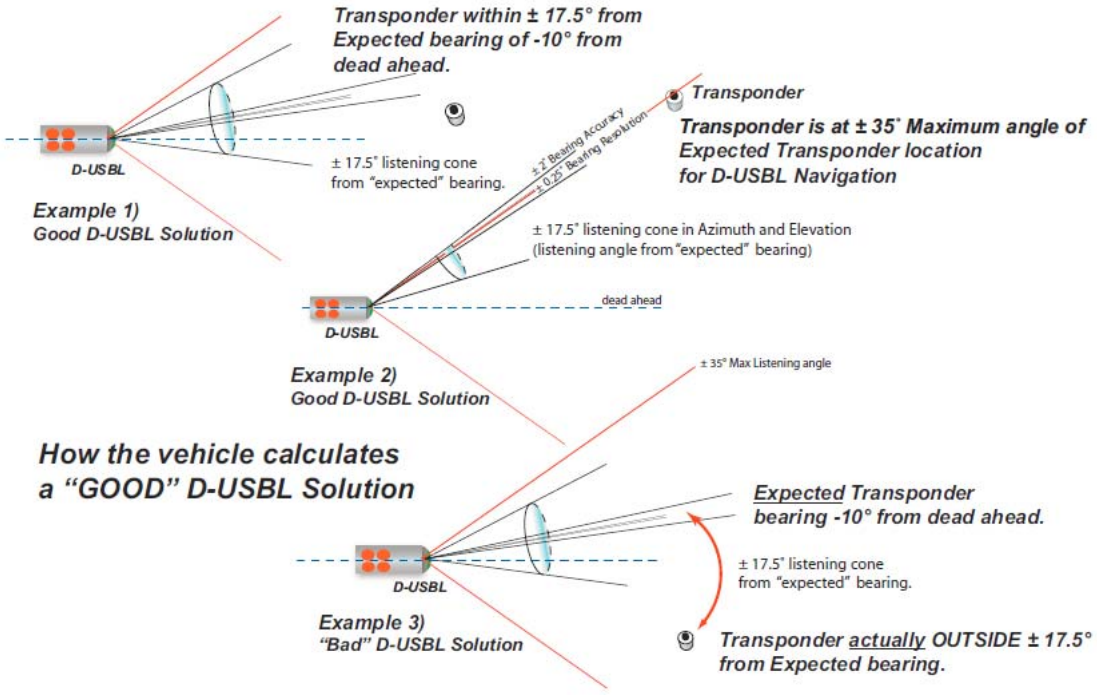

Figure 8. USBL Specifications for Determining Good Fixes. Source: [5].

Table 2. D-USBL Performance Specifications. Source: [5].

Physical/Functional Area	Characteristic	
	Metric	**US**
D-USBL Navigation Accuracy without GPS error	± 2 degrees, ±1 m (limited by compass)	± 2 degrees, ± <3 ft (limited by compass)
D-USBL Navigation Resolution	less than 1 m	less than 3 ft
D-USBL Max Range Between Vehicle and Transponder	1500 m typical	1640 yds
D-USBL - Transponder Interrogation Rate	≥ 1.5 seconds between pings	
Frequency Range	20-30 kHz	
Bearing Accuracy	± 2.5 degrees	
Bearing Resolution	± 0.25 degrees	
Listening Angle	± 17.5 degrees	
Beamwidth in azimuth and elevation	± 35 degrees	
Range (travel time) Accuracy	± 1 ms	
Range (travel time) Resolution	± 80 µs	

The Kearfott SeaDeViL INS is an integrated system that merges the ADCP, DVL, GPS, and accelerometer sensors using a Kalman filter. To help reduce the PUC the system uses GPS while surfaced to obtain position and velocity estimates, and the ADCP and DVL to obtain currents and speed over ground while submerged. The system specifications are shown in Table 3.

Table 3. Kearfott SeaDeViL INS System Specifications. Source: [22].

Physical/Functional Area	Characteristic	
	Metric	**US**
Size	$8.85*10^{-3}$ m^3	540 in^3
Weight	< 7.25 kg	< 16 lbs
Power	< 30 watts @Vdc	
Operational Ranges		
Acceleration	> 30 g's	
Attitude (Roll,Pitch, Yaw)	Unlimited	
Attitude Acceleration	>10,000 deg/s^2	
Temperature	-40°C to +55 °C	40°F to +131°F
Navigation/Attitude Performance		
Position Accuracy	0.5% DT CEP	
Heading Accuracy	5.0 mils RMS	
Roll/Pitch	0.5 mils RMS	

CEP=Circular Error Probable, DT=Distance Traveled, RMS=Root Mean Squared

B. DOCKING STATION

The docking station used for docking operations with the REMUS vehicle is shown in Figure 9. The docking station was developed and provided by WHOI to CAVR. The docking station is fairly simple in its design to allow for easy deployment and recovery by divers. The design consists of a 9.6 kWh battery capable of running the docking station and recharging the REMUS, a linear actuator with guide pins to connect the AUV to the docking station, an acoustic beacon to provide terminal homing capability, and two ballast tanks capable of being filled by a diver's breathing apparatus [11]. The AUV enters the docking station through a square opening, 0.62 meters in length, and then with help from guidance rails travels into the ultimate docking position, a cylindrical chamber approximately 0.22 meters in diameter and .93 meters in length. Once successfully in the docking station, the linear actuator will guide the connecting cable to the AUV in order for the docking station and third party users to access the vehicle. The docking station has the capability of recharging the REMUS vehicle up to ten times. A camera system is also built into the docking station that allows third parties to view the docking attempts of the vehicle. In order to access this camera

feed as well as the vehicle when it is docked, the docking station is equipped with a cable attachment to a surface buoy. From this surface buoy third parties can access the vehicle and docking station through direct or Iridium connections.

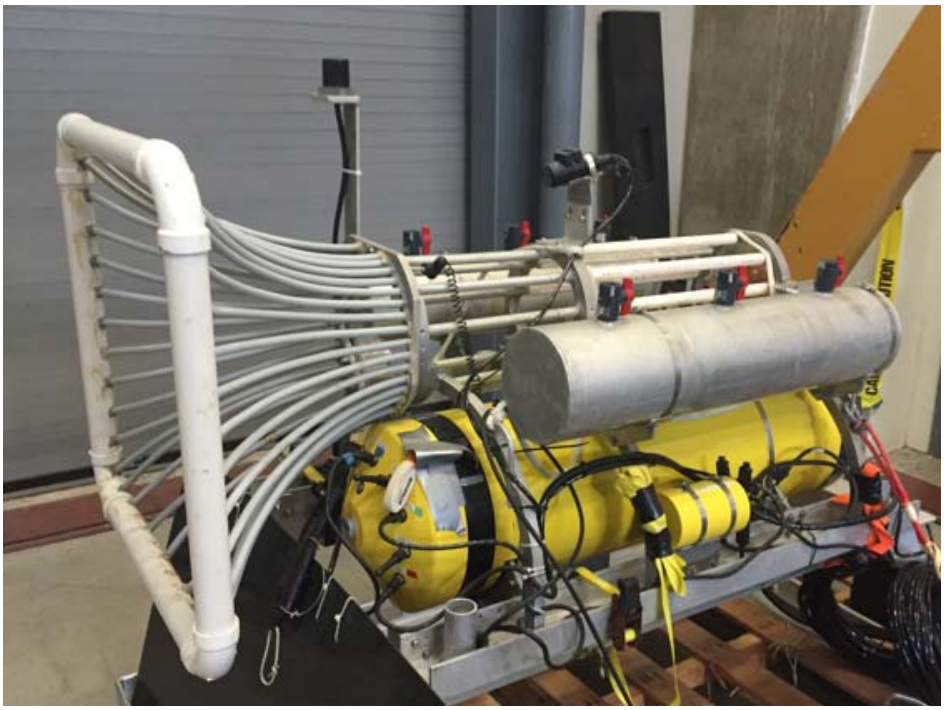

Figure 9. CAVR Docking Station for REMUS 100 AUV

THIS PAGE INTENTIONALLY LEFT BLANK

III. REMUS 100 HYDRODYNAMIC MODELING WITH FORE AND AFT TUNNEL THRUSTERS

A. INTRODUCTION

This section discusses the development of the non-linear hydrodynamic simulation model for the new CAVR REMUS 100 configuration with cross tunnel thruster. The full derivation of the majority of the governing equations are not included in this thesis as they have been developed extensively in several other works, which includes [6], [7],and [9]. This thesis provides the resulting equations from these previous works as well as the full development of novel additions specific to the CAVR REMUS 100 configuration. These novel additions include a realistic aft thruster model, a realistic tunnel thruster model, and hydrodynamic coefficients specific to the vehicle configuration at varying speeds.

B. MODEL BACKGROUND

1. Assumptions

In order to develop the vehicle simulation model several assumptions concerning the vehicle and the surrounding environment were taken in order to simplify some of the complexities associated with the underwater domain. These assumptions are as follows:

- The AUV is assumed to be a single rigid body with constant mass.
- The AUV operates in a homogeneous fluid free from surface, bottom, or wave effects with only linear effects from currents.
- Rotational effects from the Earth as well as local gravitational variances are assumed negligible.
- The types of external forces acting on the vehicle are inertial, gravitational, hydrostatic, hydrodynamic and propulsive.

2. Reference Frame

The 6 DOFs that are incorporated into the presented hydrodynamic model are presented in Table 4 in accordance with the Society of Naval Architects and Marine Engineers (SNAME) standard notation [23].

Table 4. 6 Degrees of Freedom Notation Used with REMUS AUV

Degree of Freedom	Motion Description	Kinetics	Velocity	Displacement
1	*Surge*, motion along x-axis	X	u	x
2	*Sway*, motion along y-axis	Y	v	y
3	*Heave*, motion along z-axis	Z	w	z
4	*Roll*, rotation about x-axis	K	p	ϕ
5	*Pitch*, rotation about y-axis	M	q	θ
6	*Yaw*, rotation about z-axis	N	r	ψ

In order to best represent the position, orientation, and motion of the AUV two orthogonal reference frames are utilized. The first frame is the global inertial frame which is fixed with respect to the center of the earth. This frame is used to display the position and orientation of the vehicle. The second reference frame is a body frame with an origin fixed at the center of buoyancy of the vehicle. The body frame allows to more simply show the linear and angular velocities of the vehicle as the principal axes are aligned with the principal direction of vehicle motion. Both the global and body frames are right-handed reference frames oriented in the North, East, and Down (NED) configuration, and are shown along with the respective degrees of freedom in Figure 10

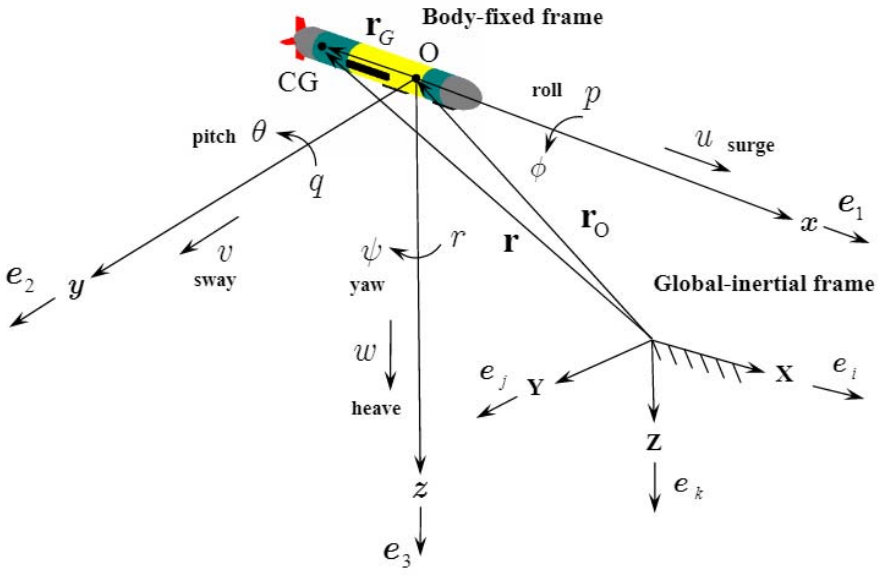

Figure 10. Reference Frames and Degrees of Freedom of AUV. Source: [8]

C. EQUATIONS OF MOTION

The equations of motion for the REMUS AUV are developed in the body-fixed frame utilizing both Newton's second law of motion and Euler's rigid body equations:

$$\sum \boldsymbol{F} = \mathbf{m} * \boldsymbol{a} \tag{2}$$

$$\sum \boldsymbol{M} = \mathbf{I} * \boldsymbol{\omega} \tag{3}$$

where the external forces (F) are developed from the product of mass (m) and acceleration (a) and moments (M) are developed from the product of the inertia (I) and the angular acceleration (ω). The external forces and moments can then be broken down into hydrostatic (HS) , added mass (A) , hydrodynamic damping (HD) , lift (L) , and propulsive (P) components:

$$\sum \boldsymbol{F} = F_{HS} + F_A + F_{HD} + F_L + F_P \tag{4}$$

$$\sum \boldsymbol{M} = M_{HS} + M_A + M_{HD} + M_L + M_P \tag{5}$$

The translational equations of motion, X, Y, and Z, are derived by setting the sum of all external forces equal to the product of mass and the inertial acceleration about the

vehicle's center of mass. This inertial acceleration is derived by first obtaining the derivative of the position vector (r_G) to determine the velocity vector where the position vector is the distance from the center of buoyancy to the center of gravity.

$$\mathbf{r_G} = [x_G \;\; y_G \;\; z_G]^T \tag{6}$$

$$\boldsymbol{\omega} = [p \; q \; r]^T \tag{7}$$

$$\mathbf{v} = [u \; v \; w]^T \tag{8}$$

$$\mathbf{v} = \dot{\mathbf{r}} = \mathbf{v}_0 + (\boldsymbol{\omega} \times \mathbf{r_G}) \tag{9}$$

The derivative of the velocity vector is then obtained resulting in the acceleration vector (a).

$$\mathbf{a} = \dot{\mathbf{v}} = \mathbf{a}_0 + (\dot{\boldsymbol{\omega}} \times \mathbf{r_G}) + (\boldsymbol{\omega} \times (\boldsymbol{\omega} \times \mathbf{r_G})) + (\boldsymbol{\omega} \times \mathbf{v}) \tag{10}$$

After substituting in the variables and carrying out the mathematic operations the acceleration vector results in:

$$\mathbf{a} = \begin{bmatrix} \dot{u} - vr + wq - x_G(q^2 + r^2) + y_G(pq - \dot{r}) + z_G(pr + \dot{q}) \\ \dot{v} - wp + ur - y_G(r^2 + p^2) + z_G(qr - \dot{p}) + x_G(qp + \dot{r}) \\ \dot{w} - uq + vp - z_G(p^2 + q^2) + x_G(rp - \dot{q}) + y_G(rq + \dot{p}) \end{bmatrix} \tag{11}$$

which can then be combined with the mass of the vehicle to develop the full translational equations of motion:

$$\sum \mathbf{F} = \begin{bmatrix} \sum X \\ \sum Y \\ \sum Z \end{bmatrix} = \mathbf{m} \begin{bmatrix} \dot{u} - vr + wq - x_G(q^2 + r^2) + y_G(pq - \dot{r}) + z_G(pr + \dot{q}) \\ \dot{v} - wp + ur - y_G(r^2 + p^2) + z_G(qr - \dot{p}) + x_G(qp + \dot{r}) \\ \dot{w} - uq + vp - z_G(p^2 + q^2) + x_G(rp - \dot{q}) + y_G(rq + \dot{p}) \end{bmatrix} \tag{12}$$

A similar process is conducted to derive the rotational equations of motion, K, M, and N, by obtaining the derivative of the angular momentum about the vehicle's center of

mass and setting it equal to the sum of the external moments acting on the vehicle. Angular momentum is defined as:

$$\mathbf{H} = \mathbf{I} \cdot \boldsymbol{\omega} \tag{13}$$

where I is the inertia tensor of the vehicle

$$\mathbf{I} = \begin{bmatrix} I_{xx} & I_{xy} & I_{xz} \\ I_{yx} & I_{yy} & I_{yz} \\ I_{zx} & I_{zy} & I_{zz} \end{bmatrix} \tag{14}$$

Obtaining the derivation of the angular momentum and applying Newton's second law results in:

$$\sum \mathbf{M} = \dot{\mathbf{H}} = \mathbf{H}_0 + (\mathbf{r_G} \times \mathbf{ma}) = \mathrm{I}\dot{\boldsymbol{\omega}} + (\boldsymbol{\omega} \times \mathbf{H}_0) + \mathbf{m}((\mathbf{r_G} \times \dot{\mathbf{v}}) + \mathbf{r_G} \times (\boldsymbol{\omega} \times \mathbf{v})) \tag{15}$$

After substituting in the proper variables and carrying out the mathematic operations the resulting rotational equations of motion are:

$$\sum \mathbf{M} = \begin{bmatrix} \sum K \\ \sum M \\ \sum N \end{bmatrix} = \tag{16}$$

$$\begin{bmatrix} I_{xx}\dot{p} + (I_{zz} - I_{yy})qr - (\dot{r} + pq)I_{xz} + (r^2 - q^2)I_{yz} + (pr - \dot{q})I_{xy} + m(y_G(\dot{w} - uq + vp) - z_G(\dot{v} - wp + ur)) \\ I_{yy}\dot{q} + (I_{xx} - I_{zz})\mathrm{rp} - (\dot{\mathrm{p}} + qr)I_{xy} + (\mathrm{p}^2 - r^2)I_{zx} + (\mathrm{qp} - \dot{r})I_{yz} + m(z_G(\dot{\mathrm{u}} - vr + wq) - x_G(\dot{\mathrm{w}} - uq + vp)) \\ I_{zz}\dot{r} + (I_{yy} - I_{xx})\mathrm{pq} - (\dot{\mathrm{q}} + rp)I_{yz} + (\mathrm{q}^2 - p^2)I_{xy} + (\mathrm{rq} - \dot{p})I_{zx} + m(\mathrm{x}_G(\dot{\mathrm{v}} - wp + ur) - y_G(\dot{\mathrm{u}} - vr + wq)) \end{bmatrix}$$

In order to simplify the equations of motion it is assumed that the off diagonal values in the inertia tensor are very small and can therefore be neglected. Similarly, the x and y distance values from the center of buoyancy to the center of gravity are assumed to be negligible. These assumptions lead to the following simplified equations:

$$\sum \mathbf{F} = \begin{bmatrix} \sum X \\ \sum Y \\ \sum Z \end{bmatrix} = m \begin{bmatrix} \dot{u} - vr + wq + z_G(pr + \dot{q}) \\ \dot{v} - wp + ur + z_G(qr - \dot{p}) \\ \dot{w} - uq + vp - z_G(p^2 + q^2) \end{bmatrix} \tag{17}$$

$$\sum \mathbf{M} = \begin{bmatrix} \sum K \\ \sum M \\ \sum N \end{bmatrix} = \begin{bmatrix} I_{xx}\dot{p} + (I_{zz} - I_{yy})qr - mz_G(\dot{v} - wp + ur) \\ I_{yy}\dot{q} + (I_{xx} - I_{zz})\,\mathrm{rp} + m\,\mathrm{z}_G(\dot{\mathrm{u}} - vr + wq) \\ I_{zz}\dot{r} + (I_{yy} - I_{xx})\,\mathrm{pq} \end{bmatrix} \tag{18}$$

D. FORCE AND MOMENT COMPONENTS

Using the underwater vehicle model from Fossen [6] as a framework, the force and moment components fall into five distinct categories for underwater vehicles. These force and moment categories are hydrostatic, added mass, hydrodynamic damping, lift, and propulsive. This section briefly describes and annotates each force and moment component, using SNAME notation, as it pertains to each degree of freedom.

1. Hydrostatic Component

The hydrostatic forces and moments are developed from the differences between the weight and buoyancy of the vehicle. The CAVR REMUS 100 is typically positively buoyant by about 3.34 N (0.75 lbs), to allow the AUV to surface if it develops any faults or problems during a mission. The center of buoyancy is also located above the center of gravity to prevent rolling of the vehicle, and if properly ballasted the distance in the x and y directions to the center of mass are negligible. Taking into considerations these vehicle characteristics the force and moment equations are [6]:

$$X_{HS} = -(W - B)\sin\theta \tag{19}$$

$$Y_{HS} = (\mathrm{W} - \mathrm{B})\cos\theta\sin\phi \tag{20}$$

$$Z_{HS} = (W - B)\cos\theta\cos\phi \tag{21}$$

$$K_{HS} = -z_G W\cos\theta\sin\phi \tag{22}$$

$$M_{HS} = -z_G W\sin\theta \tag{23}$$

$$N_{HS} = 0 \tag{24}$$

2. Added Mass Component

Added mass can be understood as pressure-induced forces and moments due to a forced harmonic motion of the AUV which is proportional to the acceleration of the body but 180 degrees out of phase [7]. Taking into consideration of the x-y and x-z symmetry of the REMUS AUV the added mass equations are [7]:

$$X_A = X_{\dot{u}}\dot{u} + X_{wq}wq + X_{qq}q^2 + X_{vr}vr + X_{rr}r^2 \tag{25}$$

$$Y_A = Y_{\dot{v}}\dot{v} + Y_{\dot{r}}\dot{r} + Y_{ur}ur + Y_{wp}wp + Y_{pq}pq \tag{26}$$

$$Z_A = Z_{\dot{w}}\dot{w} + Z_{\dot{q}}\dot{q} + Z_{uq}uq + Z_{vp}vp + Z_{rp}rp \tag{27}$$

$$K_A = K_{\dot{p}}\dot{p} \tag{28}$$

$$M_A = M_{\dot{w}}\dot{w} + M_{\dot{q}}\dot{q} + M_{vp}vp + M_{rp}rp + M_{uq}uq \tag{29}$$

$$N_A = N_{\dot{v}}\dot{v} + N_{\dot{r}}\dot{r} + N_{wp}wp + N_{pq}pq + N_{ur}ur \tag{30}$$

3. Hydrodynamic Damping Component

As the REMUS AUV moves through the water it is subject to non-linear damping primarily in the form of skin friction caused by boundary layers. These boundary layers in practice fall mainly within the turbulent region [9] and result in axial, cross flow, and rolling drag forces and moments. As a way to simplify the high non-linearity of the damping forces and moments Prestero [7] considered the following assumptions:

- Viscous hydrodynamic damping forces always oppose the motion of the vehicle.
- Ignore linear and angular coupled hydrodynamic damping.

- Drag induced hydrodynamic damping moments are neglected due to vehicle longitudinal and lateral symmetry
- Only second-order hydrodynamic damping forces and moments are retained.

Taking into consideration these assumptions the hydrodynamic damping force and moment equations are [7]:

$$X_{HD} = X_{u|u|} u \,|u| \tag{31}$$

$$Y_{HD} = Y_{v|v|} v \,|v| + Y_{r|r|} r \,|r| \tag{32}$$

$$Z_{HD} = Z_{w|w|} w \,|w| + Z_{q|q|} q \,|q| \tag{33}$$

$$K_{HD} = K_{p|p|} p \,|p| \tag{34}$$

$$M_{HD} = M_{w|w|} w \,|w| + M_{q|q|} q \,|q| \tag{35}$$

$$N_{HD} = N_{v|v|} v \,|v| + N_{r|r|} r \,|r| \tag{36}$$

4. Lift Component

The primary lift forces and moments are provided by the lateral and longitudinal stern fins. These fins are denoted by the subscript "r" for the longitudinal rudder fin and subscript "s" for the stern elevator fins. The AUV also experiences additional lift from the overall shape of the vehicle which, similar to the fin lift forces, are proportional to the x-direction velocity as well as the velocity for the respective degree of freedom it is affecting. The resulting lift forces and moments are [8]:

$$X_L = 0 \tag{37}$$

$$Y_L = Y_{uv} uv + Y_{uu\delta_r} u^2 \delta_r \tag{38}$$

$$Z_L = Z_{uw} uw + Z_{uu\delta_s} u^2 \delta_s \tag{39}$$

$$K_L = 0 \tag{40}$$

$$M_L = M_{uw} uw + M_{uu\delta_s} u^2 \delta_s \tag{41}$$

$$N_L = N_{uv}uv + N_{uu\delta_r}u^2\delta_r \tag{42}$$

5. Propulsive Component

a. Aft Thruster

The modelling of the propulsive force for underwater vehicles remains a difficult task as the propeller thrust model is highly dependent on variables that vary as a function of forward velocity. As a result of this dependency recent models, such as [24], [24],[7] or [25], typically maintain their thruster models around a single velocity. For this thesis the model in [24] was initially used:

$$T = T_{n|n|}n\,|\,n\,| = \frac{X_p}{(1-\tau_p)} \tag{43}$$

$$Q = Q_{n|n|}n\,|\,n\,| = K_p \tag{44}$$

T is the developed thrust, $T_{n|n|}$ is the mechanical motor thrust coefficient, τ_p is the thrust reduction factor, Q is the developed torque, $Q_{n|n|}$ is the mechanical torque coefficient, and n is propeller revolutions. While these models easily allow for variable propeller revolutions the mechanical torque and thrust coefficient must also vary which generates the limitation and difficulty with this model. As an initial testing, the model was used data provided via [26] that developed force and torque measurements from a REMUS 100 traveling at roughly 4.5 knots. Using this data the developed coefficients are:

$$T_{n|n|} = \frac{T}{n\,|\,n\,|} = \frac{16.01}{159.7\,|159.7\,|} = 6.279\times10^{-4} \tag{45}$$

$$Q_{n|n|} = \frac{Q}{n\,|\,n\,|} = \frac{-0.2859}{159.7\,|159.7\,|} = -1.121\times10^{-5} \tag{46}$$

where thrust is reported in newtons (N) , propeller revolutions in radians/sec, and torque in newton-meters (N-m).

In order to advance the model and incorporate cross tunnel thrusters for simulated docking operations the vehicle must be capable of operating at variable speeds. To

incorporate the speed variability within the model experimental tests were conducted with the CAVR REMUS 100 in the Unmanned Systems Lab (USL) test tank. The goal of these tests was to develop an equation correlating revolutions per minute (RPM) to developed thrust. The tests were conducted using a FUTEK strain gauge, shown in Figure 11, attached to the rear of the REMUS to measure the developed force as the RPMs were varied from 0 to 1500, approximately 157 rad/s.

Figure 11. FUTEK Strain Gauge Used for Thrust Model Development

After collecting the RPM and force measurements a fourth-order polynomial was fit to the data using MATLAB's polyfit function. The resulting polynomial fit and measured data are shown in Figure 12. Comparing the values from [26] to the values obtained during experimentation, there is a significant increase in the developed thrust, at similar propeller revolutions, for the CAVR REMUS 100. The data reported by [26] equated 159.7 rad/s, approximately 1525 RPMs, to 16.01 N, while the experimental data equated 1500 RPMs to approximately 38 N. As a result of this significant difference in developed thrust the experimentally determined polynomial was used as the propulsive force in the X direction where n is the current propeller RPM and the RPMs are capped at 1500.

$$X_P = F_{aft} = 2.93e^{-12} * \mathrm{n}^4 + -2.69e^{-9} * \mathrm{n}^3 + 7.23e^{-6} * \mathrm{n}^2 + 0.0105 * \mathrm{n} \quad (47)$$

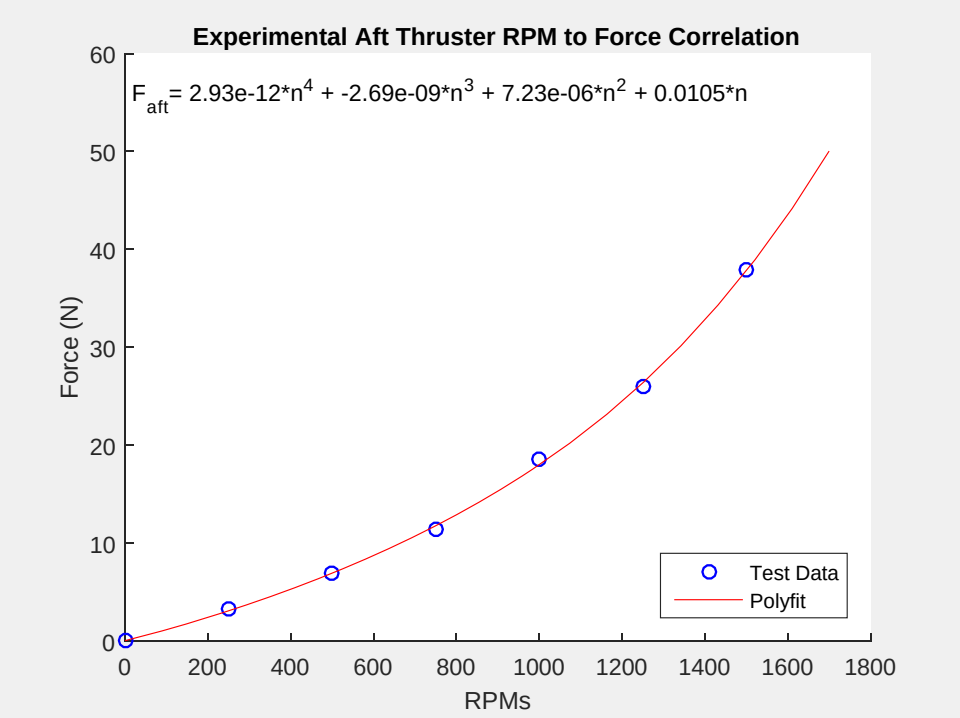

Figure 12. Experimental Results and Polynomial Fit for RPM to Thrust Correlation

Limited by lab equipment, a new torque equation was unable to be correlated to RPM. However, after reviewing previous mission data a similar 5 degree tilt, as reported in [26], was observed while the vehicle operated around 1500 RPM. As a result of this observation Equations (44) and (46) were used to define the upper limit of the developed torque and the coefficient $Q_{n|n|}$ was assumed constant. It is believed the coefficient $Q_{n|n|}$ does in fact vary with propeller rotation rate, but the difference is assumed to be negligible for the scope of this thesis.

b. Tunnel Thrusters

The CAVR REMUS 100 vehicles consist of four cross tunnel thrusters, two laterally oriented and two vertically oriented. The force developed by the tunnel thrusters is generated by a small propeller located at one end of the tunnel. Figure 13 and Figure 14 show the layout of the lateral and vertical tunnel thrusters.

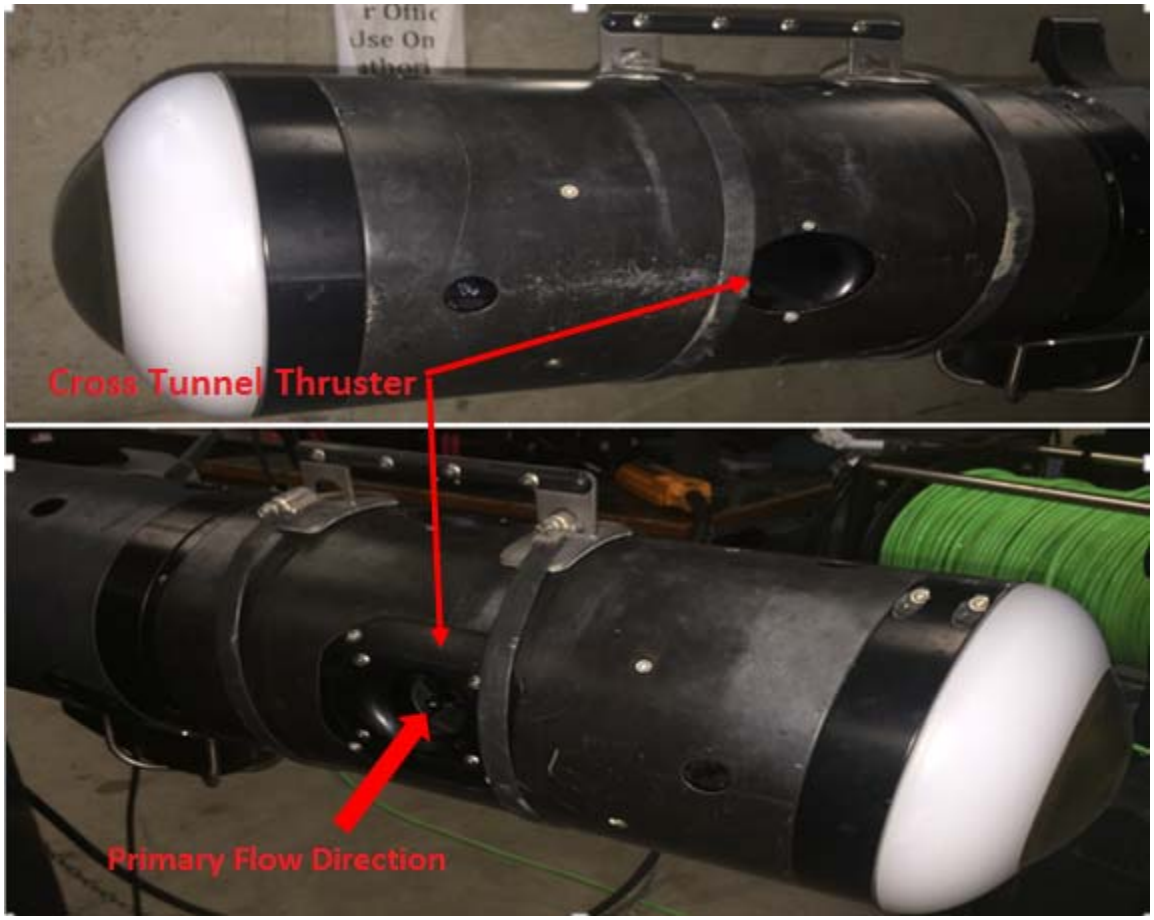

Figure 13. Forward Lateral Tunnel Thruster

Figure 14. Complete Tunnel Thruster Configuration

This small propeller is located at the bottom end of the tunnel for the vertical tunnel thrusters, the right end for the forward lateral thruster, and the left end for the aft lateral thruster. The propeller is designed to operate in both directions, but does have a

primary direction of operation where the developed force is slightly greater than the reverse direction. The primary method of operation is when the water enters the tunnel through the propeller end and is then forced out the opposite end. For the remainder of this thesis the primary operating direction will be referred to as the "forward" direction and the secondary operating direction will be referred to as the "reverse" direction.

Similar to the aft thruster, experimentally determined polynomial equations are used to model the developed thrust from the vertical and horizontal cross tunnel thrusters. The vertical tunnel thrusters for the CAVR REMUS 100 had been previously tested by Doherty in the CAVR test tank. However, Doherty's test did not take into consideration the restoring buoyancy force acting against the developed thrust from the tunnel thrusters and therefore the test results are not used in this thesis.

In order to obtain an equation correlating tunnel thruster RPM to developed force, a test similar to Doherty's was conducted. The test was conducted in the CAVR test tank and consisted of attaching one end of the FUTEK strain gauge, shown in Figure 11, to the forward handle of the REMUS vehicle and the other rigidly to the tank wall. The aft section of the vehicle was also rigidly attached to the tank wall in order to maintain vehicle stability during the test. Once the strain gauge was properly attached and zeroed out the forward lateral tunnel thruster was operated in the reverse direction by varying the RPMs from 0 to 4000. The tested reverse direction RPM values and resulting forces were then processed by the polyfit function. The test results are shown in Figure 15 and the developed polynomial function is:

$$F_{\text{rev}} = -6.85 \cdot 10^{-15} \cdot n^4 + 7.3 \cdot 10^{-11} \cdot n^3 + 9.26 \cdot 10^{-8} \cdot n^2 + 4.97 \cdot 10^{-4} \cdot n \qquad (48)$$

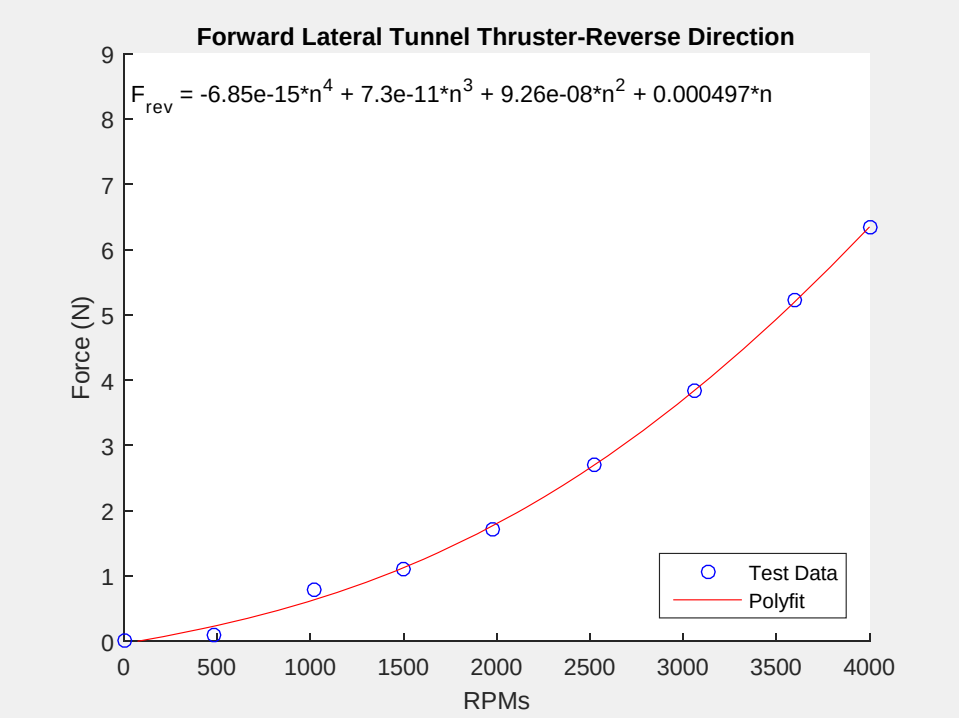

Figure 15. Experimental Results and Polynomial Fit for Reverse Thruster Direction

The same test was conducted for the forward lateral tunnel thruster in the forward operating direction by varying the RPMs from 0 to -4000. The test results are shown in Figure 16 and the developed polynomial function is:

$$F_{fwd} = 3.89 \cdot 10^{-15} \cdot n^4 + 3.5 \cdot 10^{-11} \cdot n^3 + 1.81 \cdot 10^{-7} \cdot n^2 + 3.3 \cdot 10^{-4} \cdot n \quad (49)$$

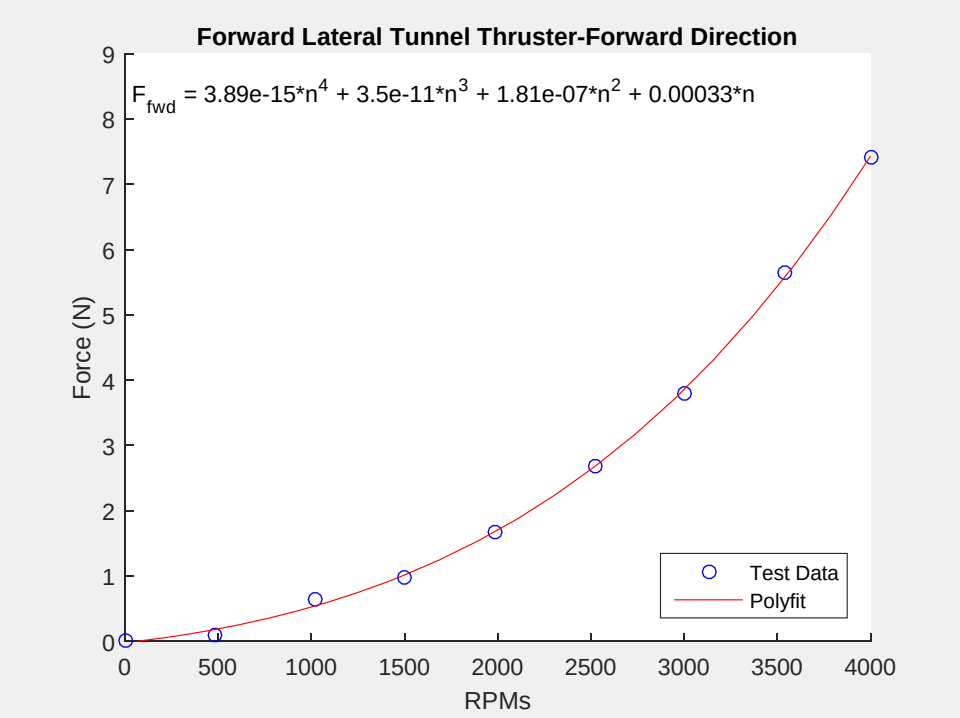

Figure 16. Experimental Results and Polynomial Fit for Forward Thruster Direction

Given the nearly identical structure of all four tunnel thrusters the assumption can be made that the force developed by the forward lateral tunnel thruster in both the forward and reverse directions can be applied to each tunnel thruster. Given the varying orientations of each tunnel thruster, the operating directions associated with positive or negative RPM commands for the forward lateral thruster is not necessarily consistent with the other three tunnel thrusters. Additionally, the sign of the RPM command does not reflect the direction of the developed force. Table 5 explains which tunnel thruster force equation is used for each cross tunnel thruster given the sign of the RPM command and the proper force sign with respect to the NED frame work.

Table 5. Applicable Force Equation for RPM Command

Tunnel Thruster	**Positive RPM**	**Negative RPM**
Forward Lateral ($F_{lat,fwd}$)	$-F_{rev}$	$+F_{fwd}$
Aft Lateral ($F_{lat,aft}$)	$-F_{fwd}$	$+F_{rev}$
Forward Vertical ($F_{ver,fwd}$)	$-F_{rev}$	$+F_{fwd}$
Aft Vertical ($F_{ver,aft}$)	$-F_{rev}$	$+F_{fwd}$

Taking into consideration the tunnel thruster orientation and the proper sign of the forces given the RPM command, the propulsive forces developed by the tunnel thrusters are:

$$Y_P = F_{lat,\,fwd} + F_{lat,aft} \tag{50}$$

$$Z_P = F_{ver,\,fwd} + F_{ver,aft} \tag{51}$$

It should be noted that the tunnel thrusters are not slaved, which means that they act independently of one another and therefore are not generating the same forces This behavior coupled with the fact that the tunnel thruster do not necessarily generate the same force given the same RPM command causes a moment about the center of buoyancy. Additionally, the vertical and lateral tunnel thrusters are not equidistant from the AUV's center of buoyancy which results in a moment about the center of buoyancy even during equal force generation. However, the vertical and lateral thrusters are assumed to act along the center line of the vehicle and therefore do not cause a roll about the x-axis. Taking into consideration these properties of the tunnel thrusters and the NED framework the moment equations are:

$$T_{ver,aft} = -(F_{ver,aft} \cdot d_{ver,aft}) \tag{52}$$

$$T_{ver,\mathrm{fwd}} = -(F_{ver,\mathrm{fwd}} \cdot d_{ver,\mathrm{fwd}}) \tag{53}$$

$$M_P = T_{vert,aft} + T_{vert,\,fwd} \tag{54}$$

$$T_{lat,\,fwd} = F_{lat,\,fwd} \cdot d_{lat,\,fwd} \tag{55}$$

$$T_{lat,\mathrm{aft}} = F_{lat,\mathrm{aft}} \cdot d_{lat,\mathrm{aft}} \tag{56}$$

$$N_P = T_{lat,\,fwd} + T_{lat,aft} \tag{57}$$

The distances from each tunnel thruster to the center of buoyancy are found in Table 6. The distances were determined while the USBL nose cone was attached.

Table 6. Distances of Each Tunnel Thruster to Center of Buoyancy

Tunnel Thruster	Distance (meters)
$d_{ver,fwd}$	0.808
$d_{ver,aft}$	-0.732
$d_{lat,fwd}$	0.852
$d_{lat,aft}$	-0.774

E. COMBINED HYDRODYNAMIC EQUATIONS OF MOTION

The hydrodynamic simulation model developed in this thesis utilizes MATLAB's ODE45 ordinary differential equation (ODE) solver to determine the motion of the CAVR REMUS 100. In order to utilize the ODE solver to develop the motion of the AUV the acceleration terms must be isolated. To accomplish this, the forces and moments are multiplied by the inverse of the mass matrix, M. Using Fossen notation [6] the mass matrix m can be broken into rigid body and added mass components:

$$\mathbf{m} = M_{RB} + M_A \tag{58}$$

where the rigid body matrix is

$$M_{RB} = \begin{bmatrix} m & 0 & 0 & 0 & mz_G & -my_G \\ 0 & m & 0 & -mz_G & 0 & mx_G \\ 0 & 0 & m & my_G & -mx_G & 0 \\ 0 & -mz_G & my_G & I_x & -I_{xy} & -I_{xz} \\ mz_G & 0 & -mx_G & -I_{yx} & I_y & -I_{yz} \\ -my_G & mx_G & 0 & -I_{zx} & -I_{zy} & I_z \end{bmatrix} \tag{59}$$

and the added mass matrix is:

$$M_A = -\begin{bmatrix} X_{\dot{u}} & X_{\dot{v}} & X_{\dot{w}} & X_{\dot{p}} & X_{\dot{q}} & X_{\dot{r}} \\ Y_{\dot{u}} & Y_{\dot{v}} & Y_{\dot{w}} & Y_{\dot{p}} & Y_{\dot{q}} & Y_{\dot{r}} \\ Z_{\dot{u}} & Z_{\dot{v}} & Z_{\dot{w}} & Z_{\dot{p}} & Z_{\dot{q}} & Z_{\dot{r}} \\ K_{\dot{u}} & K_{\dot{v}} & K_{\dot{w}} & K_{\dot{p}} & K_{\dot{q}} & K_{\dot{r}} \\ M_{\dot{u}} & M_{\dot{v}} & M_{\dot{w}} & M_{\dot{p}} & M_{\dot{q}} & M_{\dot{r}} \\ N_{\dot{u}} & N_{\dot{v}} & N_{\dot{w}} & N_{\dot{p}} & N_{\dot{q}} & N_{\dot{r}} \end{bmatrix} \tag{60}$$

Taking into account vehicle symmetry the combined mass matrix is:

$$\mathbf{m} = \begin{bmatrix} (m - X_{\dot{u}}) & 0 & 0 & 0 & mz_G & 0 \\ 0 & (m - Y_{\dot{v}}) & 0 & -mz_G & 0 & -Y_{\dot{r}} \\ 0 & 0 & (m - Z_{\dot{w}}) & 0 & -Z_{\dot{q}} & 0 \\ 0 & -mz_G & 0 & (I_x - K_{\dot{p}}) & 0 & 0 \\ mz_G & 0 & -M_{\dot{w}} & 0 & (I_y - M_{\dot{q}}) & 0 \\ 0 & -N_{\dot{v}} & 0 & 0 & 0 & (I_z - N_{\dot{r}}) \end{bmatrix} \tag{61}$$

The using the mass matrix, forces, and moments the acceleration equations are:

$$\begin{bmatrix} \dot{u} \\ \dot{v} \\ \dot{w} \\ \dot{\phi} \\ \dot{\theta} \\ \dot{\varphi} \end{bmatrix} = \mathbf{m}^{-1} \begin{bmatrix} \sum X \\ \sum Y \\ \sum Z \\ \sum K \\ \sum M \\ \sum N \end{bmatrix}, \tag{62}$$

where the full force and moment equations, after isolating the acceleration terms to the left hand side of the equation, are:

$$\begin{aligned} \sum X = &-(W - B)\sin(\theta) + (X_{wq} - m)wq + X_{qq}q^2 + (X_{vr} + m)vr + X_{rr}r^2 \\ &+ X_{u|u|}u\,|u| + F_{aft} - mz_G pr \end{aligned} \tag{63}$$

$$\begin{aligned} \sum Y = &(W - B)\cos\theta\sin\phi + (Y_{ur} - m)ur + (Y_{wp} + m)wp + Y_{pq}p + Y_{v|v|}v\,|v| \\ &+ \mathrm{Y}_{r|r|}\,r\,|r| + Y_{uv}uv + Y_{uu\delta_r}u^2\delta_r + F_{lat,fwd} + F_{lat,aft} - mz_G qr \end{aligned} \tag{64}$$

$$\sum Z = (W - B)\cos\theta\cos\phi + (Z_{uq} + m)uq + (Z_{vp} - m)vp + Z_{rp}rp + Z_{w|w|}w\,|\,\mathrm{w}\,| + Z_{q|q|}\,q\,|\,q\,| + Z_{uw}uw + Z_{uu\delta_s}u^2\delta_s + F_{ver,\,fwd} + F_{ver,aft} + mz_G p^2 + mz_G q^2 \tag{65}$$

$$\sum K = -z_G W\cos\theta\sin\phi + K_{p|p|}p\,|\,p\,| + Q - (I_{zz} - I_{yy})qr - mz_G wp + mz_G ur \tag{66}$$

$$\sum M = -z_G W\sin\theta + M_{vp}vp + (M_{rp} - (I_{xx} - I_{zz}))rp + M_{uq}uq + M_{w|w|}w\,|\,w\,| + \mathrm{M}_{q|q|}\,q\,|\,q\,| + M_{uw}uw + M_{uu\delta_s}u^2\delta_s + T_{vert,aft} + T_{vert,\,fwd} + mz_G vr + mz_G wq \tag{67}$$

$$\sum N = N_{wp}wp + (N_{pq} - (I_{yy} - I_{xx}))pq + N_{ur}ur + N_{v|v|}v\,|\,v\,| + \mathrm{N}_{r|r|}\,r\,|\,r\,| + N_{uv}uv + N_{uu\delta_r}u^2\delta_r + T_{lat,\,fwd} + T_{lat,aft} \tag{68}$$

After the linear and angular velocities are determined they are used to determine the linear and angular displacement through the integration of the following equations [8]:

$$\dot{x} = (\cos(\varphi)\cos(\theta))u + (-\sin(\varphi)\cos(\phi) + \cos(\varphi)\sin(\theta)\sin(\phi))v + (\sin(\varphi)\sin(\phi) + \cos(\varphi)\sin(\theta)\cos(\phi))w + u_c \tag{69}$$

$$\dot{y} = (\sin(\varphi)\cos(\theta))u + (\cos(\varphi)\cos(\phi) + \sin(\varphi)\sin(\theta)\sin(\phi))v + (-\cos(\varphi)\sin(\phi) + \sin(\varphi)\sin(\theta)\cos(\phi))w + v_c \tag{70}$$

$$\dot{z} = (-\sin(\theta))u + (\cos(\theta)\sin(\phi))v + (\cos(\theta)\cos(\phi))w + w_c \tag{71}$$

$$\dot{\phi} = p + (\sin(\phi)\tan(\theta))q + (\cos(\phi)\tan(\theta))r \tag{72}$$

$$\dot{\theta} = (\cos(\phi))q + (-\sin(\phi))r \tag{73}$$

$$\dot{\varphi} = (\sin(\phi)/\cos(\theta))q + (\cos(\phi)/\cos(\theta))r \tag{74}$$

where u_c, v_c, and w_c in Equations (69-71) are linear representations of the ocean currents. It should be noted that singularities can occur in Equations 72 and 74 at theta angles of 90 degrees. However, in practice the CAVR REMUS 100 does not typically reach these steep pitch angles and therefore it was not a large concern in this thesis.

F. DEVELOPMENT OF MODEL COEFFICIENTS

1. Previous Coefficient Derivations

After applying the vehicle's specific parameters and symmetry, the hydrodynamic model consists of 44 constants. These constants can be mathematically derived with varying levels of confidence. For the standard REMUS 100 configuration Prestero extensively developed these hydrodynamic coefficients and then verified their accuracy with simulation based and actual vehicle testing. Sgarioto also tested and verified these derived coefficients in a MATLAB based simulation model, after which this thesis is modeled. Similar to Prestero's work, Doherty mathematically and experimentally derived the hydrodynamic coefficients for the CAVR REMUS 100 for a vehicle configuration fairly similar to the configuration used in this thesis. Given that specific hydrodynamic coefficients are affected by vehicle length, vehicle mass, and vehicle velocity, slight changes to vehicle dimensions and characteristics can drastically the performance of the simulation model. Table 7 shows the differences between the REMUS 100 configurations during past and current coefficient development.

Table 7. Vehicle Parameters during Coefficient Development

Configuration	Length (m)	Mass (kg)
Prestero	1.33	30.5
Doherty	2.72	64.5
Current	2.26	52.5

2. Current Coefficient Development

The first step taken in determining the hydrodynamic coefficients for the current CAVR REMUS 100 configuration was to validate that the simulation model worked properly. In order to validate the model Prestero's parameters and coefficients were input into the model and tested. The part of the successful test of the standard REMUS 100 configuration conducting a simulated mission using Prestero's coefficients is shown in Figure 17.

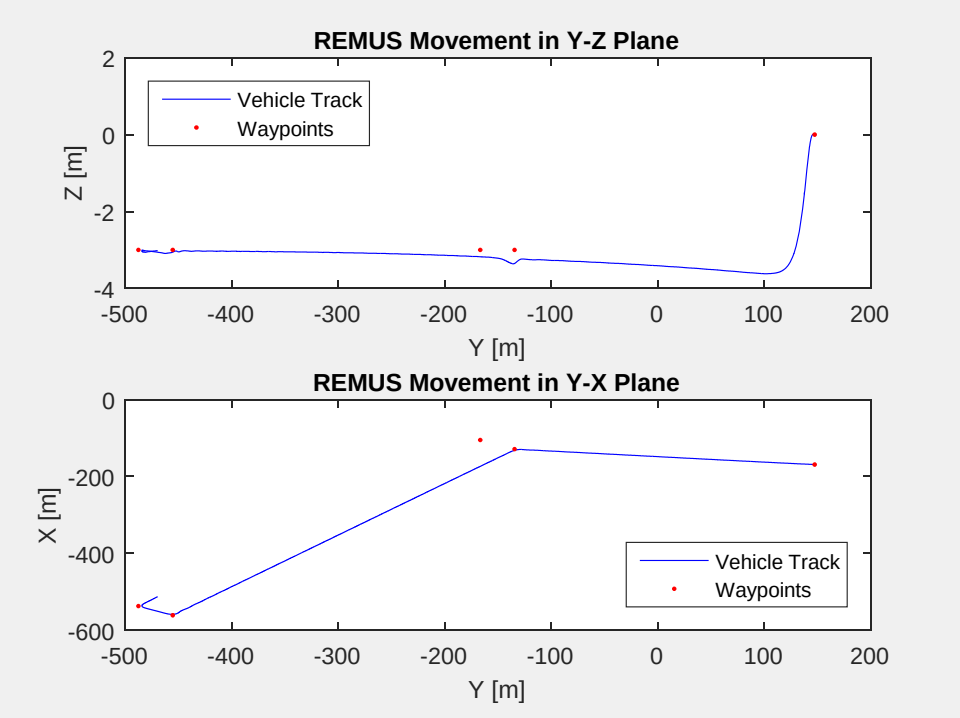

Figure 17. Simulated AUV Mission Using Prestero Parameters and Coefficients

After successfully validating the model with Prestero's coefficients, the vehicle parameters were exchanged with Doherty's and the same simulated mission was conducted. The objective behind this change was to test the robustness of Prestero's coefficients at handling a larger vehicle, and then apply Doherty's coefficients and observe the differences in model performance. Given that the configuration used by Doherty is more similar to the current configuration than Prestero's configuration, Doherty's coefficients were expected to be the baseline for the development of the new hydrodynamic coefficients.

The expectation given the new REMUS configuration was approximately twice the mass and length was that the original model was not going to work and the results, shown in Figure 18, verified this expectation. While the heading control, show in the Y-X plane, was acceptable, the depth control, shown in the Y-Z plane, was not.

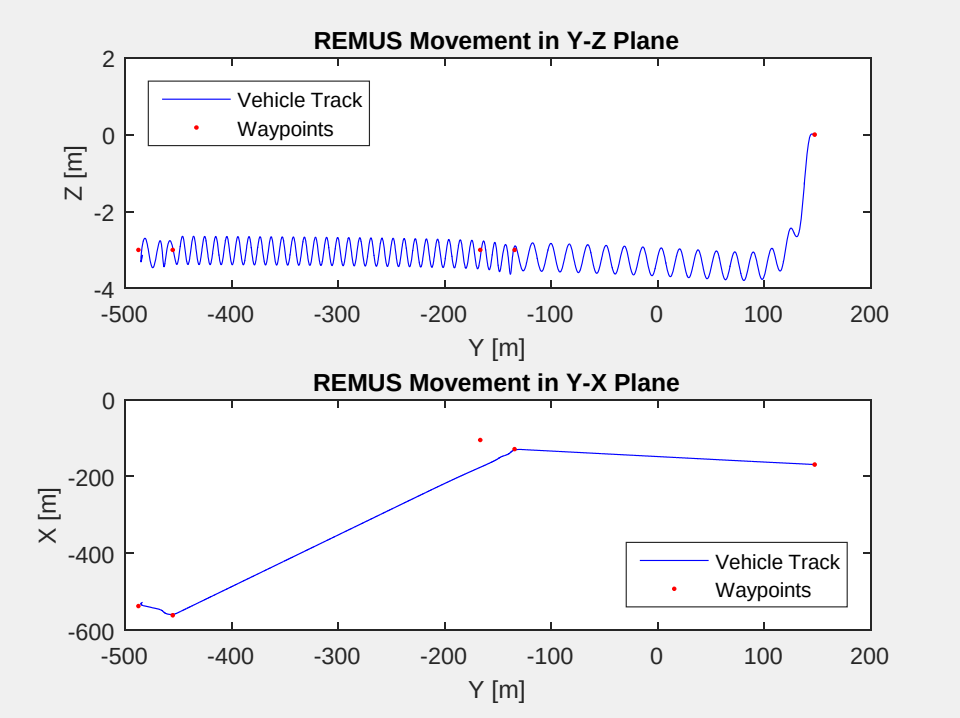

Figure 18. Simulated AUV Mission Using Doherty Parameters and Prestero Coefficients

The next step was to change the coefficients of the original model to those developed by Doherty for the new vehicle configuration. However, after changing all the coefficients and conducting the same simulated mission the model performed unsuccessfully. Figure 19 displays the results of the failed mission.

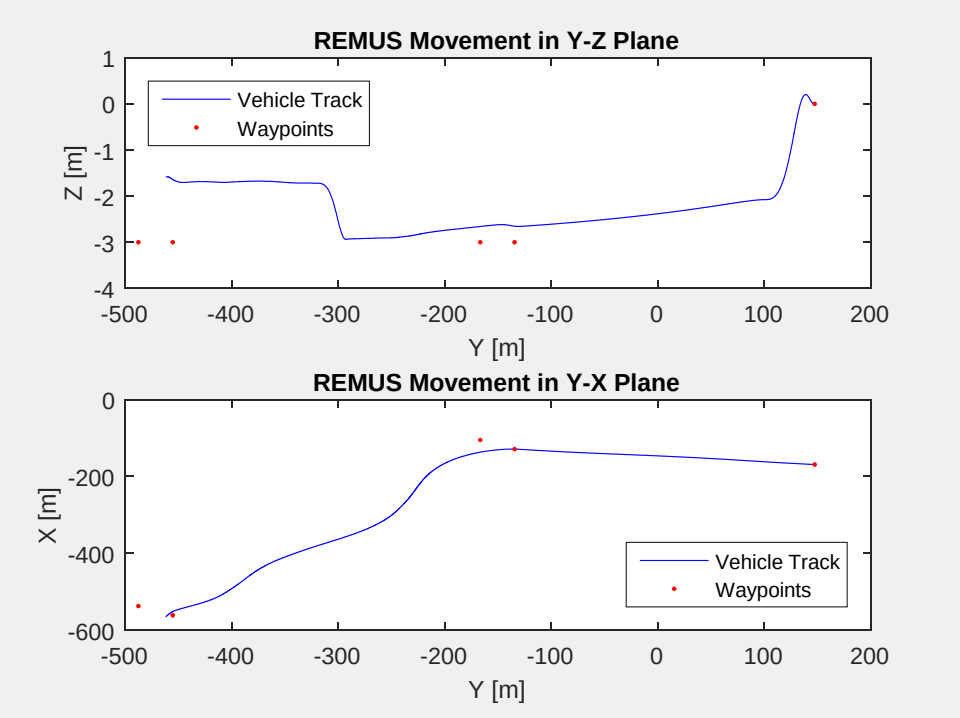

Figure 19. Simulated Mission Using Doherty Parameters and Coefficients

Comparing the two simulated missions using the larger vehicle parameters it is seen that Prestero's coefficients perform better, and therefore were used as the baseline for further testing. As a next step the coefficients were returned to those of Prestero and the vehicle parameters were set to those of the CAVR REMUS 100. To achieve acceptable model performance the next step was to first isolate a specific behavior of the vehicle (i.e., depth control), through its corresponding force and moment (i.e., Z force and M moment), and then isolate the effect of specific coefficients on the vehicle's performance. The coefficients that were changed were also chosen specifically given their contribution to their specific force or moment (i.e., hydrostatic, lift, etc.). The specific forces and moments examined were hydrodynamic damping and added mass, given the assumption that the doubled length and, as a result, the increased surface area would cause the damping and added mass effects to be altered more significantly. It is assumed that several of Doherty's derived coefficients maintain errors and as a way to isolate these errors the chosen coefficients were altered initially by inserting Doherty's coefficient, testing for improved vehicle behavior, and then, if needed, altering it smartly

to achieve improved vehicle performance. It should be noted that these coefficients were determined initially at a constant forward velocity. Test have shown that several of these coefficients are also a function of forward velocity. This function between the coefficients and forward velocity is not yet fully understood with the REMUS 100 and therefore a constant velocity was used initially to achieve an acceptable baseline performance at a typical mission speed.

Acceptable vehicle depth control was achieved after altering the coefficients shown in Table 8.

Table 8. Coefficients Altered for Depth Control Performance

Coefficient	Prestero	Doherty	Current
Z_{uq}	-5.22	0.884	-12.22
M_{uq}	-2	4.16	-10
M_{vp}	-1.93	-4.16	-1
$Z_{\dot{w}}$	-35.5	-77.8	-77.8
$Z_{\dot{q}}$	-1.93	-4.16	-4.16
$M_{\dot{w}}$	-1.93	-4.16	-4.16
$M_{\dot{q}}$	-4.88	-45.2	-30

The same approach was taken with the heading control, Y force and N moment, of the vehicle and acceptable control was achieved after altering the coefficients shown in Table 9.

Table 9. Coefficients Altered for Heading Control Performance

Coefficient	Prestero	Doherty	Current
$Y_{v\,v}$	-1310	-2850	-2850
Y_{ur}	5.22	-0.884	-0.884
Y_{wp}	35.5	77.8	77.8
Y_{pq}	1.93	4.16	4.16
N_{rr}	-94	-2810	-100
$Y_{\dot{v}}$	-35.5	-77.8	-77.8
$Y_{\dot{r}}$	1.93	4.16	4.16
$N_{\dot{v}}$	1.93	4.16	4.16

The coefficients associated with the X force and K moment remained the same from previous work. This is due to the fact that the CAVR REMUS 100 vehicle configuration kept the same diameter with no major changes that impacted roll behavior. However, the propeller component of the X force has shown to differ from previously determined force models. Therefore, the developed u-velocity from the X force must be properly correlated to the aft thruster force and RPM commands. This correlation is developed by utilizing RPM and u-velocity data from real CAVR REMUS 100 missions and the hydrodynamic damping coefficient for the X force component. The mission data used is from a mission developed specifically to test the primary speed controller of the REMUS 100 as well as correlate RPMs to u-velocity. The mission consisted of the REMUS vehicle traveling in a straight line for approximately 1.5 km with the RPMs varying between 0 and 1500, allowing sufficient time for the vehicle to reach the commanded RPM and a steady state u-velocity. The results from this mission and the correlation between RPMs and u-velocity are shown in Figure 20.

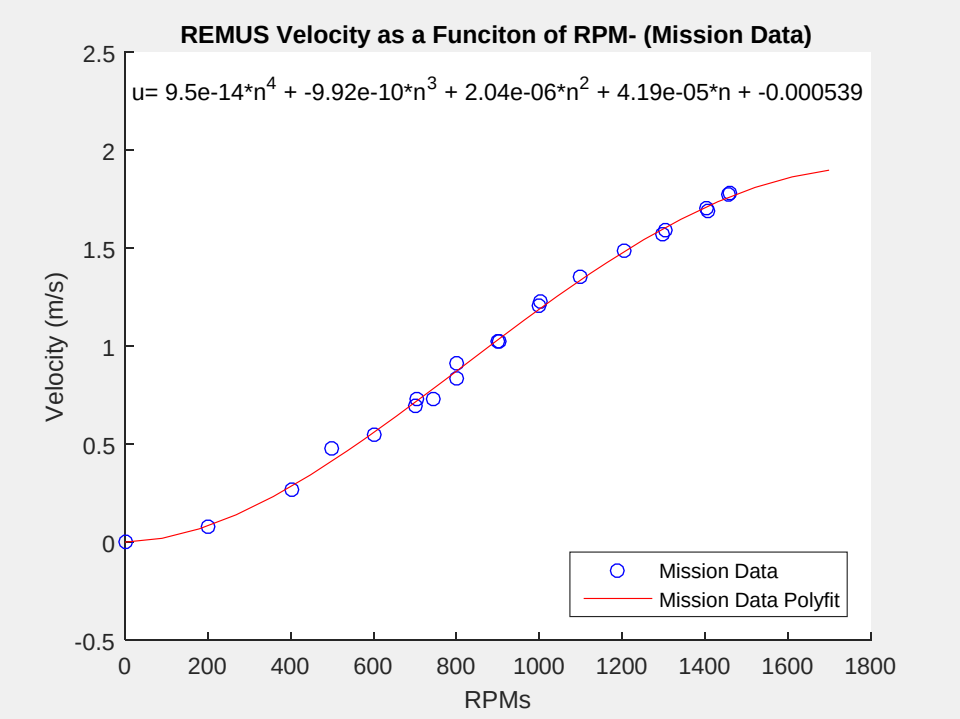

Figure 20. Correlation between REMUS 100 RPMs and Forward Velocity from Mission Data

This developed correlation was then used to determine the hydrodynamic damping coefficients that generate the correct u-velocity from the X force given a specific RPM command. The hydrodynamic damping coefficient that directly affects the forward velocity, u, in the X component of force is $X_{u|u|,}$ which was developed in [7] and [9] by the following equation where ρ is the density of the surrounding fluid, C_d is the vehicle's coefficient of drag in the x-direction, and A is the frontal surface area:

$$X_{u|u|} = -\frac{1}{2}\rho C_d A_f \tag{75}$$

Given that the density of the surrounding fluid and frontal surface area remain constant between vehicle configurations, the coefficient of drag was altered to achieve acceptable performance within the hydrodynamic model. The coefficient testing was conducted by setting the model RPMs to a constant value, allowing sufficient time for the model to reach a stable forward velocity, and then comparing the model velocity to velocity estimate determined from the mission data. If the resulting model velocity was different, the drag coefficient was smartly altered until the error between model and mission data velocities was sufficiently small. The differences between the $X_{u|u|}$ coefficients are displayed in Table 10 and the combined mission and model RPM to velocity correlations are shown in Figure 21.

Table 10. Model Drag Coefficients Required to Achieve Appropriate Forward Velocity

RPM	C_d
0	0
50	750
100	140
200	25
300	8.8
400	4.4
500	2.7
600	1.85
700	1.4
800	1.12
900	0.97
1000	0.85
1100	0.79
1200	0.76
1300	0.755
1400	0.765
1500	0.8

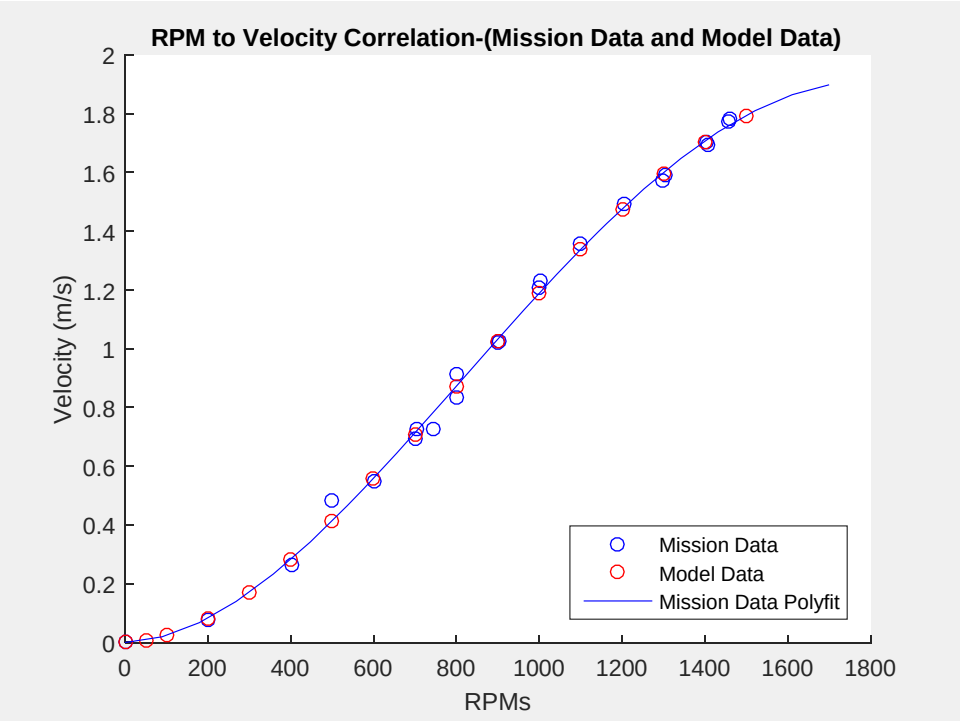

Figure 21. RPM to Forward Velocity Correlation for Mission and Model Data

The rather significant differences between the required drag coefficients at varying velocities was not expected to be as great as the results show, especially for the RPM values below 500. However, upon further expansion of the hydrodynamic damping coefficient, shown in Equation (76), that several assumptions made in previous works are not necessarily true in this thesis.

$$X_{u|u|} = \frac{X}{u^2} = \frac{1}{2}\rho C_d A_f \tag{76}$$

In order to develop the coefficient of drag in this equation, the drag force must be assumed constant, as well as the forward velocity. Both of these assumptions are not true in the case of variable forward velocity. In this scenario velocity is changing as well the drag force. While the exact Reynolds numbers are not known for all the varying forward velocities performed in this test, [7] and [9] both estimate, given their calculated Reynolds number, that at full speed the REMUS 100 vehicle operates in the laminar-turbulent transition zone. Both [7] and [9] further believe that given the many protrusions and pockets on the surface of the vehicle, the flow is most likely tripped into primarily turbulent flow. Therefore, during the range of test RPMs the REMUS 100 operates in both laminar and turbulent flow conditions which result in different drag forces. These differing drag forces combined with the varying forward velocities could account for the changes experienced with the developed drag forces. However, to fully understand and justify these developed drag coefficients further testing of developed drag forces and boundary conditions for the REMUS 100 are necessary.

The full table of hydrodynamic coefficients used in this thesis are shown in Appendix B.

G. MODEL CONTROLLERS AND AUTOPILOTS

The hydrodynamic simulation model consists of a depth controller, heading controllers, aft thruster controller, and tunnel thruster controllers. The depth controller used is developed from diving autopilot in Sgarioto's hydrodynamic model for the REMUS vehicle [8]:

$$\delta_{s_{com}} = G_1(Z_d - Z) + G_2\theta + G_3 q + G_4 \int (Z_d - Z)\partial t \tag{77}$$

where G_1,G_2, G_3, and G_4 are the controller gains and Z_d is the commanded depth. The controller seeks to reduce the error between commanded depth and actual depth by developing stern fin commands that causes the vehicle to either dive or rise.

The two heading controllers are also developed from Sgarioto's model but are originally derived from Marco and Healey's [27] work with the NPS ARIES vehicle and consist of a large heading error and small heading error controller. The development of these controllers can be found in [8] or [27];

The last group of controllers used are the RPM controllers for the 5 propellers on the CAVR REMUS 100. The controller is a conventional proportional-integral controller with the error signal based on the RPMs of the propeller:

$$N_{d_{COM}} = F_1(n - n_d) + F_2 \int (n - n_d)\partial t\,, \tag{78}$$

where F_1 and F_2 are the controller gains and n_d is the RPM command.

This PI controller show in Equation (78) was instituted for all five propellers and the gains were adjusted to resemble realistic propeller RPM behavior by comparing the model behavior to real mission data. Additionally, to prevent windup with the integral portion of the controller the integral was reset to zero when the RPMs were saturated.

THIS PAGE INTENTIONALLY LEFT BLANK

IV. POSITION ESTIMATION FILTER

A. KALMAN FILTER

The Kalman Filter (KF) is the current standard for position estimation filtering and data fusion. The filter combines Bayesian logic and state space representation to predict an updated state vector and updated covariance matrix based on an a priori assumption and a current measurement. The KF is a recursive procedure which means the updated values are fed back into the filter as the a priori assumption and the process begins anew. This filter also propagates the uncertainty or error within the updated state and measurement with the addition of noise variables. These noise variables assume that the error mean and covariance maintain a normal Gaussian probability distribution about zero. The great utility of this filter is the simplicity of the calculations. The filter is composed of five primary equations, the first of which is the state estimate extrapolation:

$$x_{k+1|k} = Ax_{k|k} + Bu_k , \tag{79}$$

where A is the state transition matrix, $x_{k|k}$ is the a priori state space system estimate, B is the control input transition matrix, u_k the control input, and $x_{k+1|k}$ is the extrapolated system estimate. The second equation is the covariance extrapolation

$$P_{k+1|k} = AP_k A^T + Q_k , \tag{80}$$

where P_k is the a priori covariance estimate, Q_k is the Gaussian system or process error noise, and $P_{k+1|k}$ is the extrapolated covariance. The third equation is the calculation of the Kalman gains:

$$K_k = P_{k+1|k} H^T [H_k P_{k+1|k} H^T + R_k]^{-1}, \tag{81}$$

where H is the measurement transition matrix, R_k is the Gaussian measurement error noise, and K_k are the Kalman gains. The fourth equation is the state update:

$$x_{k+1|k+1} = x_{k+1|k} + K_k [z_k - H_k x_{k+1|k}] , \tag{82}$$

where z_k is the measurement and $x_{k+1|k+1}$ is the updated state estimate. The fifth equation is the covariance update:

$$P_{k+1|k+1} = [I - K_k H_k] P_{k+1|k}\,, \tag{83}$$

where I is an identity matrix and $P_{k+1|k+1}$ is the updated covariance estimate. The KF while very useful for its simplicity, does have its shortcomings. The most significant short coming is that the system model being extrapolated and updated is assumed to be linear. While a Gaussian probability distribution is a fairly good estimate for linear system models it is not always necessarily applicable for non-linear models. To better represent and model the position estimation problem with the CAVR REMUS 100 other versions of the Kalman filter were explored, specifically the Extended Kalman Filter (EKF) and the Unscented Kalman Filter (UKF).

B. EXTENDED KALMAN FILTER

While the KF remains the general standard filtering method for position estimation and data fusion for linear systems, the EKF is the standard for non-linear systems. The EKF mitigates the non-linearity of systems by linearizing the system through the use of a Jacobian matrix of partial derivatives. This linearization is accomplished by using the first two terms of the Taylor Series expansion which equates to a first order approximation of the non-linear system. The assumption with the EKF is that the statistical properties of the linearized systems is nearly equal to those of the non-linear system. Similar to the KF, the EKF assumes that the mean and covariance of the process and measurement noise follows a Gaussian distribution about zero. While the accuracy of the EKF for non-linear systems remains fairly high given small time steps, it can rapidly degrade if the system is highly non-linear. The errors accrued by this high non-linearity can then be amplified during the calculation of the Jacobian matrix. Additionally, obtaining the Jacobian matrix can be a difficult and sometimes not feasible process. However, if the system does not fall within these limitations, the EKF remains an acceptable method for a wide range of applications. The governing equations of the EKF are very similar to the KF with the new state extrapolation or predication being:

$$x_{k+1|k} = f(x_{k|k}, u_k) \tag{84}$$

where is the non-linear, differentiable system is represented by the function *f*. The covariance prediction equation is now:

$$P_{k+1|k} = F_k P_{k|k} F_k^{\ T} + Q_k \,, \tag{85}$$

where F is the state transition matrix and is derived from taking the Jacobian of the function *f*:

$$F_k = \left. \frac{\delta f}{\delta x} \right|_{(x_{k|k}, u_k)} \tag{86}$$

The Kalman gain equation is the same as the one presented in Equation (81), however the measurement or observation transition matrix is derived by obtaining the Jacobian of the non-linear, differentiable measurement model represented in Equation (88) by *h*:

$$H_k = \left. \frac{\delta h}{\delta x} \right|_{(x_{k+1|k})} \tag{87}$$

The new state update equation is:

$$x_{k+1|k+1} = x_{k+1|k} + K[z_k - h(x_{k+1|k})], \tag{88}$$

where, as previously stated, *h* is the non-linear, differentiable measurement model. The covariance update equation, similar to the Kalman gain equation, is the same as the Equation (83). It should be noted that in this thesis the term Φ was utilized in the place of F_k. This is a common and convenient method of substituting the Jacobian calculation associated with the derivation of F_k with the solution of the first order differential equation $\dot{x}$ =Ax. The combination of the solution to this first order differential equation and substitution is :

$$F_k = \Phi_k = e^{A\Delta t}, \tag{89}$$

where t is the time step of the EKF calculation process.

The EKF provides a fairly good solution to mitigating the limitations associated with the KF, but still possesses several shortcomings with respect to the REMUS 100 position estimation problem. The USBL system utilized by the REMUS 100 calculates its position using non-linear functions from range and bearing measurements. These range and bearing measurements are also believed to stray from the Gaussian mean and

covariance assumption as the performance of the USBL is affected by a variety of environmental conditions as well as the range from the acoustic transponder. As previously discussed the EKF begins to degrade for highly non-linear systems and assumes a Gaussian error distribution. Given these properties of the EKF and the characteristics of the USBL system, the EKF is believed to not be an acceptable filtering solution for position estimation. As a result of the EKF shortcomings the UKF is examined.

C. UNSCENTED KALMAN FILTER

In order to mitigate the limitations previously discussed with the EKF, the UKF was examined. A significant difference the UKF provides is that it omits the linearization of the process and measurement equations, and instead utilizes the true non-linear equations of the system. This difference greatly reduces the complexity and difficulties that arise in the calculation of the Jacobian matrix. The state mean and covariance are also no longer assumed Gaussian. The distribution is maintained by using a set of specifically designed sample points, called sigma points, around the estimate in an unscented transform (UT) [19]. This method was created on the basis that it is simpler to transform a single point rather than an entire probability distribution and that the probability distribution can then be reconstructed after the UT [28]. The sigma points and UT are critical to the UKF as they allow for the approximation of a probability distribution that has not been skewed by non-linear functions [29]. These sigma points and associated weighting values are chosen carefully to best represent the true mean and covariance of the system. The use of these sigma points also allows for the spanning of potential discontinuities in the non-linear system. In addition to the elimination of the Jacobian function and ability to handle discontinuities, the UKF provides higher order approximation at a computational cost within one order of magnitude of the EKF or KF [28]. The updated mean and covariance are reportedly represented in statistical moments up to the third order Taylor Series approximation [28].

The advantages of the UKF over the EKF make it a very attractive filter for handling the non-linearities associated with the of the USBL system. While there are

some similarities between the governing equations of the UKF and EKF or KF, the majority of the governing equations are fairly unique to the UKF. The first set of calculations in the UKF process determining the weights for the sigma points as well as the mean and covariance of the sigma points:

$$\lambda = \alpha^2 (L + \kappa) - L \tag{90}$$

$$W^{mean} = \left[\frac{\lambda}{L+\lambda} \quad \left(\frac{1}{2(L+\lambda)} \right)_i \right] \qquad i = 1,...,2\,\mathrm{L} \tag{91}$$

$$W^{\mathrm{cov}} = \left[\left(\frac{\lambda}{L+\lambda} + (1 - \alpha^2 + \beta) \right) \quad \left(\frac{1}{2(L+\lambda)} \right)_i \right] \qquad i = 1,...,2\,\mathrm{L} \tag{92}$$

where λ is a scaling parameter, α determines the spread of sigma points around the a priori estimate, typically a small positive value, κ is a secondary scaling parameter, typically zero, β incorporates prior knowledge of the distribution, and L the length of the state vector [19]. Next the sigma points are calculated using the a priori state and covariance estimate:

$$\chi_k = \left[x_k \quad x_k \pm \sqrt{(L+\lambda) P_k} \right] \tag{93}$$

Following the generation of the sigma points, an unscented transformation of the process equation occurs where the sigma points are propagated forward one time step. From this propagated time step the mean and covariance values for the state estimate are developed by weighting each sigma point by its predetermined weighting value.

$$\chi_{i,k+1|k} = F\left(\chi_{i,k}\right) \tag{94}:$$

$$x_{k+1}^{-} = \sum_{i=0}^{2L} W_i^{mean} \chi_{i,k+1|k} \tag{95}$$

$$P_{k+1}^{-} = \left(\chi_{i,\mathrm{k}+1|\mathrm{k}} - x_{k+1}^{-}\right) diag\left(W^{\mathrm{cov}}\right) \left(\chi_{i,\mathrm{k}+1|\mathrm{k}} - x_{k+1}^{-}\right)^T + Q \tag{96}$$

Following the UT of the process equations, another unscented transformation occurs with the measurement equations. Similarly, the mean and covariance values for

the measurement are developed by weighting each sigma point by its predetermined weighting value.

$$Y_{i,k+1|k} = H\left(\chi_{i,k}\right) \tag{97}$$

$$y_{k+1}^{-} = \sum_{i=0}^{2L} W_i^{mean} Y_{i,k+1|k} \tag{98}$$

$$P_{y_k,y_k} = \left(Y_{i,k+1|k} - y_{k+1}^{-}\right) diag\left(W^{\text{cov}}\right)\left(Y_{i,k+1|k} - y_{k+1}^{-}\right)^T \tag{99}$$

Following the UT of the measurement and process equations, the covariance between the predicted state estimate and the predicted measurement is determined, the Kalman gains are calculated, and the updated state and covariance estimates are developed.

$$P_{x_k,y_k} = \left(\chi_{i,k+1|k} - x_{k+1}^{-}\right) diag\left(W^{\text{cov}}\right)\left(Y_{i,k+1|k} - y_{k+1}^{-}\right)^T \tag{100}$$

$$K = P_{x_k,y_k} P_{y_k,y_k}^{-1} \tag{101}$$

$$x_{k+1|k+1} = x_{k+1}^{-} + K\left(z_k - y_{k+1}^{-}\right) \tag{102}$$

$$P_{k+1|k+1} = P_{k+1}^{-} - K P_{x_k,y_k}^T \tag{103}$$

D. FILTER SYSTEM CONFIGURATION

After researching the advantages and disadvantages of the EKF or UKF, both the EKF and UKF were chosen to be tested and implemented with the INS system, but only the UKF was chosen to be implemented with the USBL system. The specific configuration of the filters was based off a federated form of unscented Kalman filtering presented by [17]. This form of filtering decentralizes UKFs to filter specific sensor systems and are then combined using a predetermined weighting value, represented by the variable β, and are fed into a master UKF that generates a combined, updated state estimate and covariance. This state estimate and covariance are then broken down by the

inverse of the weighting value and fed back into the local filters. This federated form is displayed visually in Figure 22.

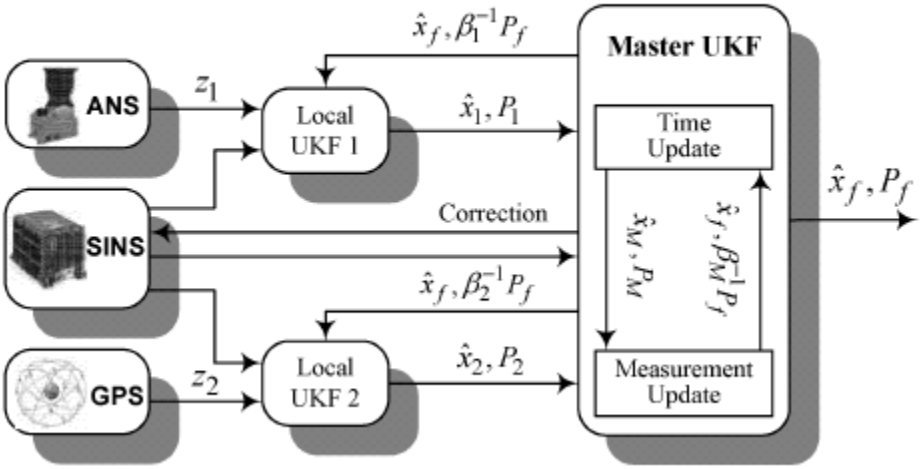

Figure 22. Federated Form of Unscented Kalman Filtering. Source: [17].

The specific configuration form used in this thesis only takes parts of this federated design. It utilizes the decentralized or local filter design, but does not utilize a master UKF to combine the values. Instead, the updated state estimates of the local filters are simply weighted together using a specific weighting function. The combined values were also not necessarily fed back into the local filters. Several configurations were tested to decide if feedback to the local filters would provide the desired positional accuracy. It was determined that for the USBL filter that the combined position estimate would not be used as the a priori estimate to allow for a true comparison of several USBL measurements. After observing USBL performance in previous docking missions it was seen that good, consistent USBL measurements tend to mimic the track of the current position estimate of the vehicle. Figure 23 depicts an actual mission that displays what is meant by USBL data mimicking the track of the vehicle.

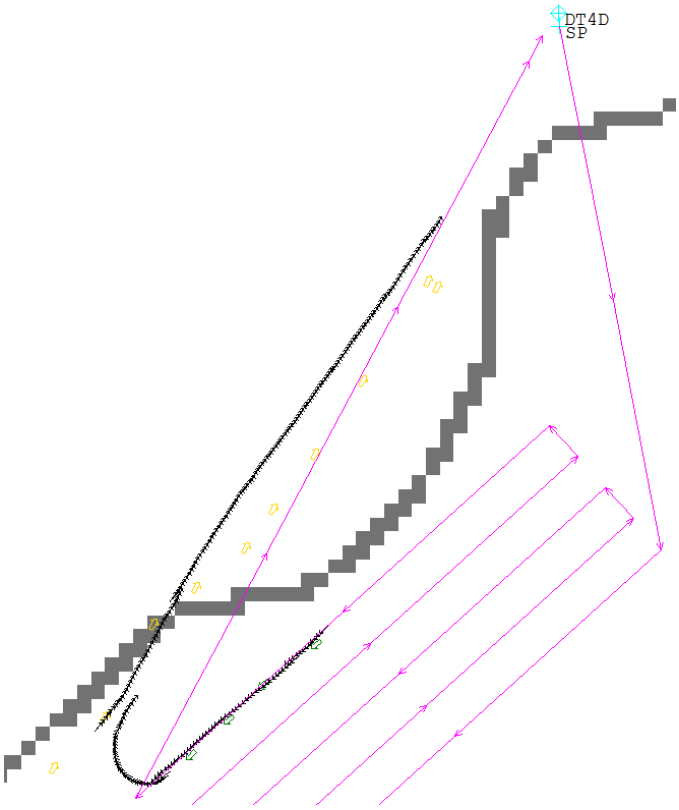

Figure 23. Terminal Homing Mission with Consistent USBL Data

In Figure 23, the yellow arrows represent USBL measurements and the black dots represent the current estimate of the vehicle, the gray colored line represents the bathymetry contour line and the magenta lines represent the mission plan. The vehicle is traveling from the bottom left of the figure to the top right, and as the vehicle gets closer to the acoustic transponder, labeled DT4D in the figure, the measurements gain consistency and begin to mimic the track of the vehicle, simply translated 8–12 meters to the right. As a potential method of determining how heavy to weight the USBL measurement this consistency was sought to be quantified and therefore updating the a priori assumption with the combined measurement would taint the true state estimate of the USBL filter. However, given the growing error with the INS, feeding back the combined estimate was tested as a way of reducing the growing positional uncertainty.

The approach in this thesis utilizes three filters, one for the USBL, one for the INS, and the REMUS filter. The REMUS filter takes all available measurements from

various sensor systems to provide a best position estimate. This filter is developed by the vehicle manufacturer. The process by which this filter operates is proprietary and therefore not fully known, however, understanding this filtering process is not critical to this thesis, but rather the information that it outputs. The State information utilizes all available sensor information to generate an accurate position estimate, which for this thesis consists of the INS and ADCP/DVL. While this filtering method has been found insufficient at generating enough positional accuracy to effectively dock in an accurate and timely manner, it does provide a useful baseline position estimate to combine with the USBL data. However, this state measurement for the initial testing in MATLAB, which utilized previous REMUS 100 docking mission data, was not used because it also consisted of the USBL sensor data. Therefore, the baseline position estimate to combine with the USBL data was the true INS and ADCP/DVL measurements.

The state vector used in the filtering process consisted of the x, y, and z positions, the u, v, and w linear velocities, the heading, and the heading rate

$$x = \begin{bmatrix} x & y & z & u & v & w & \varphi & r \end{bmatrix}^T \tag{104}$$

As a result of the USBL sensor lacking the ability to generate a z, u, v, w, heading, and heading rate, they were extracted from the INS and ADCP/DVL. The heading and heading rate were extracted from the INS, the depth was extracted from the ADCP/DVL, and linear velocities were extracted from both the DVL and INS. In order to maintain as much independence from the two filters, the DVL velocities were used initially, however as the results will later show, the estimates of these velocities was poor and therefore the INS velocities were used instead.

The general configuration of the filtering system is visually shown in Figure 24. This figure also shows several variations of the general filter configuration that were tested. These variations included testing both an EKF and UKF for the INS system, testing both the INS and ADCP data, and testing whether to update the INS filter with the combination state estimate. The differences between the configurations used in the MATLAB based testing and the intended vehicle testing are also represented in Figure 25 by the “circuit like” breaking of the line segments.

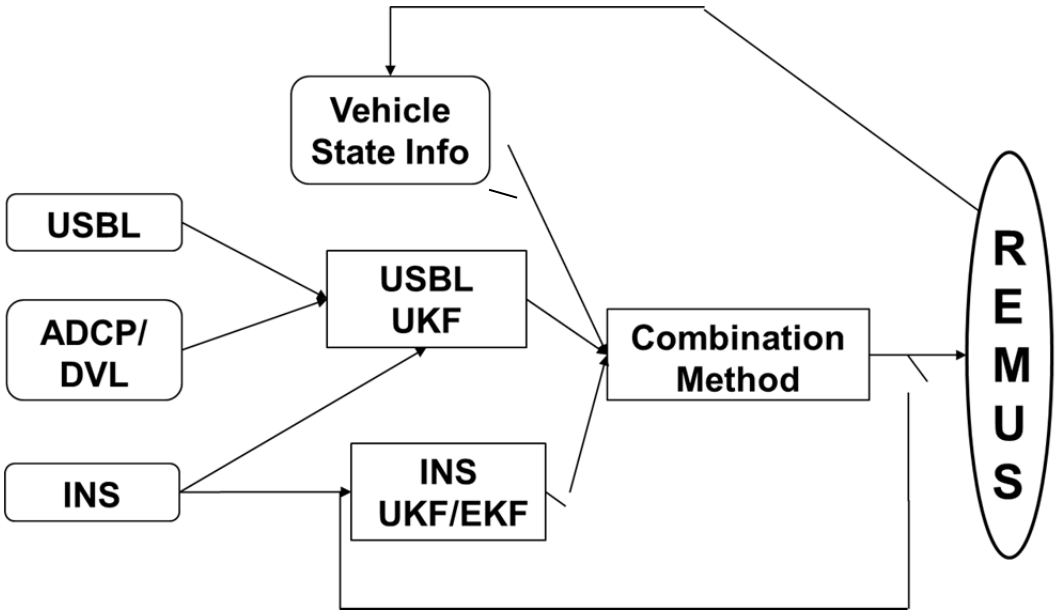

Figure 24. Final Filter Configuration Design

E. TESTING DATA AND METHOD

The underlying goal of this filtering system was to deal with the asynchronous, erroneous, and sporadic behavior of the REMUS 100 sensor systems, specifically the INS and USBL. The INS system generates measurements at approximately 10 Hz; however, the vehicle settings for the INS for the majority of the MATLAB based testing was set to collect at 1 Hz. The USBL system, on the other hand, varied in its data generation rate from as low as .0625 Hz up to about 1 Hz. On top of the variable measurement generation rate, not all the generated measurements were valid. The USBL performs a self-test to determine whether it deems the measurement accurate, and if it is deemed not accurate the USBL generates zeros for the x and y position measurements. Similar to the state information filter the exact self-test criteria are not fully known. However, given the lack of ability to access to the undisturbed USBL measurements the post self-tested measurements must be used, and therefore understanding the self-test criteria is superfluous.

In order to test the feasibility of the filter design at achieving the underlying position estimation goals of thesis, the filter was tested in several steps. The first steps

consisted of testing the filter with ideal, user generated data. This data was generated by simulating a vehicle mission using the following state vector.

$$x = [x \quad y \quad u \quad v \quad \varphi \quad r]^T \tag{105}$$

This simulated mission was then assigned as the "ground truth" or true position of the vehicle, which for actual REMUS 100 missions is not known. This ground truth position was then slightly perturbed and assigned as the INS measurement. This perturbation was a simple attempt at representing the noise or error in a typical INS measurement. The ground truth position was then used to generate USBL measurements. Similar to the INS measurement, the USBL measurements were perturbed to represent the error experienced with the real sensor system. However, unlike the INS measurements, the level of perturbation of the USBL measurements was altered as a function of range to the "docking station" to more accurately represent the behavior of the true sensor system.

For the initial runs of the filtering process the data for the INS and USBL measurements were generated at the same frequency of 1 Hz to test the ability of the system to successfully combine the two measurements, and the combination method used was a simple averaging of the two measurements. Once the filter successfully combined the two sensor measurements the data generation rate of the USBL filter was changed from 1 Hz to .1 Hz to test the ability of the filter handling asynchronous measurements at a USBL rate that is on the slower end of the rates experienced during actual REMUS missions. During this test the combination method remained a simple average of the two measurements. After successfully dealing with the asynchronous behavior, the USBL data was then further altered to include random zero measurements to test the ability of the filter from not diverging when it lacked appropriate measurement information. Additionally, a constant u and v current was added to the ground truth measurement but only applied to the USBL measurement. These currents were a simple method of inputting a constant error into the INS measurement in order to test other combination methods with measurements more realistic to real docking missions. The next combination method tested was a weighting function that weighed the USBL

measurements greater as the range to the docking station decreased. This method was chosen as a large portion of the USBL measurement error is a function of the range to the docking station. After this combination method was instituted and the new data was tested and resulted in adequate performance, the testing of the filter shifted to real REMUS 100 mission data.

In order to test with real mission data, previous mission files that either consisted of terminal homing for docking runs or terminal homing on acoustic transponders were chosen. The USBL, INS, State, and ADCP measurements were then extracted from the missions and converted into a state vector shown in Equation (104). As previously discussed, in order to develop the full state vector for the USBL measurements, the depth, linear velocities, heading, and heading rate were obtained by either the INS or ADCP/ DVL.

Initial difficulties were experienced with the real mission data as the sensors did not operate at typical operating frequency and did not necessarily operate at a truly constant operating frequency. For example, the INS system delivered measurements every 1.097–1.098 seconds and the USBL system delivered measurements every 1.098–15 seconds. In order to deal with this issue, the measurements in the state vector were extracted from the mission data along with the respective time each measurement was generated. After each measurement maintained a timestamp, several methods were developed and tested in an attempt to deal with this sensor behavior. The first method consisted of operating both the USBL and INS filters at 1 Hz and testing to see if a measurement occurred between time steps and if not instead using the most recent measurement as the new measurement, excluding the position, in an attempt to propagate the position of the vehicle forward. The second method tested was to maintain the same INS method as previously stated, but only run the USBL filter if a measurement occurred. This method also consisted of continually averaging the most recent a priori estimate of the USBL filter with the estimate of the INS filter in order to accurately maintain the behavior of the vehicle between time steps. The third method tested was a essentially a retesting of the first two methods, but this time the INS position update was zeroed out in an attempt to simulate the lack of a GPS measurement and a compounding or growing

error. The fourth method was again a retesting of the first two methods, but the USBL linear velocity measurement were changed from those generated by the INS to those generated by the ADCP/DVL sensor system.

The results of both the user generated data and the real mission data are further shown and discussed in the next chapter of this thesis.

THIS PAGE INTENTIONALLY LEFT BLANK

V. RESULTS AND ANALYSIS

A. HYDRODYNAMIC MODEL RESULTS

As previously discussed the implementation of the new CAVR REMUS 100 vehicle parameters were successfully developed and tested at a constant forward velocity. The specific velocity that these parameters were designed around was the max operating speed of the vehicle, 1500 RPMs, which equates to approximately 1.8 m/s or approximately 3.5 knots. In this thesis, acceptable vehicle behavior was defined as achieving the commanded speed, reaching the desired waypoints, maintaining stable control about the intended mission track line, and maintaining stable control of the roll, pitch and yaw otherwise referred to in this thesis as φ, θ, and ψ. Figure 25 and 26 shows the acceptable results of a simulated mission using the hydrodynamic model. Additionally, Figure 27 shows the resulting forward velocity, roll, pitch, and yaw control throughout the duration of the mission.

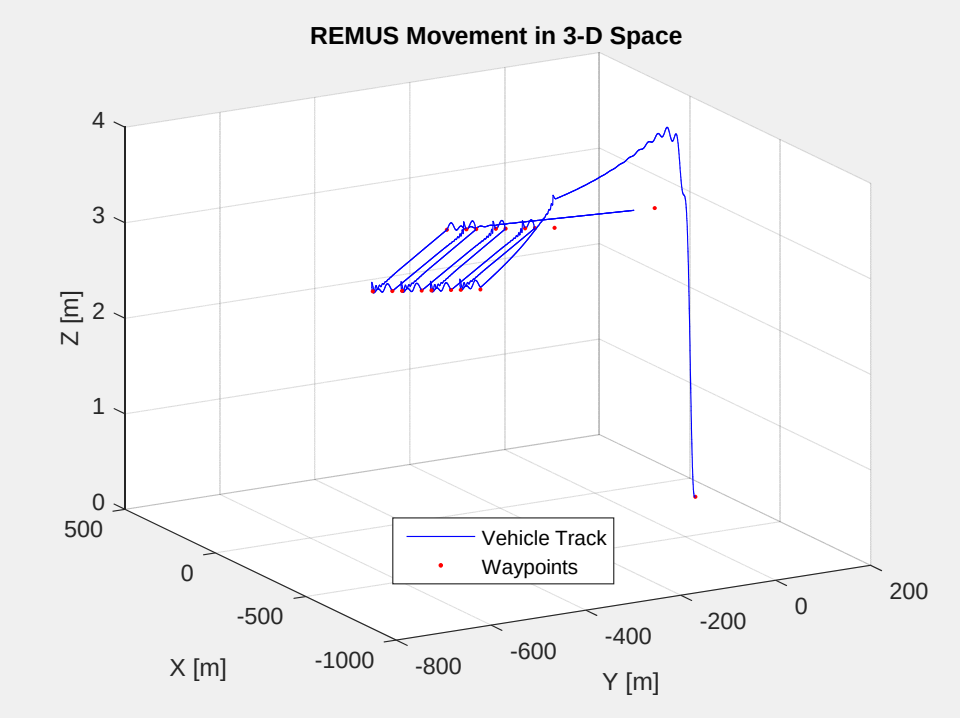

Figure 25. Successful Simulated Mission Using Hydrodynamic Model (3D space)

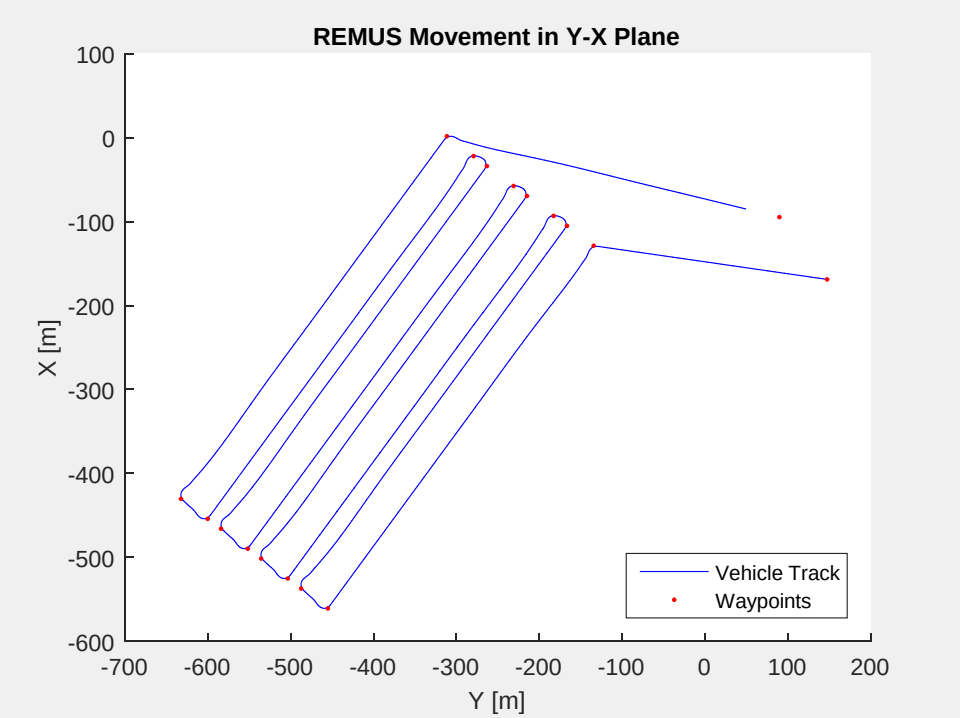

Figure 26. Successful Simulated Mission Using Hydrodynamic Mode (Y-X Plane)

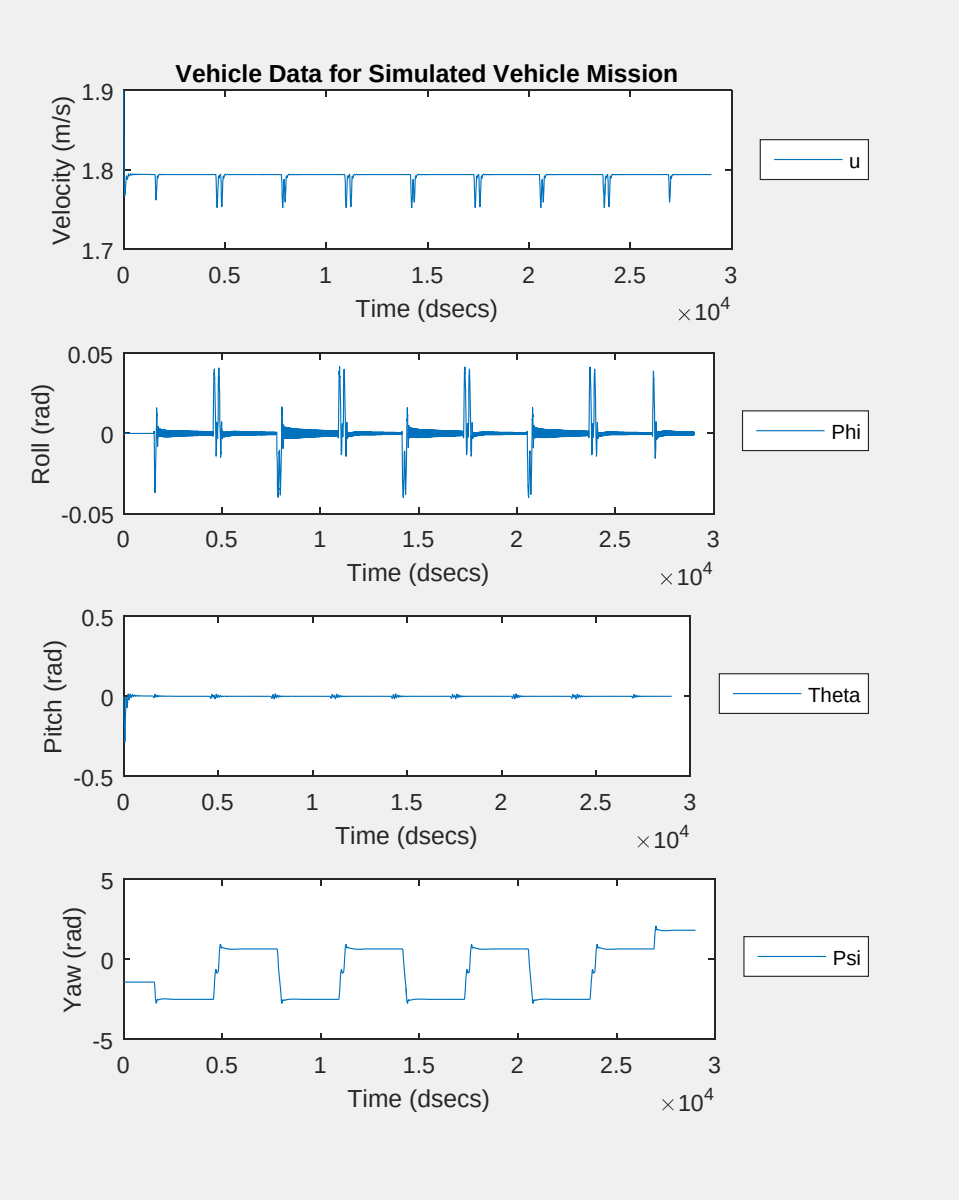

Figure 27. Mission Data from Simulated Mission Using Hydrodynamic Model

As another means of determining whether the hydrodynamic model performed adequately, it was compared to a similar surveying mission conducted with the actual REMUS 100 in the same configuration. Comparing the performance of the simulated mission using the hydrodynamic model to the performance of an actual REMUS mission, shown in Figure 28 and 29, it is seen that the model actually performed better than the actual vehicle. This better performance of the model is most likely a result of the

simulated vehicle operating in an ideal, benign environment with very optimal vehicle control. The vehicle mission shown took place in Monterey Bay and could very easily have been affected by currents and wave effects.

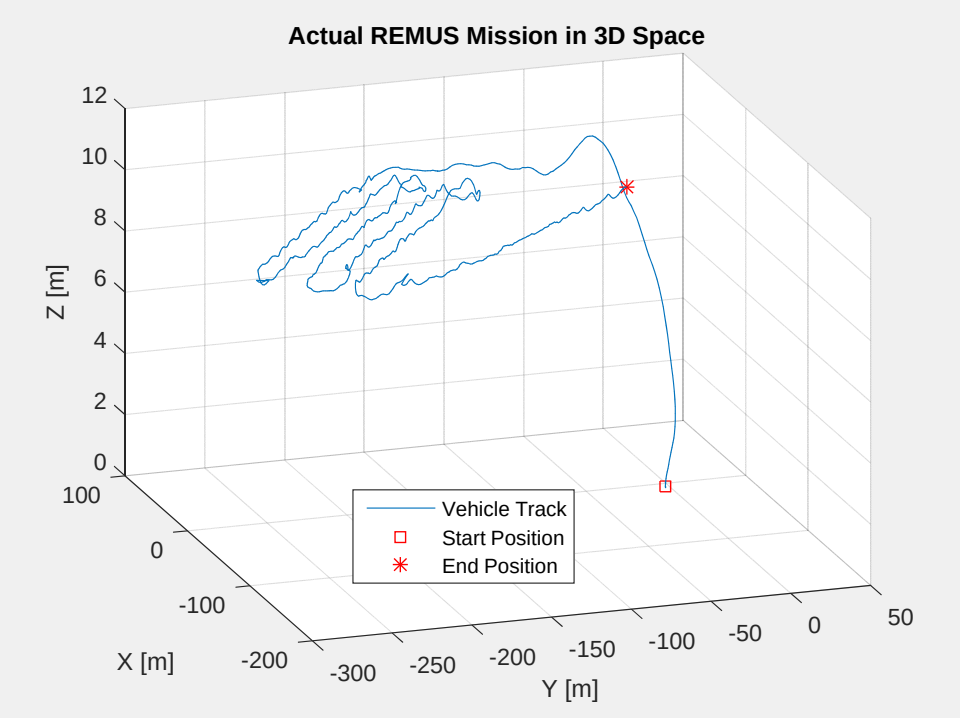

Figure 28. Surveying Mission of CAVR REMUS 100 (3D Space)

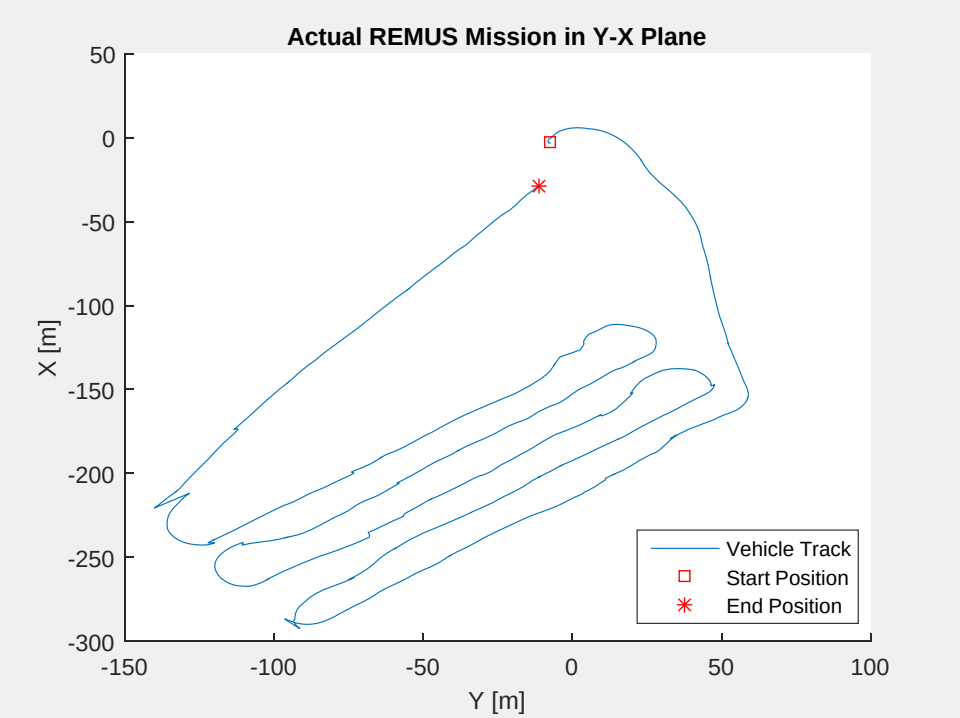

Figure 29. Surveying Mission of CAVR REMUS 100 (Y-X Plane)

While this result helps to reaffirm that the model performance is acceptable, it may actually be "too good." However, before the model was degraded to more accurately reflect the true performance of the REMUS vehicle, it was decided that the additional goals of variable speed control and tunnel thruster implementation and control would attempted to be achieved first.

Another goal of this thesis was to implement variable speed control within the model to simulate the REMUS 100 conducting a typical mission where after it conducted the programed mission objectives it would then approach the docking station, slow down, and then utilize the cross tunnel thrusters to successfully dock. To test the capability of the developed hydrodynamic model at handling varying speeds the constant velocity aspect of the model was altered to initially begin at a near zero velocity and then increase to the max forward velocity. These new variable speed commands were instituted for the initial portion of the same mission as shown in Figure 26 and the results are shown in Figure 30 with forward velocity, roll, pitch, and yaw shown in Figure 31.

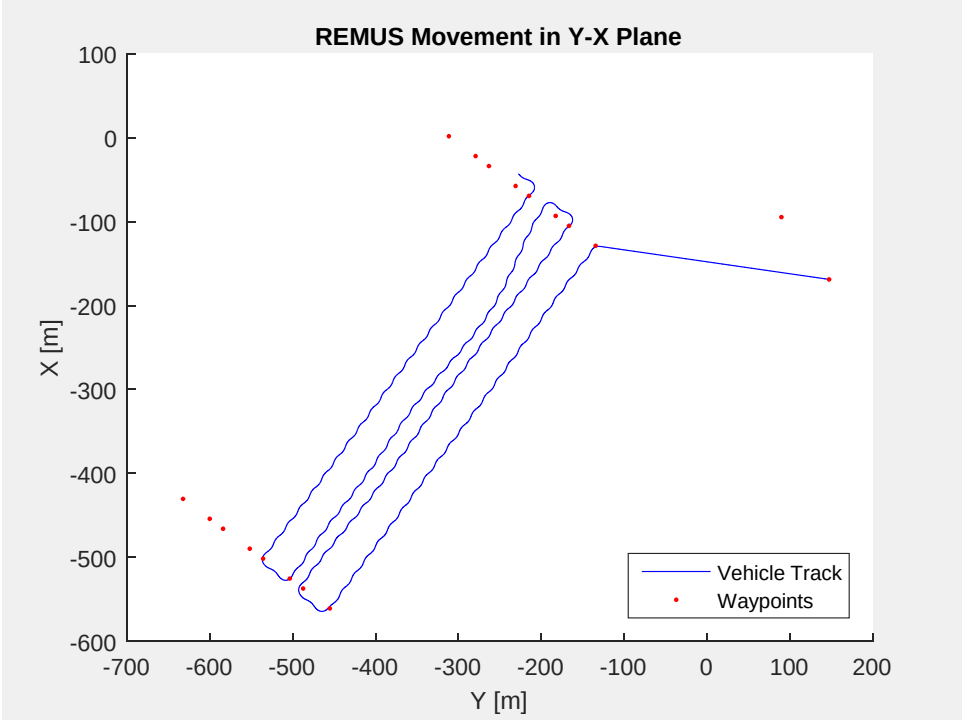

Figure 30. Simulated Mission Utilizing Variable, Increasing Forward Velocity

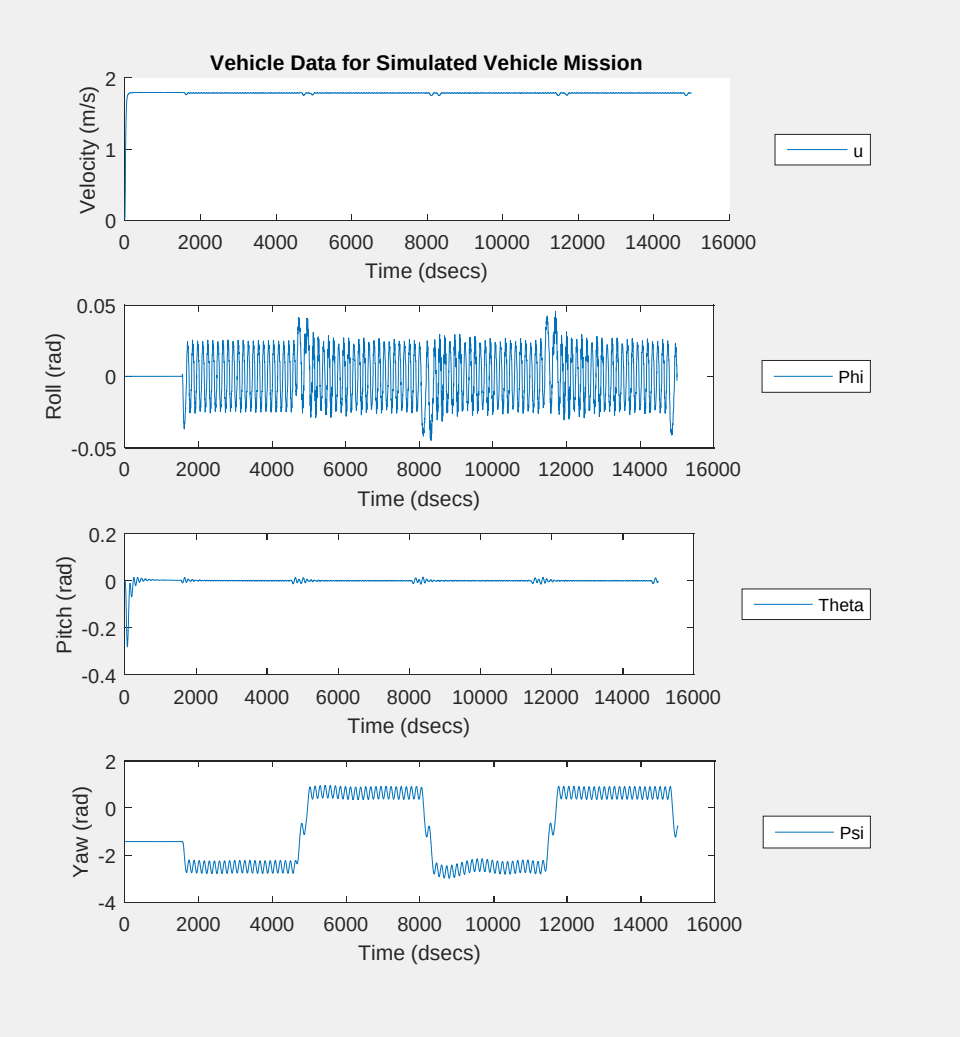

Figure 31. Vehicle Data from Simulated Mission Utilizing Variable Forward Velocity

As seen in Figure 30 and 31, the resulting performance of the variable speeds with the newly developed hydrodynamic model was rather poor. While the model successfully went from near zero velocity to the desired velocity in a realistic amount of time, large significant oscillations developed in roll and yaw. It was initially believed that the hydrodynamic coefficients change as a function of forward velocity, and as an initial attempt to quantify the extent of these changes the coefficients were altered to achieve acceptable behavior while the velocity ranged from near zero to the max velocity. If acceptable behavior was able to be achieved over the full range of forward vehicle velocity by altering the hydrodynamic coefficients, it would greatly reduce the required

testing and development time associated with testing the hydrodynamic coefficients are small velocity increments. In an attempt to reduce these oscillations, a similar process to that originally conducted to develop the hydrodynamic model was applied. However, after altering the same coefficients as before, as well as additional coefficients, acceptable behavior was not able to be achieved. It is believed that the range of velocities tested during this mission was too great and that the development of average hydrodynamic coefficients for this span was not an accurate enough way of representing the effect of forward velocity on the hydrodynamic coefficients.

However, before the hydrodynamic coefficients were determined for other velocities the variable speeds were tested once more, but this time in reverse. This test was conducted to examine if the same vehicle behavior develops as the vehicle slows down. The initial speed for this test was set to max and the final speed was set to 700 RPMs, which was chosen to represent the slower approach speed to the docking station as well as to allow the vehicle to continue along the mission track. The decreasing variable speed was applied to the same mission that was conducted previously. The results of the simulated mission as well as the vehicle data are shown in Figure 32 and 33, respectively.

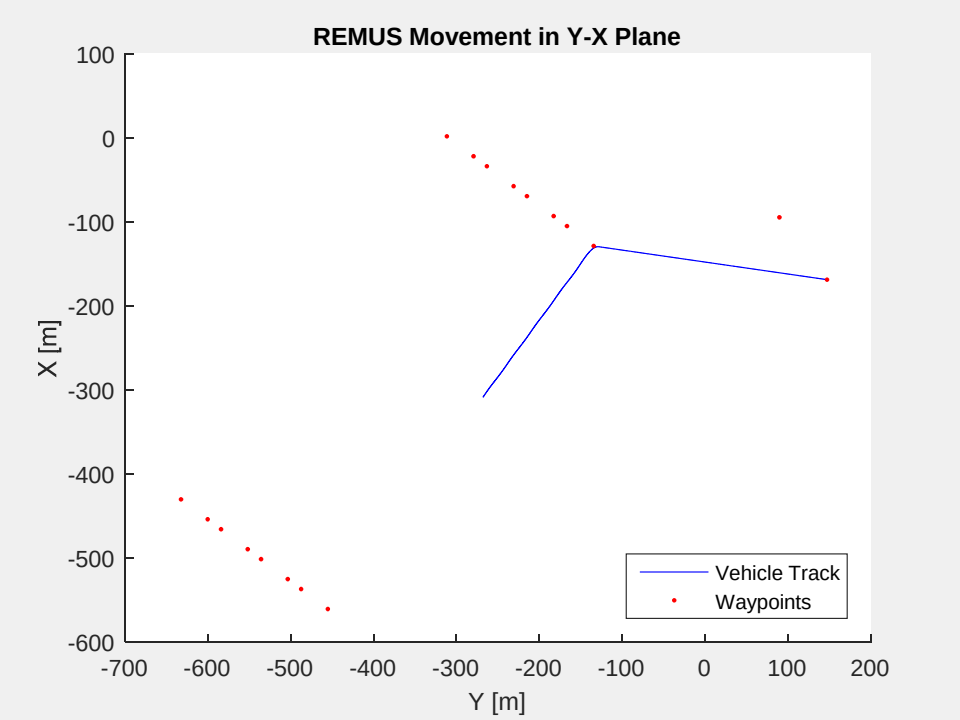

Figure 32. Simulated Mission Utilizing Decreasing Variable Speed

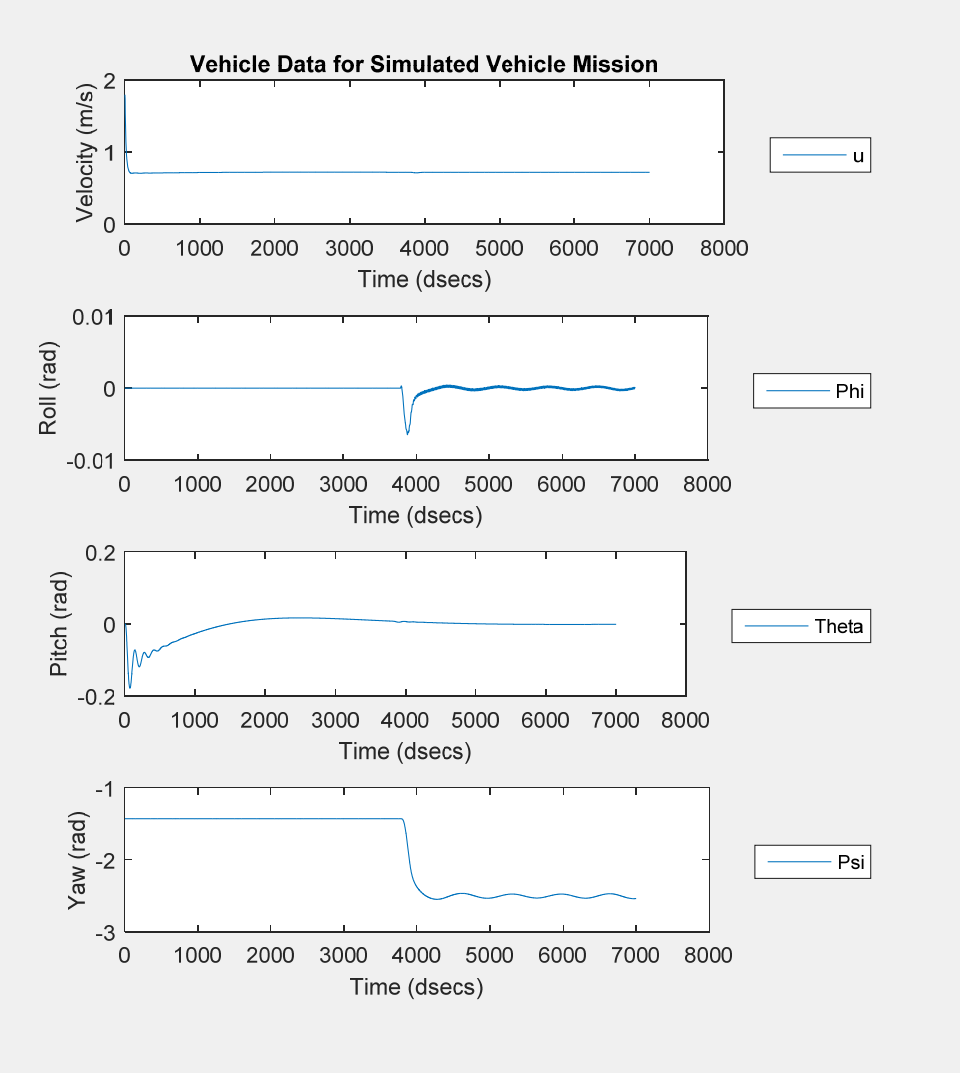

Figure 33. Vehicle Data for Simulated Mission Utilizing Decreasing Variable Speed

Similar to the increasing forward velocity mission, the decreasing forward velocity reached the desired velocity goals, however, unlike the increasing velocity mission, the overall vehicle performance was found acceptable. The results of this mission show that the stability issues associated with variable speeds are more significant with increasing forward velocity than decreasing forward velocity. Given that this decreasing velocity capability is what this thesis specifically looks to utilize to for simulated docking missions, the implementation and control of the tunnel thrusters was

conducted before any further investigation into the effect of forward velocity on the hydrodynamic coefficients.

As previously discussed in Chapter III, the tunnel thrusters were developed utilizing experimental tests and previous mission results. Once the correct force and torque equations as well as the PI controllers for RPM commands were implemented for the vertical and lateral tunnel thrusters, the controllers for reducing heading error, cross track error, pitch error, and depth error were developed. The general form that implemented for these controllers sought to relate the linear or angular displacement error to a force value which would then be split between the forward and aft tunnel thrusters and then converted into an equivalent RPM command. This RPM command would then be fed into the PI RPM controller as well as be converted back into a force and the subsequent torque. The hydrodynamic model and ODE45 solver then convert this force into either a linear or angular velocity which can then be propagated forward and a new error value can be obtained. This general form is visually represented in Figure 34.

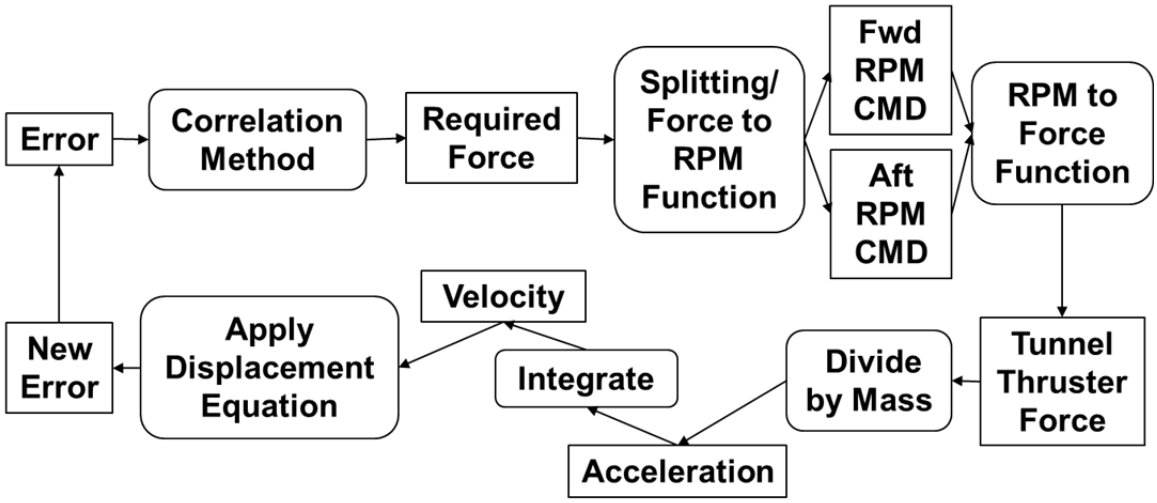

Figure 34. General Error Control Instituted for Tunnel Thrusters

The ultimate goal of the simulation model was to conduct a typical REMUS mission and then simulate docking to a docking station. With this goal in mind, a new mission was designed where the vehicle would conduct several surveying legs and then

attempt to dock. During the final docking leg the cross tunnel thrusters would then be engaged to stabilize the vehicle on its terminal trajectory as the forward velocity decreased. This mission was conducted with and without tunnel thrusters to gauge the effectiveness of the tunnel thruster control. For this mission a simple linear correlation between the depth error and lateral error to the track line were used. This run looked to develop adequate control of strictly linear displacement, and address errors in angular displacement later. The simulation results are shown in Figures 35, 36, 37, and 38, which display the total vehicle track, the docking component of the vehicle track, the Tunnel Thruster RPMs, and the linear velocities and angular displacements, respectively.

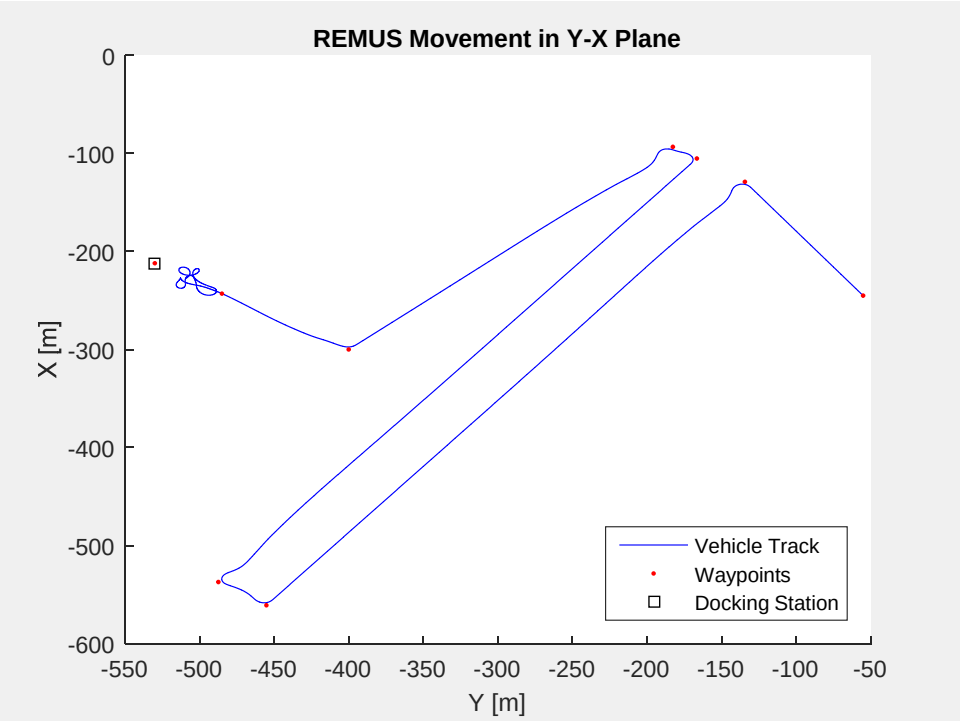

Figure 35. Simulated REMUS Mission with Docking Component

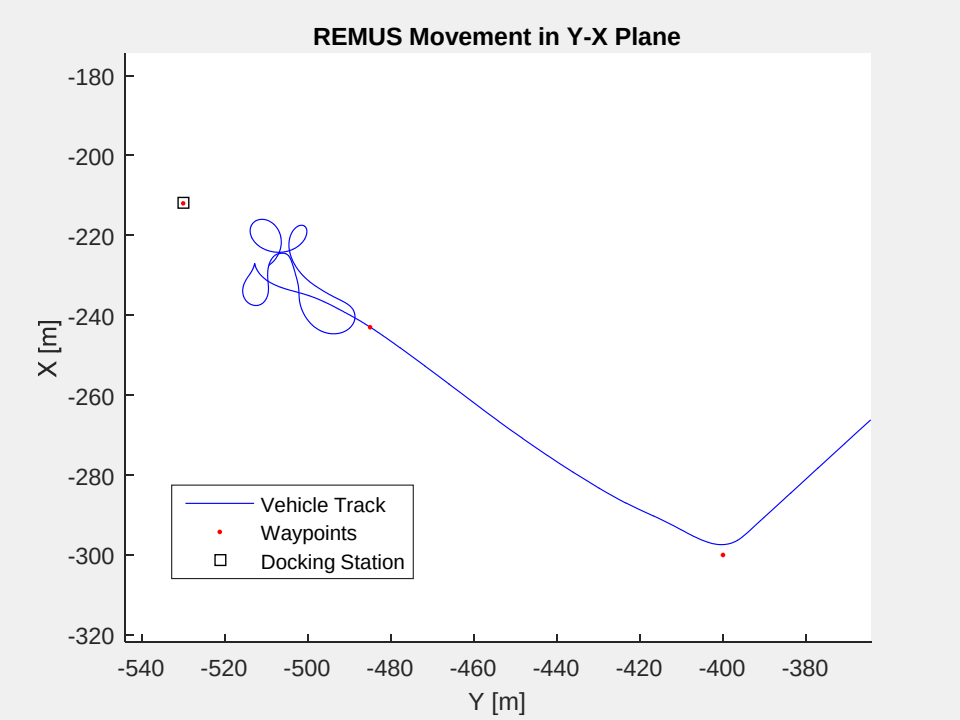

Figure 36. Simulated REMUS Mission with Docking Component (Zoomed)

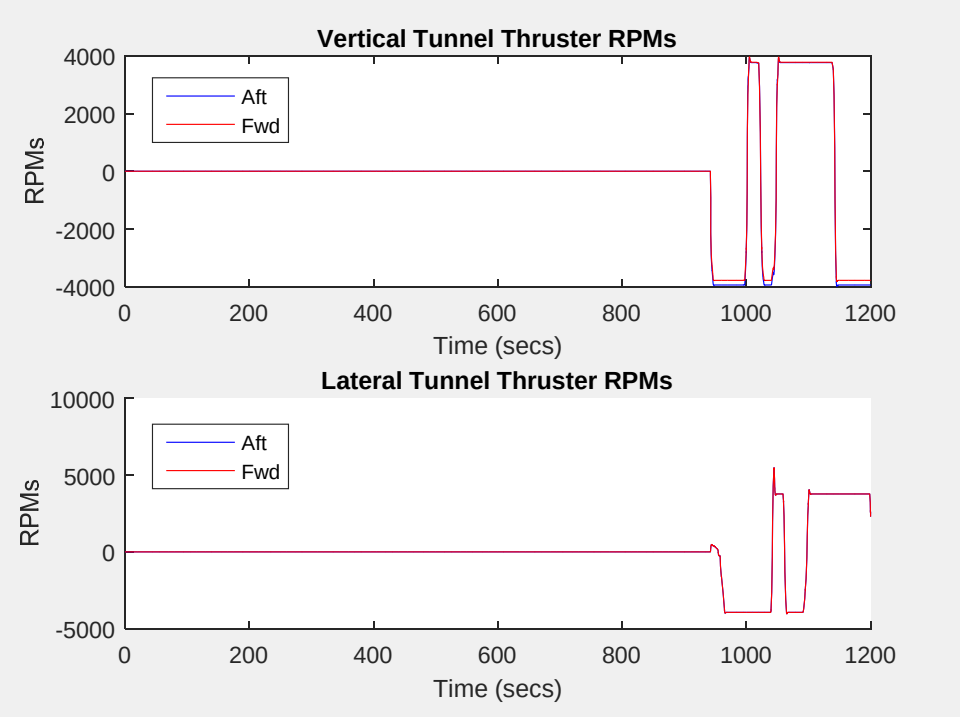

Figure 37. Tunnel Thruster RPMs for Simulated Mission with Docking Component

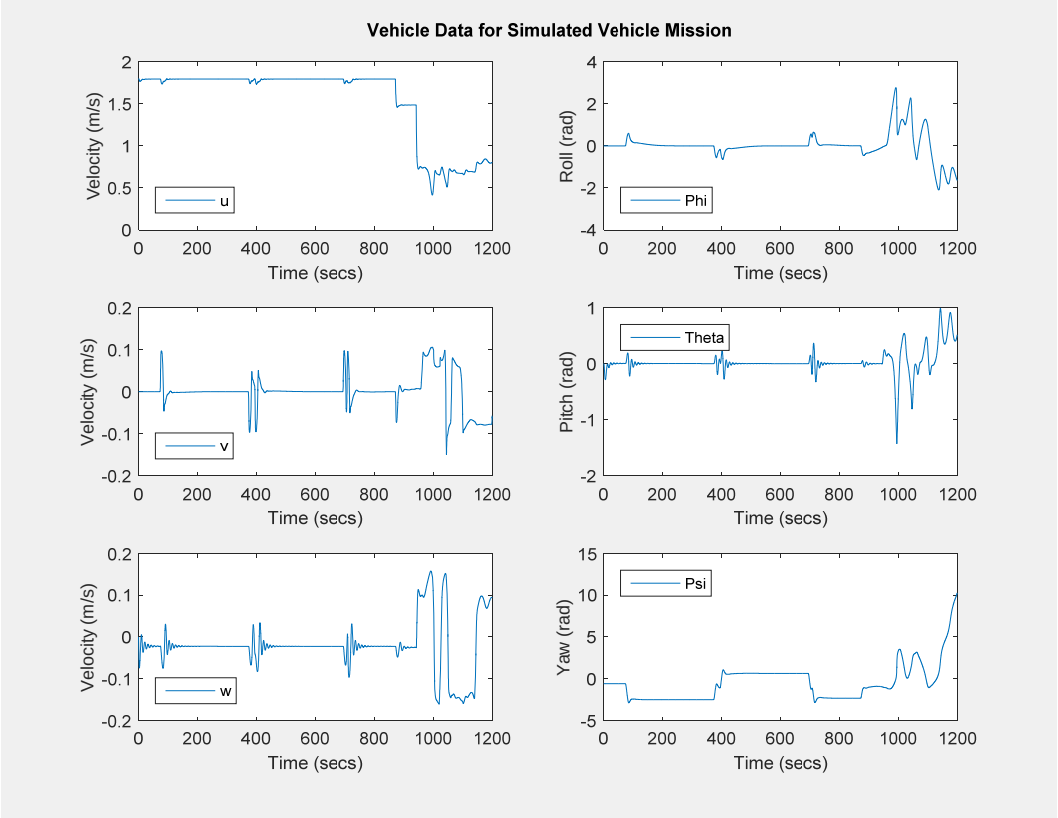

Figure 38. Linear Velocities and Angular Displacement for Simulated Mission with Docking Component

Reviewing Figures 35–38, it is clearly seen that that simulated vehicle can successfully transition from a typical mission type, in this case surveying, to a subsequent docking mission. The vehicle also successfully reduced its speed from 1500 RPMS to 700 RPMs without becoming unstable. However, the docking portion of the mission was ultimately unsuccessful due to poor controllability at reducing the displacement errors in both depth and lateral track line error. A further investigation into alternative control methods as well as the cross coupling effects caused by the addition of the cross tunnel thrusters is necessary in order to fully gain the ability to simulate docking missions in the hydrodynamic simulation model.

B. POSITION ESTIMATION FILTER RESULTS

As previously discussed in Chapter IV, the development and testing of the position estimation filtering design was conducted with both user generated and real

REMUS data. The testing of the design also consisted of several variations of generated data as well as several variations of how the real data was handled and filtered. Given that the initial user generated data compiled the asynchronous, erroneous, and sporadic sensor behaviors in consecutive steps, only the final test is shown in this thesis for brevity. This final test consisted of the INS and USBL sensor operating at differing frequencies, the INS "failing" to account for unknown current measurements, sporadic USBL measurements to return measurements of zero for the x and y positions. The INS position measurements were also zeroed out to represent a lack of position update from the GPS. It should be noted that the USBL filter operated at the same frequency as the INS filter, but did not always have a positional measurement. This design feature was a way of simulating asynchronous sensor data. The generated data is shown in Figure 39 and the results of this filtering run are shown in Figure 40 where the vehicle track begins in the bottom left of the figure and travels right to the subsequent waypoints marked by the red squares. Additionally, the error or uncertainty of the position estimates are displayed via the trace of the covariance matrices, shown in Figure 41.

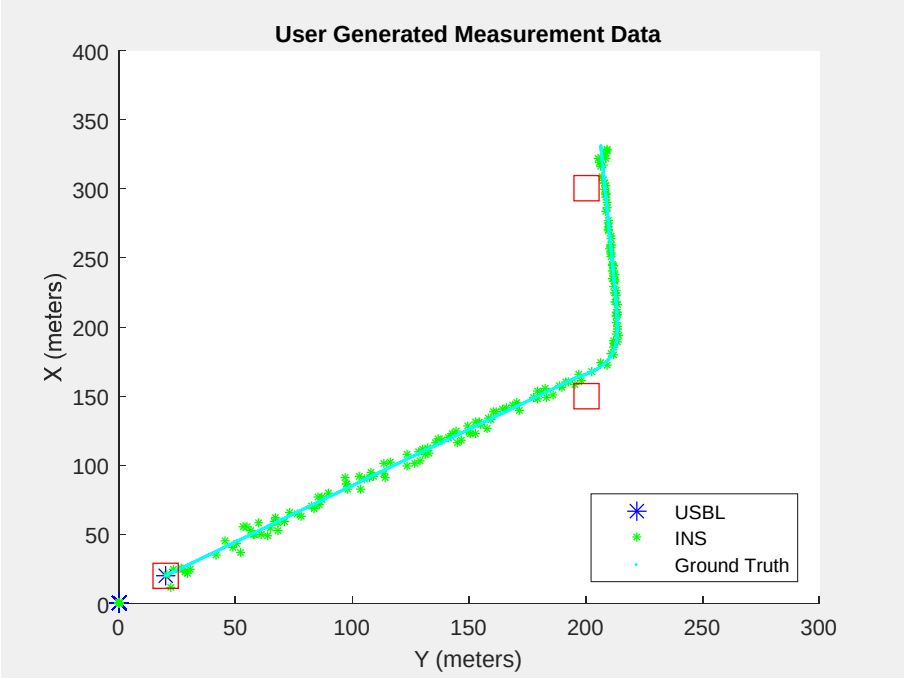

Figure 39. User Generated Measurement Data

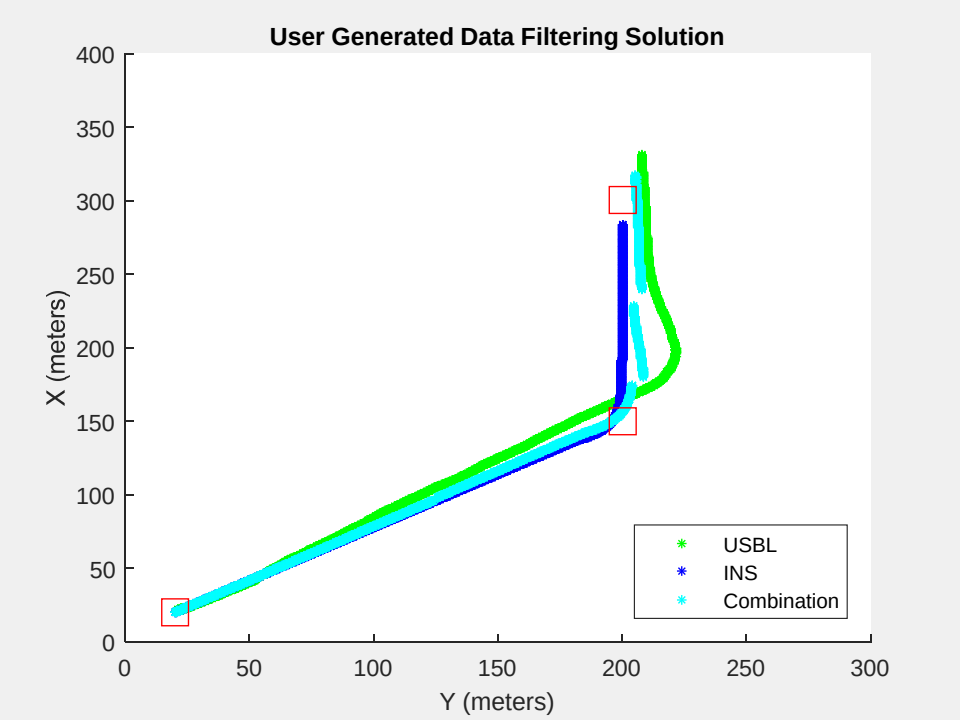

Figure 40. User Generated Data Final Filtering Run

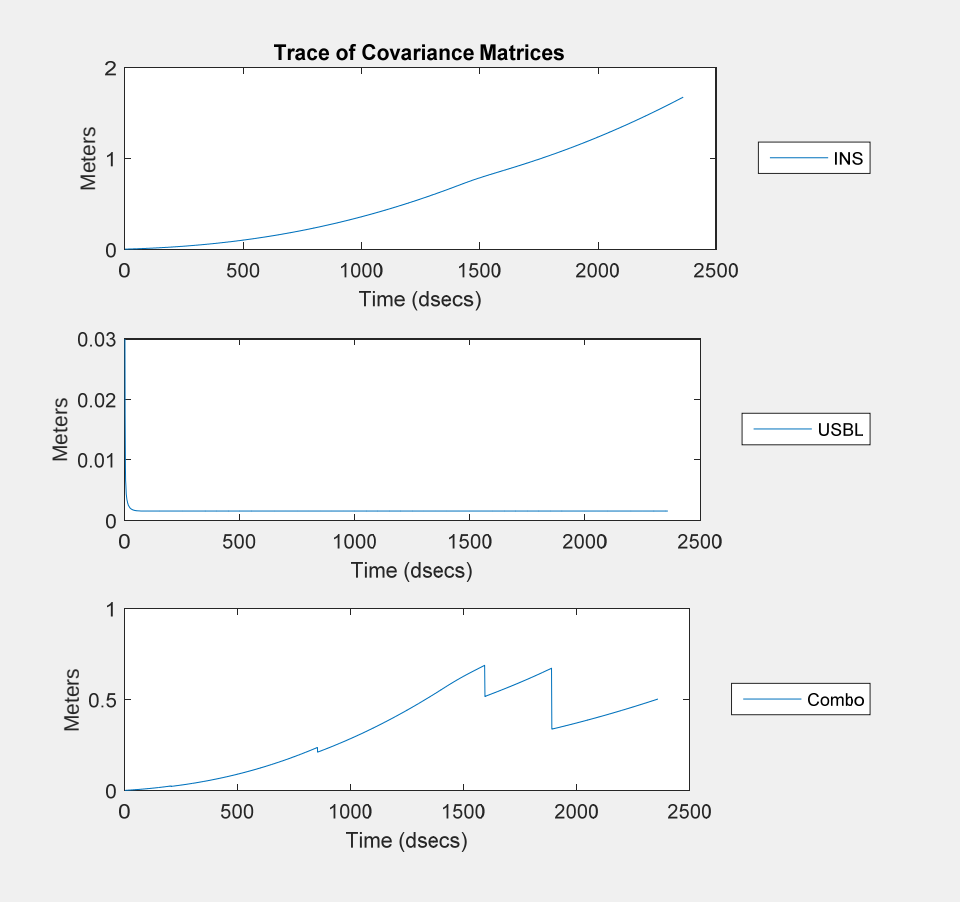

Figure 41. Positional Uncertainty Developed from Covariance Matrices

The weighting function applied in this run was developed as a function of range to the docking station, which is represented by the red square at the coordinates (200, 300). The results of this run does show adequate performance of the simple combination method in combining the two sensor systems with the goal of more accurately estimating the ground truth of the vehicle position. However, this combination method is fairly rudimentary and is sought to be used as a baseline combination method rather than the final method.

The positional uncertainty associated with the INS measurements does realistically represents the growing error. The INS error grows at a rate of .45% distance traveled, which for this mission, a traveled distance of approximately 370 meters, equates to approximately 1.6 meters of uncertainty which is seen in Figure 43. This capability of

realistically portraying the growing uncertainty of the INS system was experienced with the INS EKF function, but not with the INS UKF function which resulted in the use of an EKF with the INS rather than a UKF.

While the INS filter accurately represents the growing error within the system, the USBL error is not necessarily realistic to the actual sensor behavior. However, unlike the INS error, the USBL error is not necessarily a linear relation, but rather more likely a combination of range to the docking station and the specific environmental conditions. As a result of this non-linear assumption further investigation into the modeling of this error is necessary.

As a way to further verify the capability of this filtering system design, real REMUS mission data was used for the measurement updates. In order to obtain these measurements, previous mission files containing either docking attempts or terminal homing on an acoustic transponder were chosen. The data associated with the current vehicle state information, the INS, the USBL, and the ADCP/DVL were downloaded and then process by a MATLAB script to generate the appropriate measurement state vectors. It should be noted that the initial mission data maintained vehicle position as latitude, longitude, and depth. In order to maintain the same equations used in the filters for the user generated data, aforementioned MATLAB script also converted the latitude, longitude, and depth positions into a local tangent plane. The origin of this local tangent plane was located at the initial position of the vehicle at the start of the mission.

As previously discussed in Chapter IV, several methods of implementing the filter design with the real mission data were tested with limited initial success. The first method tested operating both the filters at the same frequency and tested whether an updated measurement had occurred, and if no measurement had occurred, the position portion of the measurement transition matrix associated with that specific filter was zeroed out in order to only propagate the positon forward and grow the positional uncertainty. This method experienced rapid divergence of the USBL filter given the significant time in between positional measurements. The Q and R matrices, which are traditionally used as tuning parameters to adjust the performance of Kalman filters, were altered in an attempt reduce or eliminate this divergence, but all attempts were

unsuccessful. This method was also tested with ADCP velocity measurements and zeroed out INS position measurements and again resulted in the divergence of the USBL filter as well as a divergence of the INS filter when the position measurements were not updated.

The second method tested operated the INS filter at a constant frequency while the USBL filter only ran once a measurement was available. This method was developed as a way to prevent divergence with the USBL filter. In order to maintain an accurate representation of the linear velocities, heading, and heading rate in between USBL measurements, the a priori USBL measurements were averaged with the posterior INS estimate after every successive run of the INS filter. During the development of this method it was decided that a potentially more accurate method of a combined position estimate would be to continually propagate forward the most recent combined estimate. This method was accomplished by adding an additional EKF for the position estimate, for the actual vehicle testing this would be considered the state measurement. Additionally, another measurement comparison was considered, which consisted of comparing the USBL measurement with the most recent propagated position estimate instead of the INS measurement. Both the comparisons were tested to determine which yielded more acceptable filter solutions.

The filter was operated two ways, the first was at the same frequency of the INS filter and the second was similar to the USBL filter with respect to its operating frequency and averaging its a priori estimate with the posterior INS estimate. The posterior estimate of this new EKF was then combined with the posterior USBL estimate in a similar manner as before, solely a function of range. Similar to the testing conducted with the first method, the ADCP velocities were substituted in for the INS velocities and the measurement transition matrix of the INS filter were zeroed out. However, the use of ADCP velocities resulted in worse performance than the INS velocities and the zeroed out INS measurement positions again resulted filter diverges. The ADCP and INS results are left out of this thesis for brevity.

The filtered solution weighting INS data versus USBL data is shown in Figure 42, and the subsequent traces of the covariance matrices are shown in Figure 43. The results of this filtered solution display unrealistic state estimates that do not necessarily

propagate forward. This forward propagation of the vehicle estimate is the desired behavior in order to realistically represent the forward motion of the REMUS vehicle.

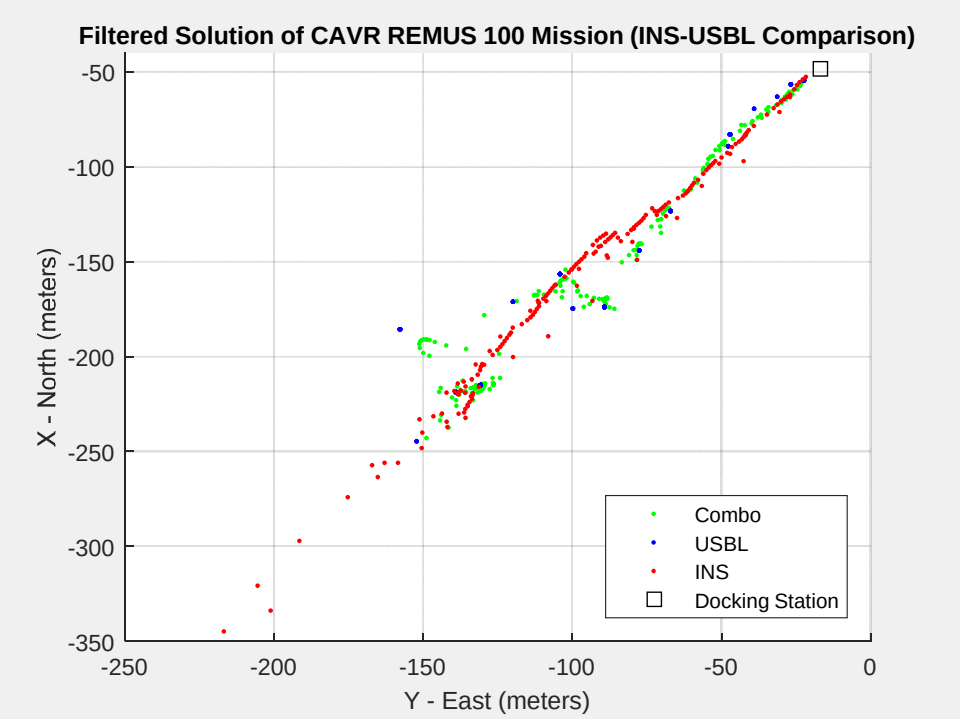

Figure 42. Filtered Solution Weighting INS and USBL Measurements

The covariance values shown in Figure 43 accurately depict the growing error within the tested filtering system, but do not necessarily reflect the realistic behavior of the sensor errors. Due to the divergence of the INS EKF when the position measurements were zeroed out, the error was only able to grow during filter iterations where there was no new INS measurements. The spikes seen with the INS covariance however are not a result of the growing error but rather significant jumps in the INS data, most likely a result of the REMUS vehicle updating or correcting for errors in the INS. These jumps or corrections are an example of one reason working with this post processed data limits the full extent of the filter development. The data extracted from the REMUS vehicle is not necessarily the true sensor information and is probably filtered before it is delivered as a measurement. Given the proprietary nature of this filtering, it is not available to the end user, and the best available sensor measurements were the post-processed ones.

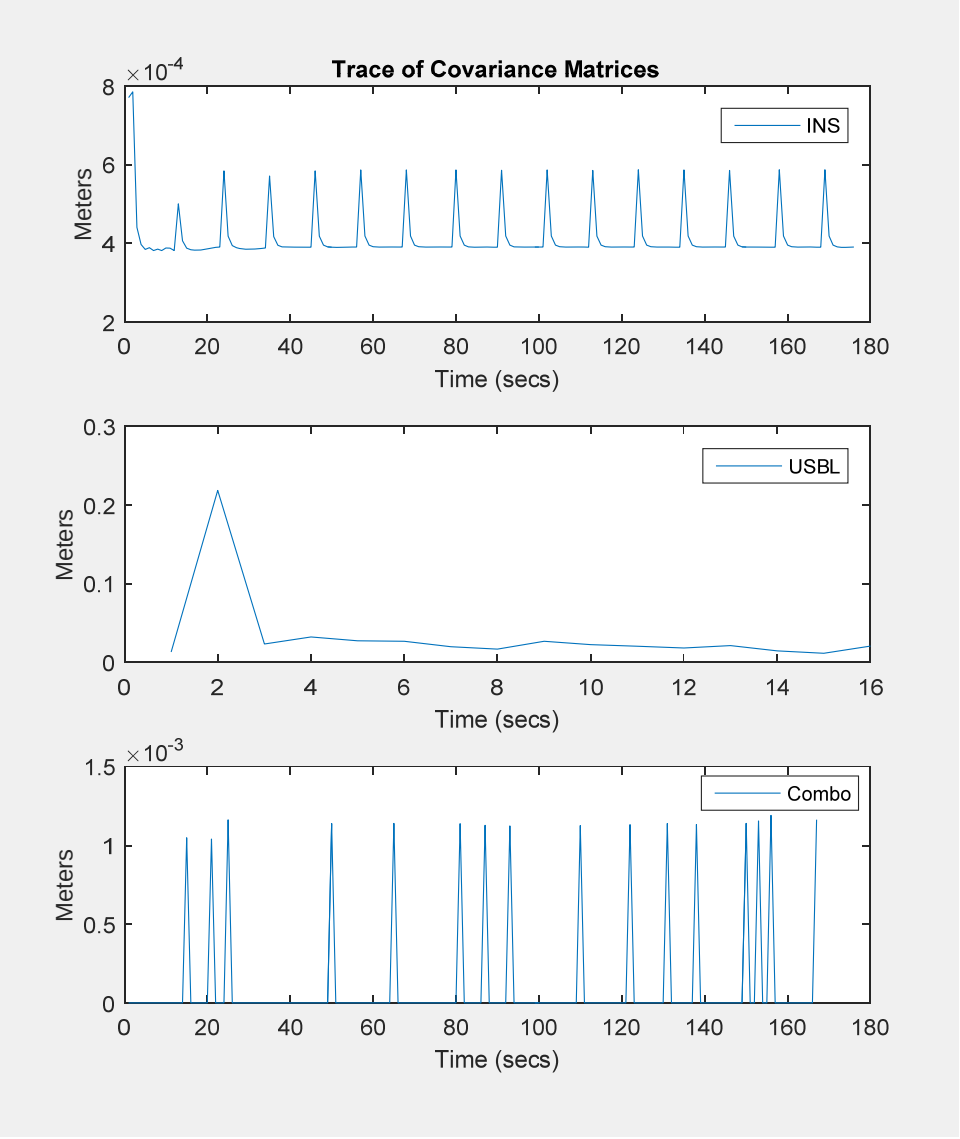

Figure 43. Trace of Covariance Matrices for Filtered INS-USBL Comparison

In order to achieve more realistic position estimation results the comparison between USBL and INS was changed to the USBL sensor and the a priori position estimate propagated forward one time step. The results of this new filtering process are shown in Figure 44 and the traces of the filter covariance matrices are shown in Figure 45.

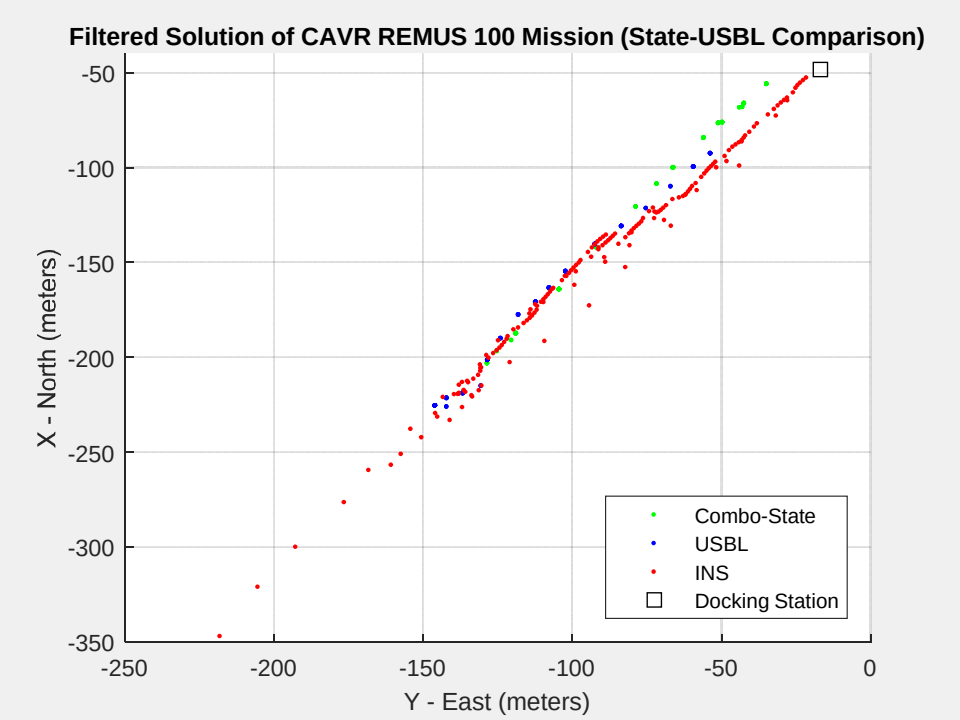

Figure 44. Filtering Solution Comparing USBL and Propagated Position Estimate

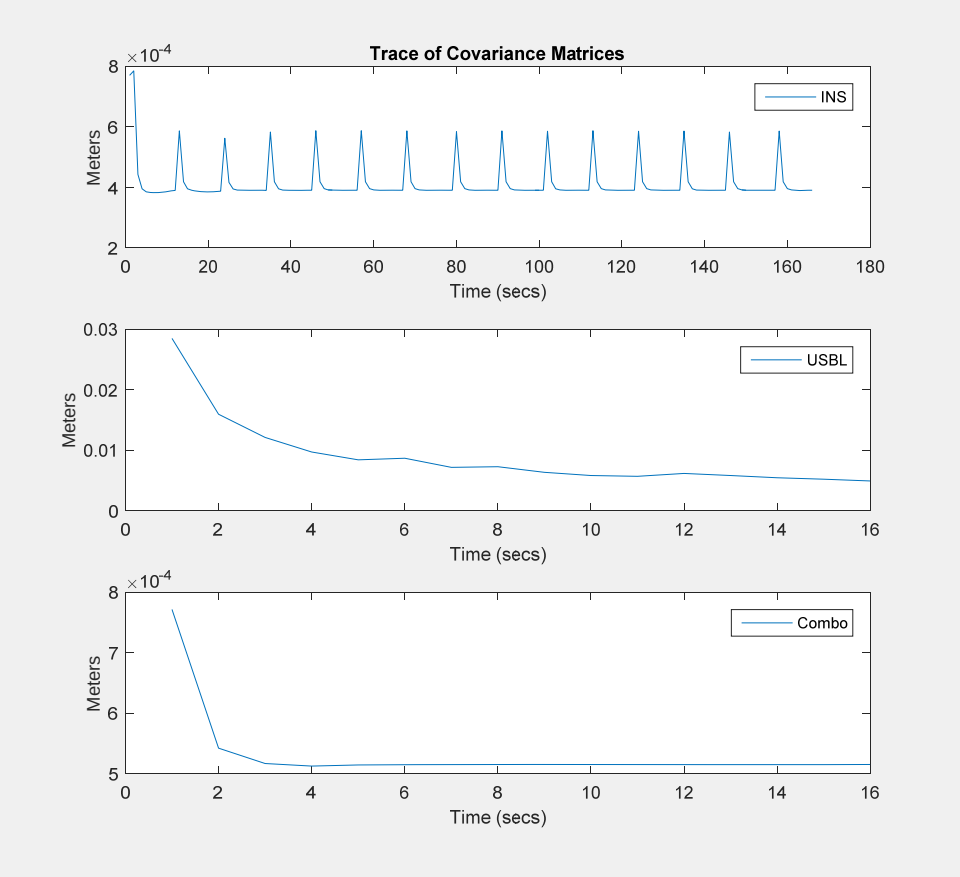

Figure 45. Trace of Covariance for USBL and Propagated Estimate Comparison

The position estimates shown in Figure 45, while less in quantity, do provide a more realistic representation of a position estimate that accurately accounts for the motion of the vehicle as well as the USBL measurements. While the method used to determine USBL measurement accuracy is not necessarily representative of the entire USBL error, it does provide a baseline performance that can be compared to the vehicle state measurements as an initial way to determine the adequacy of the filter results. These state measurements, as described earlier in this thesis, are the outputs of the primary built-in REMUS filter that develops a position estimate by incorporating all available sensor systems. While this comparison is not being used as a metric to determine whether the filter is more successful than the primary vehicle filter, it is used as a means of determining if the filtered solution is reasonable. The only hard metric that can be used to compare filtering processes is successful vehicle docking, which requires real time

vehicle testing. The results from of the filtered solution, INS solution, and vehicle State position are shown in Figure 46.

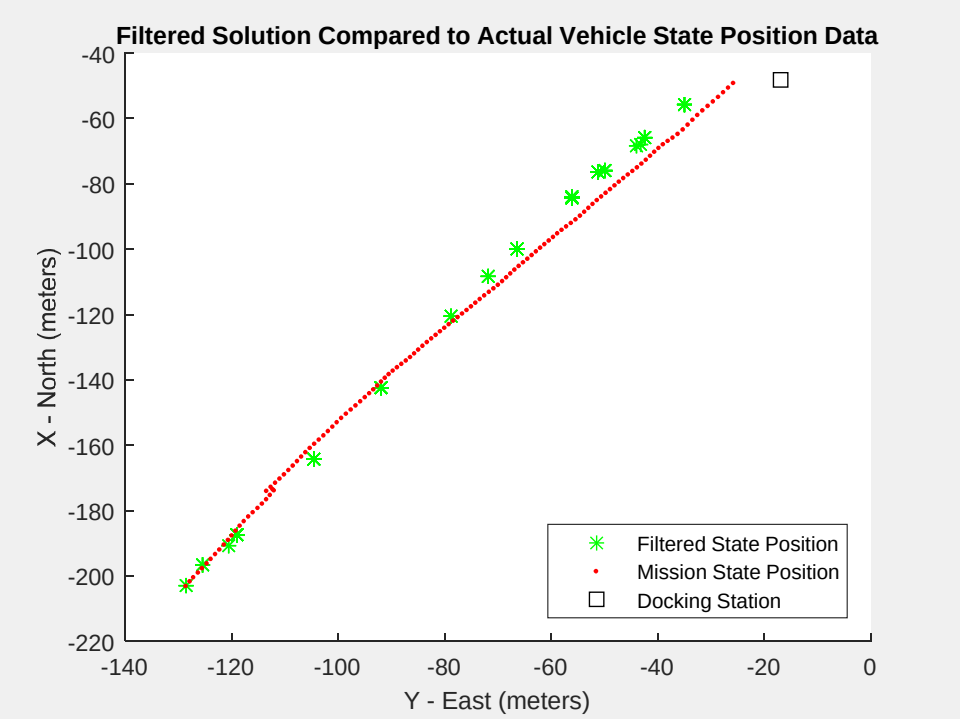

Figure 46. Final Filtered Solution Compared to Vehicle State Position

With respect to the trace of the covariance matrices shown in Figure 46, the results are similar to those shown in Figure 45, the errors accurately represent the design of the filters and experience similar error spikes as a result of discontinuities or jumps in the data. Further investigation into accurately modeling INS and USBL error is necessary to develop a full understanding of how best to weigh sensor system measurements.

VI. CONCLUSION

In this thesis several aspects surrounding the difficulties with terminal homing for autonomous underwater vehicles were explored. The first part of this thesis looked to develop a simulation model rooted in the hydrodynamic properties of the CAVR REMUS 100 vehicle. This model was more specifically developed to generate the capability of simulating docking missions with the new REMUS 100 configuration, which consists of four cross tunnel thrusters. In addition to the hydrodynamic model, this thesis also looked to present a potential filtering system that would ultimately provide a method of more accurately estimating the position of the REMUS vehicle through the utilization of the available sensor systems. The design presented in this thesis was specifically tailored to the INS and USBL sensor system.

A. HYDRODYNAMIC MODEL

The first contribution of this thesis was the hydrodynamic simulation model for the new CAVR REMUS 100 vehicle. This model incorporated the new cross tunnel thrusters in a manner that accurately portrayed realistic force and torque generation through experimental testing. Similar to the tunnel thruster force experiments, the aft thruster force generation was developed from experimental testing. In addition to the experimental testing, several other aspects of the model were compared to real REMUS mission data to ensure realistic performance. These aspects that were compared to mission data consisted of the tunnel thruster RPM control, aft thruster RPM control, rudder and dive fin actuator control, depth controller performance, and developed velocities from the aft thruster and tunnel thrusters. This model also took initial steps into investigating the effect of forward velocity on the hydrodynamic coefficients. One specific step taken was developing a set of functions that generate the appropriate hydrodynamic damping coefficients for the X-force component that generate realistic forward velocities given specific RPM commands. Another step taken was determining that the varying the forward velocity from a larger value to a smaller value affects the performance of the hydrodynamic simulation significantly less than operating with an

increasing velocity. The last contribution of the hydrodynamic model was an initial control algorithm that adequately controls the tunnel thrusters to reduce the heading error, cross track error, depth error, and pitch error.

B. POSITION ESTIMATION FILTER

The second contribution of this thesis is a preliminary positional estimation filter design capable of handling asynchronous, sporadic, and erroneous sensor measurements from the available REMUS sensor systems. This filter design was specifically implemented with the INS and USBL system but remains flexible for additional sensor systems, such as an optic sensor system capable of high positional accuracy within close proximity to the docking station. This flexibility also extends to the weighting or combination method of the various sensor systems. Several weighting methods were tested and shown to be adequate in this thesis, and were also easily swapped out.

As a result of not being able to implement the filtering system on board the actual REMUS vehicle, the largest difficulty faced during the development of this filtering process was having to base the development of the filter off post processed data. The REMUS software processes all the sensor information before it is recorded as a measurement, and as previously discussed these processing methods are not available to the user. As a result of these proprietary processes, any secondary filtering processes that is different than the primary, built in filter on the vehicle must be tested using "non-true" sensor measurements. Several filtering methods that were believed to be a potentially viable were unable to be tested given the data the REMUS vehicle provides to the end user. Conducting filtering tests onboard the actual vehicle are believed to provide more viable, adequate filtering results than what is capable with post processed data. Additionally, testing post processed data can only be used to a limited extent because there is no metric to determine the success of the filtering process. The only metric that can truly determine if one filtering process is better than another, and that is the extent of successful vehicle docking.

C. FUTURE WORK

1. Hydrodynamic Model

Several further areas should be explored with regards to the hydrodynamic model. The first, and largest, area is to further investigate the effect of forward velocity on the hydrodynamic coefficients, and specifically look to generate correlations or functions that relate the coefficient values to forward velocity or RPM commands. The second area is to explore other control methods of handling the tunnel thruster force generation during the docking portion of simulated missions in order to reduce the linear and angular displacement errors. The final area is to conduct a computational fluid dynamic simulation of the REMUS 100 in a variety of conditions to more thoroughly understand the flow about the vehicle in hopes to develop more accurate hydrodynamic coefficient terms, and then compare these results to the current model performance and coefficients.

2. Position Estimation Filter

The actual implementation of the designed filtering system was unable to be tested on board the CAVR REMUS 100 in a real time environment. The primary focus of follow on work should focus on converting the MATLAB based filtering system into the REMUS architecture. Additionally, further investigation into weighting functions that account for the complete system error should be conducted, specifically looking to use the filter covariance matrices as the primary method of weighting the sensor estimates.

THIS PAGE INTENTIONALLY LEFT BLANK

APPENDIX A. VEHICLE PARAMETERS

Vehicle Parameter	Value	Units	Description
ρ	1030	kg/m^3	Seawater Density
L	2.26	m	Length
D	0.19	m	Diameter
m	52.5	kg	Mass
W	515.03	N	Weight
B	518.36	N	Buoyancy
A_f	0.0285	m^2	Hull Frontal Area
x_G	0	m	Center of Gravity wrt Origin at COB
y_G	0	m	Center of Gravity wrt Origin at COB
z_G	0.0196	m	Center of Gravity wrt Origin at COB
I_{xx}	0.769	$kg\text{-}m^2$	X-Moment of Inertia wrt Origin at COB
I_{yy}	19.13	$kg\text{-}m^2$	Y-Moment of Inertia wrt Origin at COB
I_{zz}	19.13	$kg\text{-}m^2$	Z-Moment of Inertia wrt Origin at COB

THIS PAGE INTENTIONALLY LEFT BLANK

APPENDIX B. HYDRODYNAMIC COEFFICIENTS

Coefficient	Value	Units	Description
X_{uu}	-9.54	kg/m	Axial Drag in Surge
$X_{\dot{u}}$	-0.93	kg	Added Mass in Surge
X_{wq}	-77.8	kg/rad	Added Mass in Surge Cross-Term
X_{qq}	-1.93	kg-m/rad	Added Mass in Surge Cross-Term
X_{vr}	35.5	kg/rad	Added Mass in Surge Cross-Term
X_{rr}	-1.93	kg-m/rad	Added Mass in Surge Cross-Term
Y_{vv}	-2850	kg/m	Cross-Flow Drag in Sway
Y_{rr}	0.632	kg-m/rad	Cross-Flow Drag in Sway
Y_{uv}	-28.6	kg/m	Body Lift Force and Fin Lift
$Y_{\dot{v}}$	-77.8	kg-m/rad^2	Added Mass in Sway
$Y_{\dot{r}}$	4.16	kg	Added Mass in Sway
Y_{ur}	0.884	kg/rad	Added Mass in Sway Cross-Term
Y_{wp}	77.8	kg/rad	Added Mass in Sway Cross-Term
Y_{pq}	4.16	kg-m/rad	Added Mass in Sway Cross-Term
$Y_{uu\delta r}$	9.64	kg-m/rad	Fin Lift Force
Z_{ww}	-28.6	kg/m	Cross-Flow Drag in Sway
Z_{qq}	-0.632	kg/m	Cross-Flow Drag in Sway
$Z_{\dot{w}}$	-77.8	kg-m/rad^2	Added Mass in Heave
$Z_{\dot{q}}$	-4.16	kg-m/rad	Added Mass in Heave
Z_{uw}	-28.6	kg/rad	Body Lift Force and Fin Lift
Z_{uq}	-12.22	kg/rad	Added Mass in Heave Cross-Term and Fin Lift
Z_{vp}	-77.8	kg/rad	Added Mass in Heave Cross-Term
Z_{rp}	1.5	kg/rad	Added Mass in Heave Cross-Term
$Z_{uu\delta s}$	-9.64	kg/m-rad	Fin Lift Force
K_{pp}	-0.13	kg-m^2/ rad^2	Rolling Resistance
$K_{\dot{p}}$	-0.14	kg-m^2 /rad^2	Added Mass
M_{ww}	3.18	kg	Cross-Flow Drag in Heave
M_{qq}	-188	kg-m^2 /rad^2	Cross-Flow Drag in Heave
M_{uw}	24	kg	Body Lift Force and Fin Lift

Coefficient	Value	Units	Description
$M_{\dot{w}}$	-4.16	kg-m	Added Mass in Pitch
$M_{\dot{q}}$	-30	kg-m^2/rad	Added Mass in Pitch
M_{uq}	-10	kg-m/rad	Added Mass in Pitch Cross-Term and Fin Lift
M_{vp}	-1	kg-m/rad	Added Mass in Pitch Cross-Term
M_{rp}	4.86	kg-m^2 /rad^2	Added Mass in Pitch Cross-Term
$M_{uu\delta s}$	-6.15	kg/rad	Fin Lift Moment
N_{vv}	-3.18	kg	Cross-Flow Drag in Yaw
N_{rr}	-100	kg-m^2 /rad^2	Cross-Flow Drag in Yaw
N_{uv}	-24	kg	Body and Fin Lift Moment
$N_{\dot{v}}$	4.16	kg-m	Added Mass in Yaw
$N_{\dot{r}}$	-4.88	kg-m^2/rad	Added Mass in Yaw
N_{ur}	-2	kg-m/rad	Added Mass in Yaw Cross-Term and Fin Lift
N_{wp}	-1.93	kg-m/rad	Added Mass in Yaw Cross-Term
N_{pq}	-4.86	kg-m^2 /rad^2	Added Mass in Yaw Cross-Term
$N_{uu\delta r}$	-6.15	kg/rad	Fin Lift Moment

LIST OF REFERENCES

[1] G. Evans. (2010, Oct 15). UUVs: Unmanned and in demand [Online] Available: http://www.naval-technology.com/features/feature98410/

[2] National Research Council (U.S.). "Committee for mine warfare assessment, naval mine warfare: operational and technical challenges for naval forces." Washington, DC: National Academy Press, 2001.

[3] Technology and the Mine Problem Symposium, and Naval Postgraduate School (U.S.), *Proceedings of the Seventh International Symposium, Technology and the Mine Problem*: Monterey, CA: Naval Postgraduate School, 2006.

[4] L. Gerken, *ASW Versus Submarine Technology Battle.* Chula Vista, CA: American Scientific, 1986.

[5] *REMUS Operations and Maintenance Manual*. Kongsberg, Norway: Kongberg Maritime, 2007.

[6] T. Fossen, *Guidance and Control of Ocean Vehicles*. New York: John Wiley and Sons, 1994.

[7] T. Prestero, "Verification of a six-degree of freedom simulation model for the REMUS autonomous underwater vehicle," M.S. thesis, Applied Ocean Science and Engineering, Massachusetts Institute of Technology, Boston, MA, 2001.

[8] D. E. Sgarioto, "Control system design and development for REMUS autonomous Underwater Vehicle," Defense Technology Age., Auckland, NZ, May 2007.

[9] M. Doherty, "Cross body thruster control and modeling of a body of revolution autonomous underwater vehicle," M.S. thesis, Mechanical Eng. Dept., Naval Postgraduate School, Monterey, CA, 2005.

[10] M. Blanke, K.-P. Lindegaard, and T. I. Fossen, *Dynamic Model for Thrust Generation of Marine Propellers*, Proceedings Volume from the 5th IFAC Conference. pp. 363–368. 2001.

[11] B. Allen, T. Austim, N. Forrester, R. Goldsborough, A. Kukulya, G. Packard, M. Purrell, and R. Stokey, *Autonomous Docking Demonstrations with Enhanced REMUS Technology*, OCEANS, pp. 1–6, Sep. 2006.

[12] R. S. McEwen, B. W. Hobson, L. McBride, and J. G. Bellingham, Docking Control System for a 54-cm-Diameter (21-in) AUV, *IEEE Journal of Oceanic Engineering*, Vol. 33, no. 4, pp. 550–562, Oct. 2008.

[13] C. Yang, S. Peng, S. Fan, S. Zhang, P. Wang, and Y. Chen, "Study on docking guidance algorithm for hybrid underwater glider in currents," Zhejiang University, Hangzhou, China. 2015.

[14] L. Armesto, S. Chroust, M. Vincze, and J. Tornero, *Multi-rate Fusion with Vision and Inertial Sensors,* Robotics and Automation, 2004. Proceedings. ICRA '04. 2004 IEEE International Conference on, Vol.1, pp. 193–199, 2004.

[15] Y. Geng and J. Sousa, "Hybrid derivative-free EKF for USBL/INS tightly-coupled integration in AUV," Autonomous and Intelligent Systems (AIS), 2010 International Conference on, Povoa de Varzim, pp. 1–6, 2010.

[16] N. Syahroni, "OCP based decentralized data fusion for autonomous underwater vehicles," Information Technology and Electrical Engineering (ICITEE), 2013 International Conference on, Yogyakarta, pp. 465–469, 2013.

[17] J. Ali and F. Jiancheng, "Multisensor data synthesis using federated of unscented Kalman filtering," 2005 IEEE International Conference on Industrial Technology, Hong Kong, pp. 524–529, 2005.

[18] C. H. Dillard, "Energy-efficient underwater surveillance by means of hybrid aquacopters," M.S. thesis, Mechanical Eng. Dept., Naval Postgraduate School, Monterey, Ca, 2014.

[19] E. A. Wan and R. Van Der Merwe, *The Unscented Kalman Filter for Nonlinear Estimation,* Adaptive Systems for Signal Processing, Communications, and Control Symposium 2000. AS-SPCC. The IEEE 2000, Lake Louise, Alta., pp. 153–158, 2000.

[20] S. Sarkka, *On Unscented Kalman Filtering for State Estimation of Continuous-Time Nonlinear Systems,* IEEE Transactions on Automatic Control, vol. 52, no. 9, pp. 1631–1641, Sept. 2007.

[21] B. Allotta et al., *A Comparison Between EKF-based and UKF-based Navigation Algorithms for AUVs Localization,* OCEANS 2015 - Genova, Genoa, pp. 1–5, 2015.

[22] *Kearfott's Proven Sea Navigation Unit.* Little Falls, NJ: Kearfott Corporation, 2010.

[23] The Society of Naval Architects and Marine Engineers. *Nomenclature for Treating the Motion of a Submerged Body Through a Fluid,* Technical Bulletin No. 1–5, 1950.

[24] T. I. Fossen and M. Blanke, Nonlinear Output Feedback Control of Underwater Vehicle Propellers Using Feedback from Estimated Axial Flow Velocity*, IEEE Journal of Oceanic Engineering,* Vol. 25, No. 2, pp. 241–255, 2000.

[25] A. J. Healey, Rock, S. M. Rock, S. Cody, D. Miles, and J. P. Brown, Toward an Improved Understanding of Thruster Dynamics for Underwater Vehicles, *IEEE Journal of Oceanic Engineering,* Vol. 20, No. 4, pp. 354–361, 1995

[26] B. Allen, S.W. Vorus, and T. Prestero, *Propulsion System Performance Enhancements on REMUS AUVs,* Proceedings of the MTS/IEEE OCEANS 2000 Conference, 11-Providence, RI, pp. 1869–1873, 14 Sep. 2000,

[27] D. B. Marco and A. J. Healey, *Command, Control and Navigation Experimental Results With the NPS ARIES AUV,* IEEE Journal of Oceanic Engineering, Vol. 26,No. 4, pp. 466–477, 2001.

[28] D. Simon, *Optimal State Estimation: Kalman, H-Infinity and Nonlinear Approaches*. Hoboken, NJ: John Wiley & Sons, 2006.

[29] J. Julier and J. K. Uhlmann, "Unscented filtering and nonlinear estimation," in *Proceedings. of the IEEE, 2004*, vol. 92, no. 3, pp. 401–422.

THIS PAGE INTENTIONALLY LEFT BLANK

INITIAL DISTRIBUTION LIST

1. Defense Technical Information Center
   Ft. Belvoir, Virginia

2. Dudley Knox Library
   Naval Postgraduate School
   Monterey, California